

ROBUST PHASE SENSITIVE INVERSION RECOVERY IMAGING

A Thesis

by

RAVINDRA MAHENDRAKUMAR GARACH

Submitted to the Office of Graduate Studies of
Texas A&M University
in partial fulfillment of the requirements for the degree of

MASTER OF SCIENCE

August 2005

Major Subject: Electrical Engineering

ROBUST PHASE SENSITIVE INVERSION RECOVERY IMAGING

A Thesis

by

RAVINDRA MAHENDRAKUMAR GARACH

Submitted to the Office of Graduate Studies of
Texas A&M University
in partial fulfillment of the requirements for the degree of
MASTER OF SCIENCE

Approved by:

Chair of Committee,	Jim Ji
Committee Members,	Aniruddha Datta
	Deepa Kundur
	Lihong Wang
Head of Department,	Chanan Singh

August 2005

Major Subject: Electrical Engineering

ABSTRACT

Robust Phase Sensitive Inversion Recovery Imaging. (August 2005)

Garach, Ravindra Mahendrakumar, B.E., Gujarat University

Chair of Advisory Committee: Dr. Jim Ji

Inversion Recovery (IR) is a powerful tool for contrast manipulation in Magnetic Resonance Imaging (MRI). IR can provide strong contrast between tissues with different values of T1 relaxation times. The tissue magnetization stored at an IR image pixel can take positive as well as negative values. The corresponding polarity information is contained in the phase of the complex image. Due to numerous factors associated with the Magnetic Resonance (MR) scanner and the associated acquisition system, the acquired complex image is modulated by a spatially varying background phase which makes the retrieval of polarity information non-trivial. Many commercial MR scanners perform magnitude-only reconstruction which, due to loss of polarity information, reduces the dynamic contrast range. Phase sensitive IR (PSIR) can provide enhanced image contrast by estimating and removing the background phase and retrieving the correct polarity information. In this thesis, the background phase of complex MR image is modeled using a statistical model based on Markov Random Fields (MRF). Two model optimization methods have been developed. The first method is a computationally efficient algorithm for finding semi-optimal solutions satisfying the proposed model. Using an adaptive model neighborhood, it can reconstruct low SNR images with slow phase variations. The second method presents a region growing approach which can handle images with rapid phase variations. Experimental results using computer simulations and *in vivo* experiments show that the proposed method is robust and can perform successful reconstruction even in adverse cases of low signal to noise ratios (SNRs) and high phase variations.

To my loving family

ACKNOWLEDGMENTS

I would like to express my sincere appreciation to my advisor, Dr. Jim Ji, for guiding me throughout my graduate research.

I would like to thank Dr. Jingfei Ma for providing the MRI data used in this research, my committee members Dr. Lihong Wang, Dr. Aniruddha Datta and Dr. Deepa Kundur for their support and helpful discussions and to all my lab-mates: Swati, Dante, Kina and A for their contribution of ideas to my research.

I am thankful to my library supervisor, Ms. Lisa Craig-Young, for sanctioning my two week leave from my student worker job so that I could work on the final stages of my thesis.

Finally, I would like to thank my parents without whose emotional and financial support I could not have completed this work.

TABLE OF CONTENTS

CHAPTER		Page
I	INTRODUCTION	1
	A. Magnetic Resonance Imaging	1
	B. Inversion Recovery	2
	C. Phase-Sensitive Inversion Recovery (PSIR)	4
II	MARKOV RANDOM FIELD MODEL FOR PSIR	7
	A. Model	7
	B. Optimization	10
	1. Block Merging	11
	2. Region Growing	20
	C. Combatting Noise	26
	1. Low Pass Filtering	26
	2. Wavelet Denoising	27
	3. Slope Filtering	30
III	EXPERIMENTAL RESULTS	36
	A. Method of Performance Evaluation	36
	B. Computer Simulations	37
	1. IR Phantom	37
	2. Block Merging	39
	3. Region Growing	41
	4. Wavelet Denoising	45
	5. Slope Filtering	50
	C. <i>In vivo</i> Results	54
	D. Discussion	67
IV	CONCLUSION AND FUTURE WORK	74
	REFERENCES	75
	VITA	79

LIST OF FIGURES

FIGURE	Page
1	Illustration of the inversion recovery pulse and the time evolution of the longitudinal magnetization. 5
2	Two different neighborhood structures. (a) Shows a neighborhood of four closest points, (b) Shows configuration where eight closest points are neighbors. 9
3	Obtaining global optimum in a 2×2 image block using exhaustive search. The white boxes indicate phases close to 90^0 whereas the grey boxes indicate phases closer to 270^0 . Here, the third configuration in the first row gives the minimum cost and is selected as the background phase of the 2×2 block under consideration. 12
4	Background phase extraction from an 8×8 phase image using block merging: Step1. 2×2 sized image blocks are obtained by exhaustive search. Step2. 4×4 sized blocks are obtained by merging four 2×2 blocks obtained in previous step. Step3. The procedure is continued to extract the background phase from the complete image. 14
5	Formation of representative pixel vectors. Here D_H and D_V represent horizontal and vertical depths respectively. The horizontal and vertical vectors of representative pixels R_{H1}, R_{H2} and R_{V1}, R_{V2} are formed by weighted means D_H and D_V pixels respectively. 16
6	Adaptive depth estimates for horizontal and vertical depths for a quarter of a brain image. The depths are indicated by opaque white color and are superimposed on the phase map of the inversion recovery image. (a) and (b) show the horizontal and vertical depth estimates for the image respectively. 17
7	Flow-chart indicating the steps involded in block merging method for PSIR. Here l is the smallest integer such that $2^l \geq N$ where the size of the image is $N \times N$ 19

FIGURE	Page
8	Circular growth trajectory for region growing. The optimally combined center pixels serve as a reliable starting area from which the region is grown. The numbers indicate the sequence in which the circular path is traversed. 21
9	(a) First order neighborhood, (b) Second order neighborhood, (c) Third order neighborhood. 24
10	Region growing (a) Original phase map, (b) Locally smooth regions extracted using region growing with first order neighborhood, (c) Consistent background phase extracted after repeating region growing with second and third order neighborhoods. 25
11	Low pass filtering before phase sensitive reconstruction (a) PSIR image without low pass filtering, (b) PSIR image with low pass filtering. As seen, the low pass filtering is not successful in removing all the errors due to noise. 28
12	PSIR result generated with and without using wavelet denoising. (a) Digitally generated phantom image without background phase modulation and noise added to it, (b) Real part of complex image shows the effect of phase modulation and noise, (c) PSIR using region growing algorithm without denoising shows two failure sites which appear in different shade due to wrongly assigned polarity, (d) Phase sensitive reconstruction after wavelet denoising. 31
13	Diagrammatic representation of phase-slope in a small area of a complex IR image. (a) Portion of tissue with short T1 and hence positive polarity, (b) Portion of area between tissues with short and long T1 values contains, (c) Tissue with long T1 and hence negative polarity. Unlike the vector sum is unpredictable at the interface due to cancelation of opposing phases, the phase-slope value is consistent in all the cases. Source: [15]. 33
14	Slope filtering. Here the vector A is replaced by its projection A_{proj} on the phase-slope vector. The result is a form of averaging on the phase to minimize the effect of noise without disturbing the polarity information. 35

FIGURE	Page
15	Flow chart of complex IR phantom generation. The bubbled arrows indicate the user controllable inputs. 38
16	Phantom image. (a) Phantom template without background phase modulation and noise, (b) Background phase modulation pattern. The pattern is cropped at the corners due to rotation by 45^0 , (c) Magnitude image. Notice that the star and the square with different polarity appear in the same shade in this image due to similar magnitude, (d) Real part of complex phantom image displays the effect of background phase modulation. 40
17	Image reconstruction using block merging algorithm. (a) True image, (b) Real image displaying background phase modulation, (c) Magnitude reconstruction, (d) PSIR image obtained using block merging algorithm. 42
18	Error vs. SNR plot for the block merging algorithm. The background phase variation in all the cases was maintained constant with maximum variation rate of 0.026 cycles per pixel. 43
19	Phase sensitive reconstruction of image with very high background phase variation rate using block merging algorithm. (a) True image, (b) Real image displaying rapid background phase variations, (c) Magnitude reconstruction, (d) PSIR Image obtained using block merging algorithm. 44
20	Image reconstruction of image with high background phase variation rate and moderately low SNR using region growing algorithm. (a) True image, (b) Real image displaying background phase modulation. The white box indicates the maximum phase variation region with 2 phase cycles covered in 28 pixels, (c) Magnitude reconstruction, (d) PSIR image obtained using block merging algorithm. 46
21	Error vs. SNR plot for the region growing algorithm. The background phase variation in all the cases was maintained constant with maximum variation rate of 0.026 cycles per pixel. 47
22	Error vs. background phase variation rate plot for the region growing algorithm. The image SNR in all the cases was maintained at a constant level of 40 dB. 48

FIGURE	Page	
23	Comparative error vs. SNR plots for region growing algorithm with and without wavelet denoising. Here the background phase variation rate for each case was set at 0.035 cycles per pixel.	49
24	Comparative PSIR result sets generated with and without using denoising for high rate of background phase variations. (a) Phantom image without phase modulation and noise; (b) Real part of complex image shows different phase variation rates at different locations; (c) PSIR using region growing without denoising shows failure due to high frequency background phase; (d) PSIR after denoising the phase image.	51
25	Plot of percentage error vs. maximum spatial variation measured in cycles per pixel. Errors increase with frequency of background phase variations. Image SNR of 27.5 dB was used for simulations. . .	52
26	Improvement in region growing algorithm using slope filtering. Here background phase variation rate is 0.065 cycles per pixel and the image SNR is 17.9 dB. (a) Phantom image without phase modulation and noise; (b) Real part of complex image; (c) PSIR using region growing without slope filtering; (d) PSIR with slope filtering.	53
27	Phase sensitive reconstruction of IR brain image using block merging algorithm (a) Real part of complex IR image; (b) Magnitude reconstruction; (c) PSIR image.	55
28	Phase sensitive reconstruction of IR brain image using block merging algorithm (a) Real part of complex IR image; (b) Magnitude reconstruction; (c) PSIR image.	56
29	Phase sensitive reconstruction of IR brain image using region growing algorithm (a) Real part of complex IR image; (b) Magnitude reconstruction; (c) PSIR image.	57
30	Phase sensitive reconstruction of IR brain image using region growing algorithm (a) Real part of complex IR image; (b) Magnitude reconstruction; (c) PSIR image.	58

FIGURE	Page
31	Use of slope filter to achieve successful reconstruction. (a) Real part of complex IR image; (b) Magnitude reconstruction; (c) Phase sensitive reconstruction fails in a part of image due to noise; (d) Successful phase sensitive reconstruction by treating the image data with slope filter before reconstruction. 59
32	Phase sensitive reconstruction of data acquired using a fast spin-echo sequence on a 15 Tesla MR scanner (a) Real image; (b) Magnitude reconstruction; (c) PSIR image. 60
33	Phase sensitive reconstruction of data acquired using a fast spin-echo sequence on a 15 Tesla MR scanner (a) Real image; (b) Magnitude reconstruction; (c) PSIR image. Note that the magnitude reconstruction in this case results in a contrast inversion between ventricles and the surrounding structure. 61
34	Phase sensitive reconstruction of data acquired using a fast spin-echo sequence on a 15 Tesla MR scanner (a) Real image; (b) Magnitude reconstruction; (c) PSIR image reconstructed with inverted polarity. This example demonstrates the problem of global polarity determination in the PSIR reconstruction. 62
35	Phase sensitive reconstruction of a low SNR MR data acquired using 8 coils using a fast spin-echo sequence. (a) Real image; (b) Magnitude reconstruction; (c) PSIR image. 63
36	Phase sensitive reconstruction of 8 coil data acquired using fast spin-echo sequence. The imaging time was 300ms. (a) Real image; (b) Magnitude reconstruction; (c) PSIR image. 64
37	Phase sensitive reconstruction of 8 coil data acquired using fast spin-echo sequence. The imaging time was 300ms. The input image SNR was 32dB. (a) Real image; (b) Magnitude reconstruction; (c) PSIR image. 65
38	Phase sensitive reconstruction of IR brain image. (a) Real part of complex image; (b) Magnitude reconstruction; (c) Phase sensitive reconstruction. 66

FIGURE	Page	
39	<p>Analysis of PSIR failure - 1. (a) Phase map of input image; (b) Extracted background phase by PSIR algorithm. Though the polarity information has been eliminated in the phase map as required for successful background phase extraction, a large portion extracted background phase is inconsistent with the rest of the phase map; (c) Zoomed-in failure location boxed using a black square in (b). Note that here the failure starts at a single pixel (116, 116) and spreads in a considerable portion of the phase map.</p>	69
40	<p>Analysis of PSIR failure - 2. (a) Phase of pixels in input image surrounding pixel at location (116, 116). Pixel (116, 116) being the corner starting point in the growth trajectory, its decision is made only from pixel (117, 117). The arrows indicate the pixels used for making decision and the numbers indicate the sequence in which the shown pixels phases are determined. Pixels with similar angles are shown in similar shades; (b) Result of region growing.</p>	70
41	<p>Unsuccessful reconstruction of a gradient echo brain image acquired using a 3 Tesla MR scanner. (a) Real image; (b) Failed phase sensitive reconstruction. White box in the boundary region shows the failure location; (c) Phase-map. The white box indicated the region surrounding the failure site; (d) Thresholded phase difference between phases of neighboring pixels. The regions with a difference between 75° and 105° between neighboring pixels are indicated. The white box indicates the failure location crowded with pixels having almost 90° phase difference between each other.</p>	72
42	<p>Phase sensitive reconstruction of gradient echo data. (a) Real part of complex gradient echo image; (b) Unsuccessful phase sensitive reconstruction. The black arrow shows the beginning of reconstruction failure at a failure site; (c) Phase-map of the image. The white box indicated the region surrounding the failure site; (d) Thresholded phase difference between phases of neighboring pixels. The regions with a difference between 75° and 105° between neighboring pixels are indicated. The white arrow indicates the failure site.</p>	73

CHAPTER I

INTRODUCTION

A. Magnetic Resonance Imaging

Magnetic Resonance Imaging (MRI) uses a powerful magnetic field and precisely programmed radio frequency (RF) pulses to visualize tissues without dissecting the body. Human body has plenty of hydrogen in the form of water and fat. Hydrogen nucleus contains an unpaired proton which plays a major role in the generation of magnetic resonance (MR) signal. The proton being a charged particle spins around its axis. The spins of protons in a body are randomly distributed resulting in a net near-zero spin. When subjected to an external static magnetic field B_0 in an MR scanner, these spins align in the direction of the magnetic field to produce a non-zero net spin. The alignment of spins remains in this equilibrium state until it is disturbed by another magnetic field B_1 . When B_1 field is suddenly removed, the spins wobble and go back to their equilibrium state. This can be compared to a compass needle subjected to the field of a magnet. When the magnet is suddenly removed, the needle wobbles and settles down in its equilibrium state of alignment with earth's magnetic field. This wobbling of the spins creates electromagnetic signals which are detected as the MR signals.

MRI has established itself as an important diagnostic and visualization technique for medical and research communities. MRI is considered ideal for diagnosing multiple sclerosis, tendonitis, tumors of pituitary gland and brain, infections of spine, brain and joints. It is a very useful technique in visualizing and evaluating torn ligaments, bone tumors, herniated cysts in spine and masses of soft tissues. Research on diagnosis

The journal model is *IEEE Transactions on Automatic Control*.

of strokes in early stages using MRI has also yielded promising results. The fact that MRI systems do not use ionizing radiation or radioactive chemicals makes it a much safer imaging technique as compared to computer axial tomography (CAT) and positron emission tomography (PET) scans. Also, while CAT is limited to axial plane, MRI can capture images in axial, sagittal as well as coronal plane without moving the patient.

MR signals are acquired using precisely designed radio frequency pulse sequences. Depending on the application, the imaging sequences can modulate the net magnetization of the imaged body to reveal important information like contrast between tissues, flow of blood, etc. Inversion Recovery (IR) is one such pulse sequence that can be used to enhance T_1 contrast between the imaged tissues.

B. Inversion Recovery

Inversion recovery is a magnetization preparation technique in which a 180° RF pulse is used to invert the longitudinal magnetization before the 90° excitation pulse. An interesting feature of IR is that it provides a T_1 contrast enhanced by a factor of two as compared to the conventional spin-echo sequence. An IR pulse sequence is typically specified by three parameters:

1. Inversion Time (TI): The time between the 180° inversion pulse and the 90° imaging pulse.

2. Repetition Time (TR): The time duration between two successive IR pulse sequences.

3. Echo Time (TE): Echo is an MR signal generated when the transverse magnetization is refocused and results in a measurable signal due to re-alignment of spins. The time between the 90° pulse and the peak of the echo signal is called the echo

time.

IR pulse sequence is widely used for fluid or fat suppression in the imaged tissue. A number of different variants of IR have been proposed for tissue suppression. Some of these methods tweak the IR imaging parameters while others add additional pulses to the IR sequence. In short tau (τ) inversion recovery (STIR), the TI is set to $T_1 \ln 2$, where T_1 is the spin-lattice relaxation time of the tissue component to be suppressed. It is used to suppress water or fat in the resultant image [1]. Fluid attenuated inversion recovery (FLAIR) uses long TI set to null the signal from fluid in the obtained images and is used in cerebrospinal fluid suppression [2]. By saturating fat protons prior to slice selection in IR, their signal can be made negligibly small in acquired images. This technique is called Spectral Presaturation Inversion Recovery (SPIR) [3, 4]. Inversion pulses are also used in black blood magnetic resonance angiography (MRA) for cardiovascular imaging. Here the inflowing blood signal is suppressed with respect to myocardium for better cardiac-chamber segmentation. Double-inversion recovery turbo spin echo is one such imaging sequence. IR has been found useful in numerous applications like imaging bone tumors [5], pulmonary blood flow and perfusion [6], detecting myocardial infarction [7], diagnosing acute appendicitis [8] and detection of hemorrhage in atherosclerotic plaques [9] to name a few.

If the tissue magnetization at thermal equilibrium is M_0 , then the IR image can have values from $(-M_0, +M_0)$. Since the resultant image can contain negative values, reconstruction of real part of the complex image is required in order to take the advantage of the complete contrast range.

C. Phase-Sensitive Inversion Recovery (PSIR)

Since IR image pixels can have both positive and negative values, they have associated magnitude and polarity information. These are stored in the magnitude and a phase component of the complex IR image. The phase component that stores the polarity information is called the intrinsic phase. The intrinsic phase is not readily available due to the presence of another component called the background phase. The background phase interference is a result of several factors like magnetic field inhomogeneities, off-resonance phenomena and acquisition errors [10]. Conventional magnitude reconstruction ignores the phase and hence the polarity information. As a result, it fails to realize the potential T_1 contrast increment offered by IR imaging. Figure 1 shows how the longitudinal magnetization evolves in a typical spin-echo IR pulse sequence. The 180° inversion pulse inverts the equilibrium tissue magnetization M_0 to $-M_0$. Thereafter the longitudinal magnetizations of various tissues start returning to their equilibrium states at rates depending on their T_1 relaxation times. A snap-shot of different tissue magnetizations is acquired using a 90° imaging pulse. As indicated by magnetization relaxation profiles, while IR can provide a dynamic contrast range of $(-M_0, M_0)$, the magnitude reconstruction is able to utilize a range of only $(0, M_0)$ due to loss of polarity information.

PSIR methods can provide enhanced T_1 contrast by estimating and utilizing this polarity information [10–20]. PSIR can be performed by estimating the intrinsic phase component using multiple acquisitions. Here the phase errors are estimated by acquiring another image without inversion [7, 14, 21] or with different inversion time TI [12, 13]. These methods suffer from increased acquisition time and result in patient discomfort. Moreover, they are susceptible to errors caused by spatial misregistration due to patient motion. An alternative approach is to extract the intrinsic phase

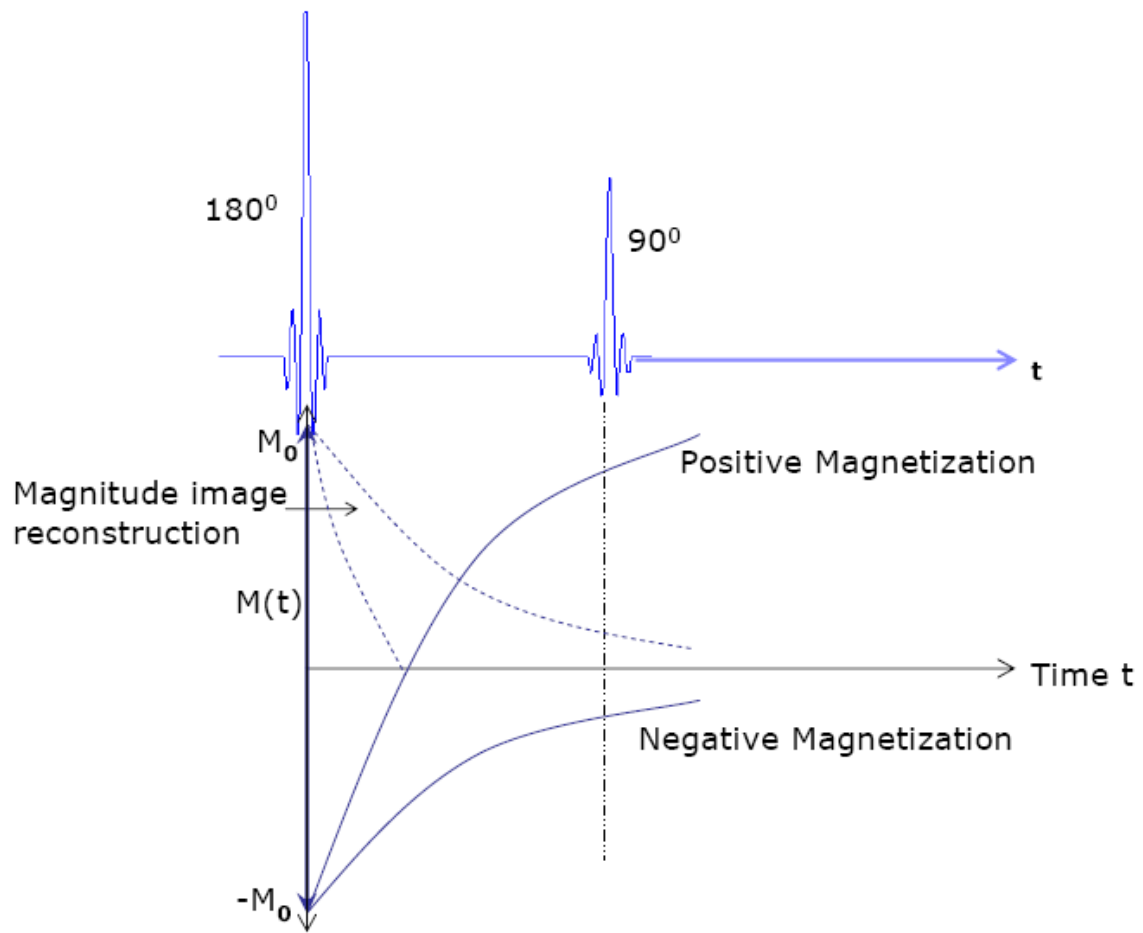


Fig. 1. Illustration of the inversion recovery pulse and the time evolution of the longitudinal magnetization.

from the available phase information from the acquired IR image [10, 11, 15, 17–20]. These algorithms exploit differing characteristics of intrinsic and background phase to extract the desired information.

A complex IR image obtained after Fourier transformation of the k-space data can be expressed as

$$I(x, y) = |I(x, y)|e^{i\Phi(x, y)} = |I(x, y)|e^{i(\theta(x, y)+s(x, y))} \quad (1.1)$$

where $|I(x, y)|$ is the magnitude and $\Phi(x, y)$ is the phase [11]. The total phase $\Phi(x, y)$ can be considered to be composed of two different components: $\theta(x, y)$, the smoothly varying background phase and $s(x, y)$, the intrinsic phase which is 0 or π and indicates polarity information [17]. The intrinsic phase $s(x, y)$ can be estimated using the information provided by the total image phase $\Phi(x, y)$ and using the characteristic differences between $s(x, y)$ and $\theta(x, y)$. Using this principle, two different approaches to enhance the T_1 contrast range of IR images have been developed in this research.

CHAPTER II

MARKOV RANDOM FIELD MODEL FOR PSIR

In the presented methods, a statistical model based on Markov Random Fields (MRF) is used to model the smoothly varying component of the image phase. Reliable reconstruction is provided using the model by adaptively incorporating the phase correlations among many pixels.

A. Model

A *random field* is a stochastic process defined on a two-dimensional set and the random fields possessing Markov property are known as *Markov random fields*. For a *Markov chain* X_k satisfying first order neighborhood,

$$P(X_n = x_n | X_k = x_k, k \neq n) = P(X_n = x_n | X_{n-1} = x_{n-1}, X_{n+1} = x_{n+1}) \quad (2.1)$$

In other words, given the values at time points $n - 1$ and $n + 1$, the conditional distribution of X_n is independent of values at all other time points. The points $n - 1$ and $n + 1$ are called neighbors of n . Thus, the conditional distribution in a Markov chain is dependent on the values at the neighboring time points only. A MRF can be thought of as an extension of a Markov chain in two dimensions. Let S be a finite rectangular two-dimensional lattice of integer points. The points in S are called sites. A MRF can be defined on S and neighbors can be defined satisfying the following conditions:

1. A site must not be a neighbor of itself
2. Symmetry condition: If t is a neighbor of s , then s is a neighbor of t

If s and t are neighbors, we write $s \sim t$. Now, neighborhood N_s of s can be defined as

$$N_s = \{t \in S : t \sim s\} \quad (2.2)$$

Figure 2 shows two different neighborhood structures.

For PSIR reconstruction, it is necessary to separate the background phase and the intrinsic phase. This method achieves this by estimating the background phase modeled using MRF [22]. MRF models have been successfully applied as a ‘‘smoothness’’ constraint for solving many computer vision problems [22, 23, 24]. Background phase encountered in IR imaging is a slow varying function and the MRF can be expected to adequately model the spatial correlation among pixels in a chosen neighborhood. Specifically, the background phase map $\Theta = \theta(x, y)$ is estimated by maximizing the a posteriori probability $P(\Theta|\Phi)$, where Φ is the observed phase of the complex image.

We maximize this probability by minimizing a cost function, also called the *potential function*. This potential function is defined in such a way that reliable pixels, identified by high signal strength and low gradient, are given more weight in making the decisions. This provides robustness to the algorithm against noise. We define this potential function as

$$\varepsilon(\Theta) = \sum_{(x,y)} \sum_{(\hat{x},\hat{y}) \in N(x,y)} d(\theta(x,y), \theta(\hat{x}, \hat{y})) \frac{\min\{|I(x,y)|, |I(\hat{x}, \hat{y})|\}}{\max\{G(x,y), G(\hat{x}, \hat{y})\}} \quad (2.3)$$

Here $d(.,.)$ measures the angular difference, $N(x,y)$ is the neighborhood and $G(x,y)$ is the phase gradient at point. We propose to calculate the angular difference using

$$d(\theta_1, \theta_2) = |\text{mod}(\theta_1 - \theta_2 + \pi, 2\pi) - \pi| \quad (2.4)$$

This definition gives $d(0, 2\pi)$ as 0 and not 2π . The gradient $G(x,y)$ is calculated as the angular difference in a 3×3 local neighborhood of $\theta(x,y)$ and using $d(.,.)$ as the

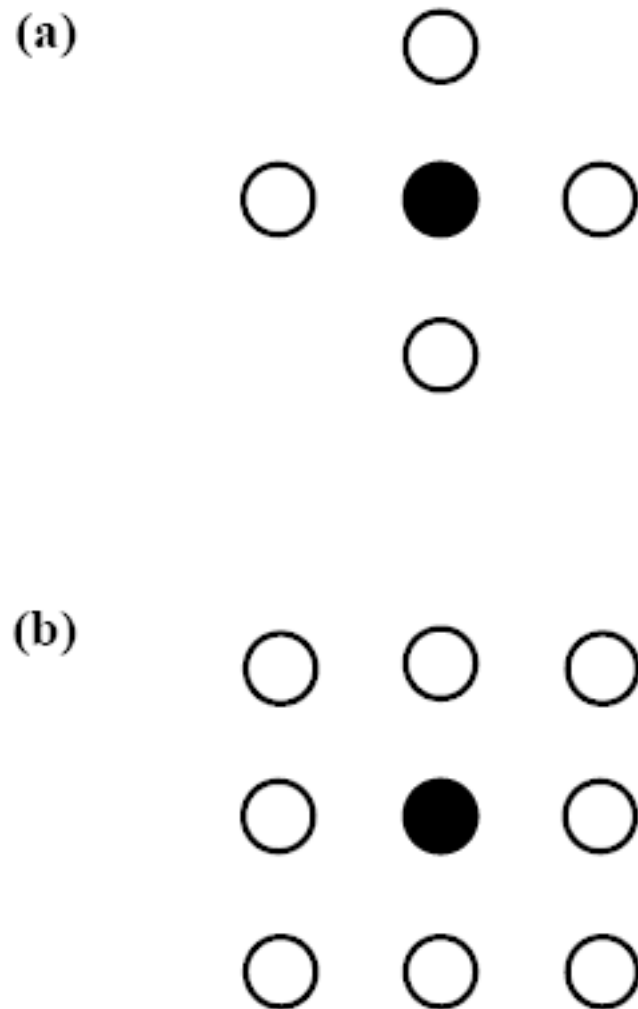


Fig. 2. Two different neighborhood structures. (a) Shows a neighborhood of four closest points, (b) Shows configuration where eight closest points are neighbors.

metric.

$$G(x, y) = \sum_{m=-1}^1 \sum_{n=-1}^1 d(\theta(x, y), \theta(x - m, y - n)) \quad (2.5)$$

The second term in 2.3 is a weighting factor which emphasizes pixels with large intensity and small phase gradient. Such pixels usually have large SNR. Noisy pixels are characterized by high phase gradient and usually have low intensity. Thus, the described weighing gives more weight to pixels that are deemed reliable. The size of the neighborhood $N(x, y)$ should be chosen in accordance with the degree of smoothness of the phase map.

B. Optimization

The problem of PSIR is that of finding polarities associated with each of the image pixels. This polarity information is stored in the intrinsic phase component of the total phase. The intrinsic phase takes the values 0 and π corresponding to the positive and negative polarities respectively. The intrinsic phase can be determined by estimating and subtracting the background phase from the total phase. Background phase, being a slow varying phase component, has high correlation among pixels in a small neighborhood. Consequently, adjacent pixels with opposite polarities will have very similar background phase values and will have 180° phase difference between their intrinsic phases. As a result, the total phases of these pixels will exhibit about 180° phase difference. The background phase of the two adjacent pixels can be extracted by comparing the phase difference between the two pixels with and without adding 180° to one of the pixel phases. The combination to give the minimum phase difference is selected and in this state, phases of the pixels are their background phases. Thus, we extract the background phase by eliminating the polarity information. With these details in perspective, the optimization of a 2×2 image block can be explained using

fig. 3.

In this example, the cost is defined simply as the sum of the circular angular differences between all the adjacent pixels. Since there are $2 \times 2 = 4$ pixels, one may tend to think that a total of $2^4 = 16$ combinations need to be tested. But half of these combinations being 180° flipped versions of the other half, give the same costs. Hence all the possible costs can be found by testing 8 combinations. In general, for an $N \times N$ image, 2^{N^2-1} combinations need to be tested. As indicated in the figure, when the phases are aligned, they give minimum costs and represent the background phase.

The solution obtained as described above by testing all the possibilities is known as the *global optimum*. But obtaining global optimum is computationally prohibitive even for a moderately sized image. Two different approaches have been proposed in this thesis to efficiently obtain a sub-optimal solution which approximates the global optimum. The first approach is a “divide-and-conquer” approach. The image is divided into small regions and optimum solutions for these regions is obtained by an exhaustive search. Thereafter, these optimum blocks are merged in such a way that their optimality is preserved. The second approach obtains efficient solution by region growing. The algorithm starts from the center and expands a growth region towards the boundaries. The polarities of the newly added pixels are determined by those of its neighboring pixels that have already been visited.

1. Block Merging

The basic idea of the block merging algorithm is to divide-and-conquer the optimization problem. Specifically, the phase image is first divided into 2×2 blocks and each of these blocks are optimized by an exhaustive search. For an $N \times N$ image, this results in $N/2 \times N/2$ blocks of size 2×2 that are smooth inside their own boundaries

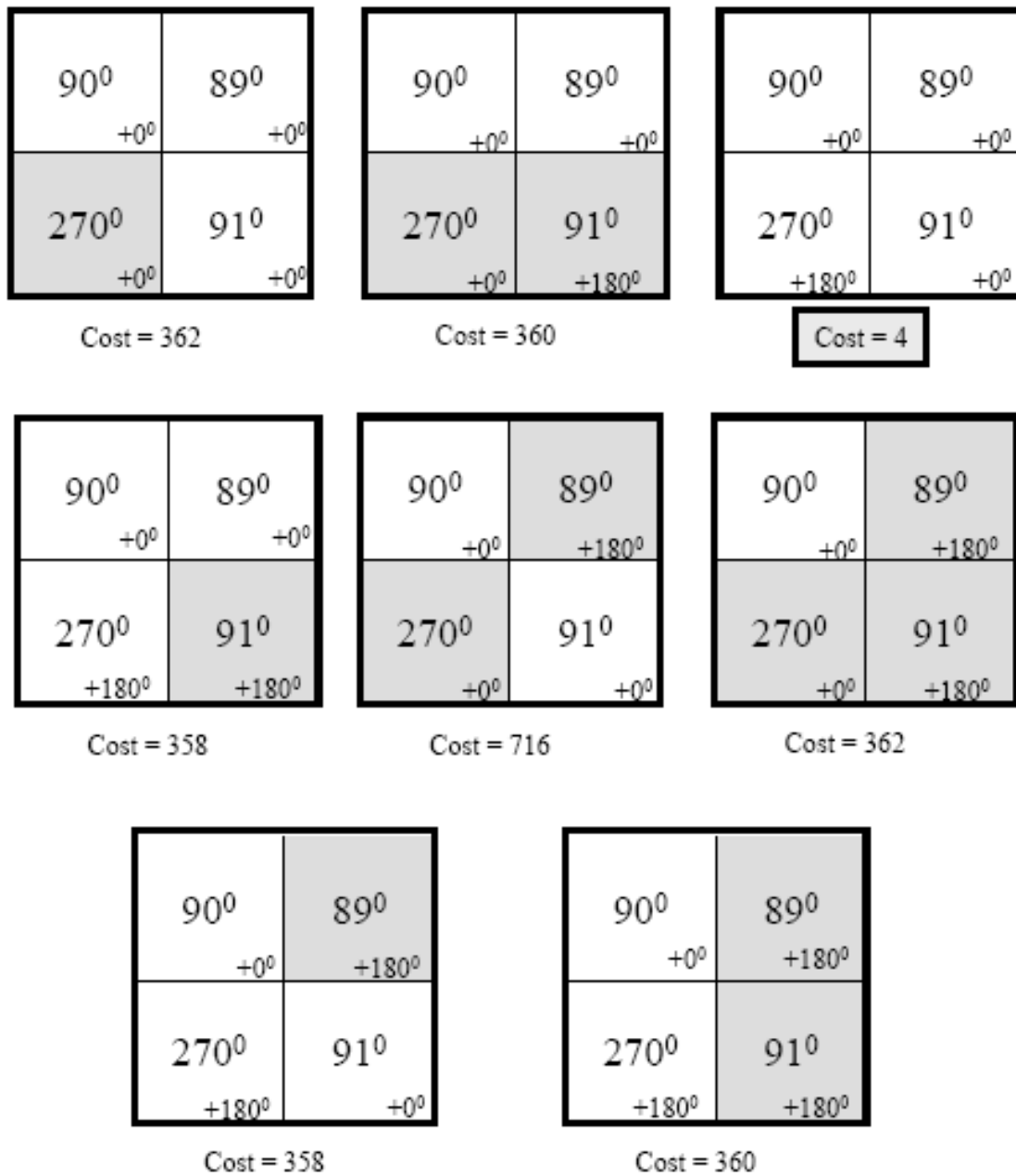


Fig. 3. Obtaining global optimum in a 2×2 image block using exhaustive search. The white boxes indicate phases close to 90° whereas the grey boxes indicate phases closer to 270° . Here, the third configuration in the first row gives the minimum cost and is selected as the background phase of the 2×2 block under consideration.

but may be 180° out-of-phase with the adjacent blocks. In the next step, neighboring blocks are combined to give 4×4 blocks, each with smooth phase variations and hence containing extracted background phase. This procedure is repeated to give 8×8 blocks, 16×16 blocks, and so on, until the whole field of view (FOV) is combined in a single block. Here every step combines four $n \times n$ sized blocks processed by the previous step to generate a phase map with $2n \times 2n$ sized smooth phase blocks. Hence, 2^l steps are required to extract the background phase in an image with $N \times N$ pixels where l is the smallest integer such that $2^l \geq N$. The procedure is explained in fig. 4.

The key to the performance of the algorithm lies in the way the blocks are combined in each stage. Suppose that each sub-block has $n \times n$ elements. Then each sub-block in a four block cluster has n boundary pixels touching the horizontal neighbor and n boundary pixels touching the vertical neighbor. Adjacent pixels at the boundary of two touching blocks can be considered as neighbors in calculating the potential defined in 2.3. The combination giving the minimum potential is selected for combining the blocks. In this process, we flip the phases of all the pixels in a particular sub-block, if required, for achieving the optimum. This maintains the relative phase differences of the pixels inside a sub-block intact and thus preserves the local optimum inside the sub-block.

In noisy MR Images, incorrect optimum combinations may be found if the boundary pixels of a sub-block are noisy. To improve the reliability of the algorithm, instead of considering just the adjacent pixels on the boundaries of combining blocks, we construct *representative pixels* to represent the phases at the sub-block boundaries. The representative pixel values are calculated as the weighted mean of D pixels at the boundaries, where D is the *depth factor* and depends on smoothness of the total phase. Weighted averaging reduces the effect of noise when combining the blocks. Since the

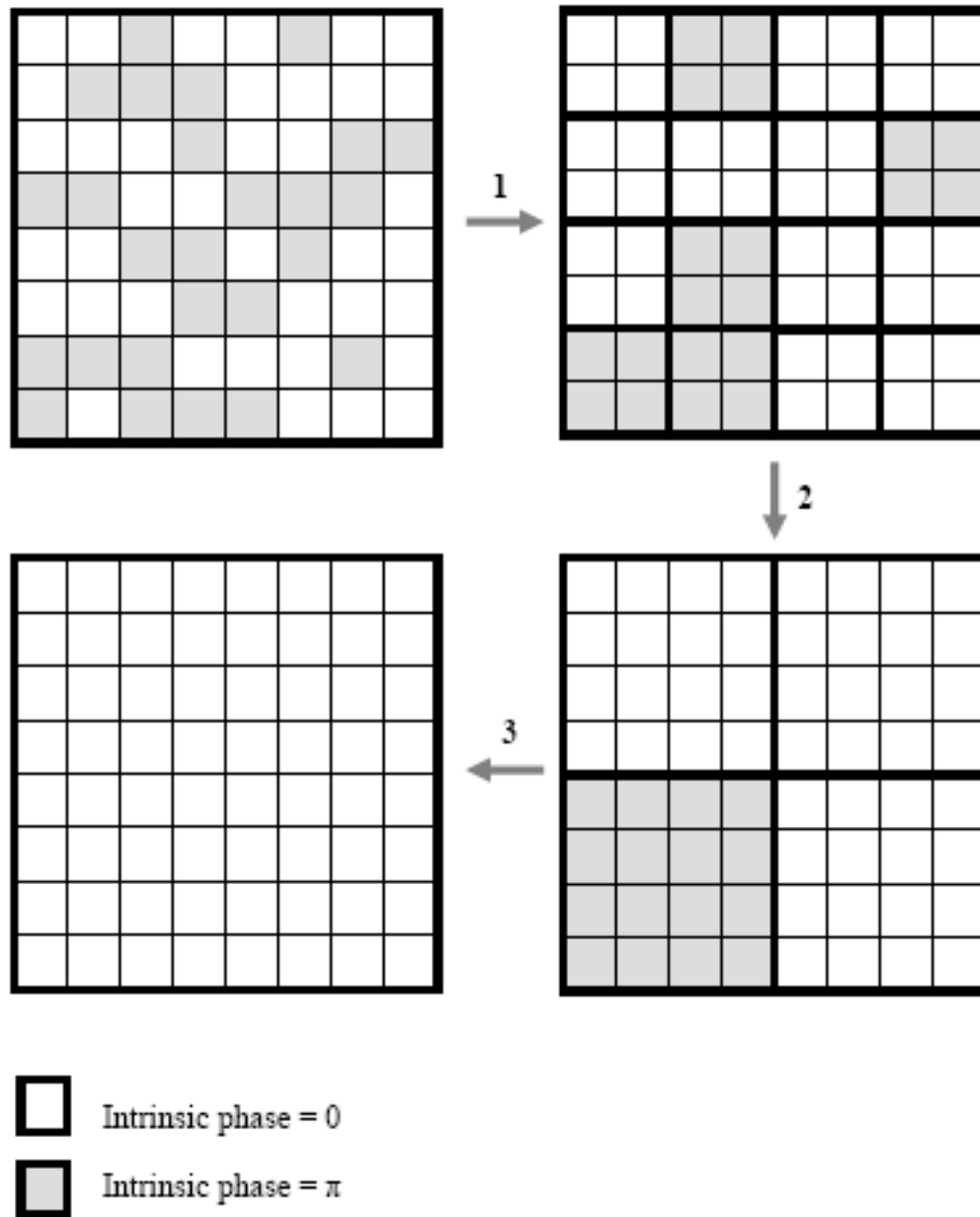


Fig. 4. Background phase extraction from an 8×8 phase image using block merging: Step1. 2×2 sized image blocks are obtained by exhaustive search. Step2. 4×4 sized blocks are obtained by merging four 2×2 blocks obtained in previous step. Step3. The procedure is continued to extract the background phase from the complete image.

phase variation rates along the horizontal and vertical directions can be different, different depths can be used when considering horizontal and vertical boundaries of a sub-block. Figure 5 explains the basic concept of representative pixels formation.

The rates of total phase variation along horizontal and vertical directions may vary with each row and column. The idea of weighted averaging is to minimize the effect of noise so that the representative pixel at the boundary truly represents the phase at sub-block boundary for a particular row or column. In low variation rate regions, higher depth is preferable. However, in high variation rate regions, averaging for a large depth may deviate the representative pixel value from the actual phase at the boundary. Also, averaging pixels of opposite polarity or pixels completely in noise regions may result in erroneous estimates. This necessitates the use of different depths for each row and column in a sub-block. These depths are adaptively calculated by estimating the phase variation rates near the boundaries of each sub-block. Figure 6 shows the adaptive depth estimation for a quarter of an inversion recovery brain image. For adaptive depth estimation, first the horizontal and vertical gradient images are calculated for the phase map using

$$G_{Horiz}(x, y) = d(\arg\{I(x, y)\}, \arg\{I(x + 1, y)\}) \quad (2.6)$$

$$G_{Vert}(x, y) = d(\arg\{I(x, y)\}, \arg\{I(x, y + 1)\}) \quad (2.7)$$

where $d(., .)$ is the circular angular difference calculated as described in 2.4 and $\arg\{.\}$ is the argument. The gradient images are then thresholded and converted to binary maps. The threshold levels between $\pi/6$ and $\pi/4$ are found to give good results. The idea is to avoid averaging when either of the following is encountered

- Noise pixels
- Pixels with different polarity information

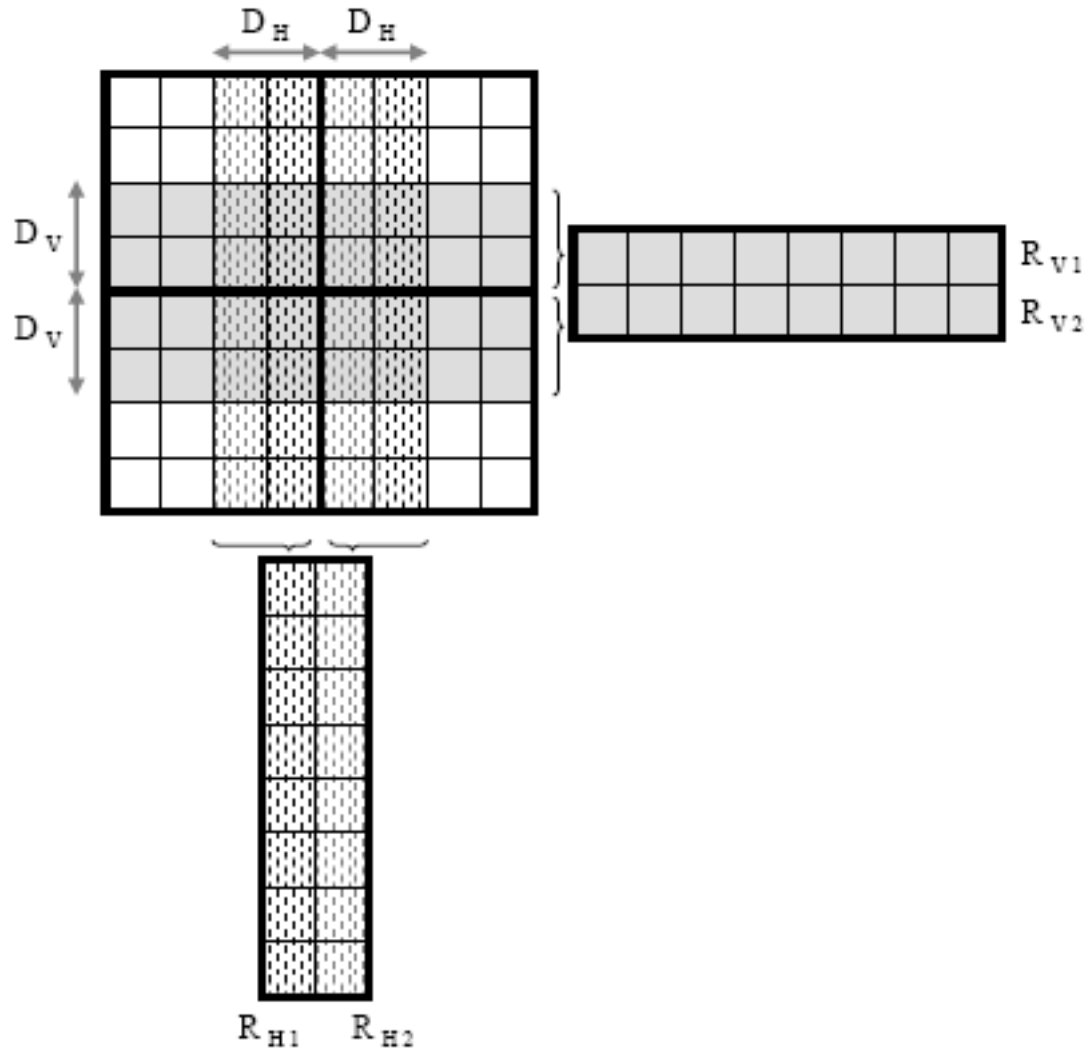


Fig. 5. Formation of representative pixel vectors. Here D_H and D_V represent horizontal and vertical depths respectively. The horizontal and vertical vectors of representative pixels R_{H1}, R_{H2} and R_{V1}, R_{V2} are formed by weighted means D_H and D_V pixels respectively.

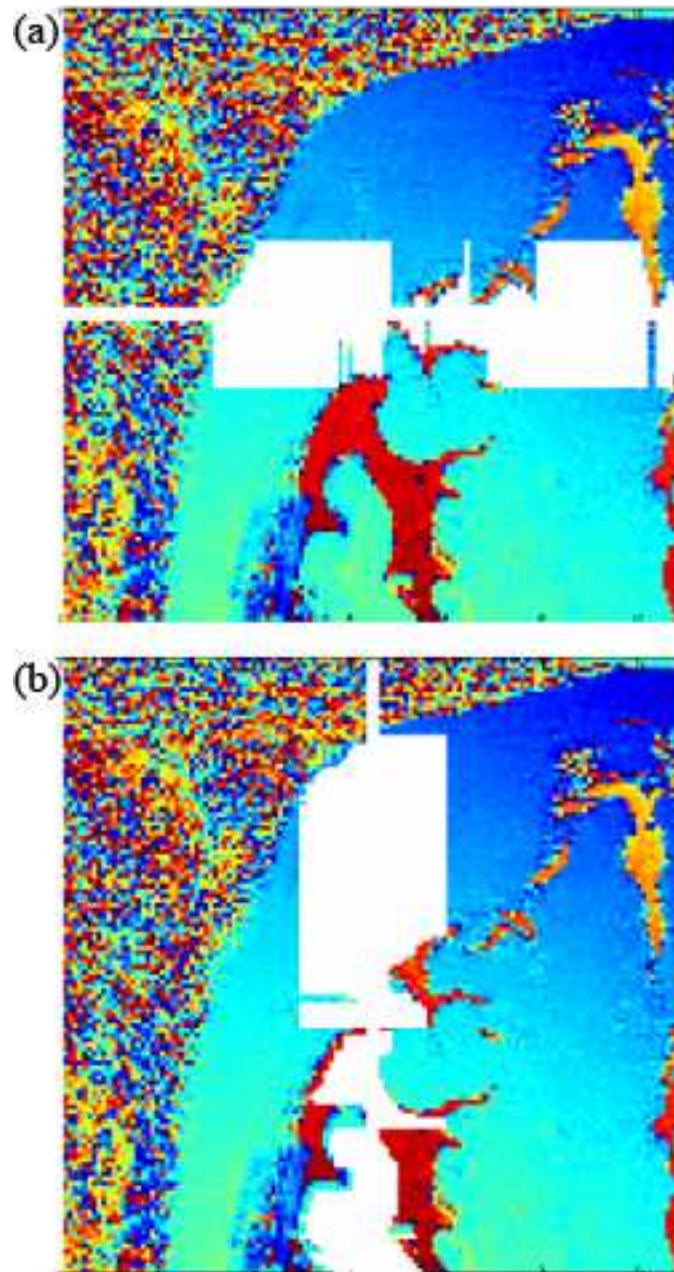


Fig. 6. Adaptive depth estimates for horizontal and vertical depths for a quarter of a brain image. The depths are indicated by opaque white color and are superimposed on the phase map of the inversion recovery image. (a) and (b) show the horizontal and vertical depth estimates for the image respectively.

- High phase gradients

Here noise pixels refer to the pixels located in noise areas outside the boundary of the object of interest. Since these areas do not contribute much MR signal, they are covered almost completely with random noise. The noise being random, the phases of these pixels have no correlation with neighboring pixels and are marked by very high phase gradients. Similarly, pixels of opposite polarity being 180° out of phase with considered pixels, are also marked by high gradients. Thus, all the above mentioned cases can be detected by observing the phase gradient map. By choosing an appropriate threshold, these cases can be isolated from noise affected areas in the object of interest which require higher averaging depths to neutralize noise. The horizontal and vertical depths are determined by scanning the thresholded horizontal and vertical gradient images respectively. The depth values are set so as to keep the noise or reverse polarity pixels from being averaged for representative pixel formation. In my implementation, the maximum allowable depth is set to 16 and the minimum depth is $\min\{2, \text{Sub-block size}\}$. The effects of minimum and maximum depths can be seen in fig. 6.

Once the depths are determined, the representative pixels are calculated by the weighted averaging of the pixels at the sub-block boundaries. Weights assigned to the pixels are directly proportional to their magnitudes $|I(x, y)|$ and inversely proportional to the gradients $G(x, y)$. The weighted averaging ensures that the representative pixels represent the average phase value of the high SNR pixels near of boundary of a considered sub-block.

The block merging method for PSIR is summarized in fig. 7 using a flow-chart. The output of the block merging procedure is the estimated background phase of the complex image. The intrinsic phase indicating polarity information is extracted by

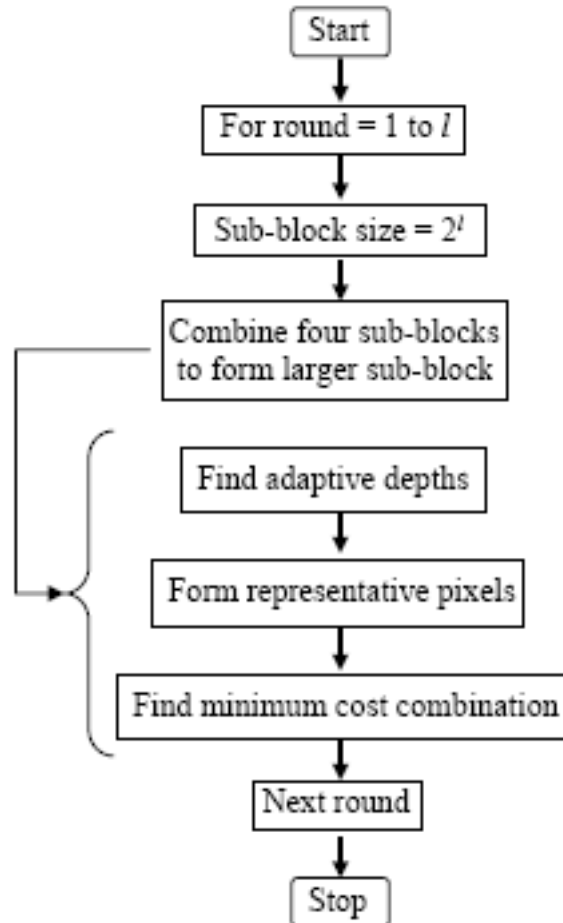


Fig. 7. Flow-chart indicating the steps involved in block merging method for PSIR. Here l is the smallest integer such that $2^l \geq N$ where the size of the image is $N \times N$.

subtracting this background phase from the total image phase. The PSIR image is obtained by combining this polarity information with the pixel magnitudes.

2. Region Growing

Region growing algorithms literally grow from a small number of image pixels and expand to cover the whole field-of-view. Generally, the starting point is chosen in a high SNR region. Since the proposed methods are developed with human brain images in mind, center of image is found to be a good starting region. Alternatively, the region can be grown from any high SNR region of the image with minor modifications in the growth trajectory. The proposed approach is much simpler as compared to the existing region growing scheme [11] and does not suffer from the limitations of the existing method [11, 20]. Since there is no phase-coherence condition controlling the region growth [11], the proposed method does not result in any information loss due to lack of growth in the image areas with high phase gradients. This also eliminates a considerable amount of manual intervention required for phase-coherence threshold selection and the need for bridge-filtering [11].

In the proposed method, first the four center pixels of the phase image are optimally combined by considering all eight combinations as discussed in the block merging method. Thereafter the region growing starts from the top left corner of the image and follows the circular trajectory described in fig. 8. That is, the trajectory goes from top left corner to top right corner, then through the bottom right, bottom left, back to top left corner and then ascends to the top left corner of the next larger loop. The new pixels are scanned according to the described trajectory. The sign of the pixel under consideration is toggled depending on the values of the pixels in the neighborhood which have already been visited. The idea is to extract the background phase from the total phase. By the basic property of the phase of an inversion recov-

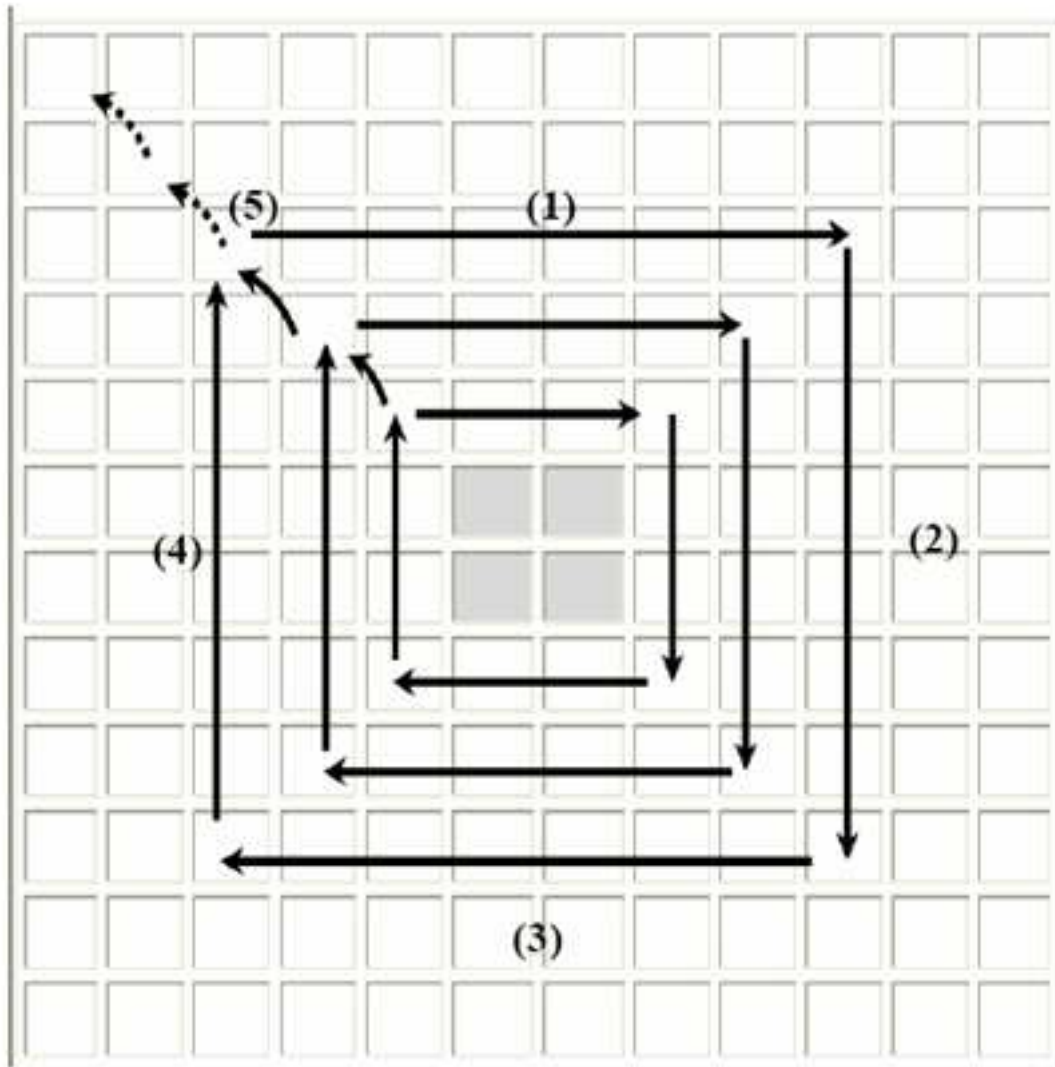


Fig. 8. Circular growth trajectory for region growing. The optimally combined center pixels serve as a reliable starting area from which the region is grown. The numbers indicate the sequence in which the circular path is traversed.

ery image, either a pixel phase is very similar to the phase of its neighboring pixel or it is 180^0 out-of-phase with its neighbor. Hence, in order to extract the background phase, if the phase of pixel under consideration

- has a small phase difference with its already visited neighbors, its sign is left unaltered.

- is almost 180^0 out-of-phase with its extracted neighbors, its sign is toggled.

By toggling the sign we are adding 180^0 to the already existing phase at the pixel. The coherence of a pixel phase with its neighbors can be measured by the dot product.

If the dot product between the complex values of two pixels is positive, the angle between them is less than 90^0 . In present context, these pixels can be said to be in phase.

Hence, to extract coherent phase, if the sum of the dot products of a pixel and its neighbors is negative, its sign is altered. In the summation, the pixels with higher reliability should be given more weight. This is accomplished by weighing the contributions by different pixels with weights inversely proportional to their gradients.

Thus, the following decision factor is calculated for each pixel under consideration

$$D(x, y) = \sum_{(x_n, y_n) \in N_v(x, y)} \frac{\langle I(x, y), I(x_n, y_n) \rangle}{|\arg\{I^2(x, y) \times I^{2*}(x_n, y_n)\}|} \quad (2.8)$$

where $N_v(x, y)$ is the set of already visited pixels in the neighborhood of the pixel at location (x, y) , $\langle \cdot, \cdot \rangle$ represents the dot product, $*$ denotes the complex conjugation, \arg is the argument and $|\cdot|$ is the absolute value. The use of $I^2(x, y)$ instead of $I(x, y)$ in the denominator ensures that the phases with polarity difference are not wrongly penalized.

$$\begin{aligned} I^2(x, y) &= \{|I(x, y)|e^{i\Phi(x, y)}\}^2 \\ &= \{|I(x, y)|e^{i(\theta(x, y)+s(x, y))}\}^2 \\ &= |I(x, y)|^2 e^{i(2\theta(x, y)+2s(x, y))} \end{aligned}$$

$$= |I(x, y)|^2 e^{i(2\theta(x, y))}$$

This is because $s(x, y) = 0/\pi$ and hence $2s(x, y) = 2\pi = 0$. Thus, the denominator in 2.8 calculates the gradient due to variations that can be attributed to noise.

The sign of a pixel is decided as follows

- If $D(x, y) \geq 0$, $\tilde{I}(x, y) = I(x, y)$
- If $D(x, y) < 0$, $\tilde{I}(x, y) = -I(x, y)$

where \tilde{I} is the image with phase equal to the extracted background phase.

In 2.8, the neighborhood used is the *first order* neighborhood. We make use of first, second and third order neighborhoods in the algorithm which we define as shown in fig. 9. Since first order neighborhood captures the coherence only between the pixels in a very small area, this may result in small locally smooth regions being extracted from the phase map. The result may look like patches of disconnected smooth phase regions. In order to extract a consistent smooth phase from the whole image, the process of region growing is repeated with the neighborhood order increased by a factor of one. This ‘knits’ the locally smooth regions to generate a consistent background phase map. Figure 10 shows the extracted locally smooth regions and the consistent background phase map obtained by neighborhood expansion.

Once the background phase is extracted, the intrinsic phase information can be obtained by subtracting it from the total phase. The real part of the complex image with just the intrinsic phase component is the desired PSIR image.

Since the region growing algorithm considers one pixel at a time in the growth trajectory, the total number of possibilities to be tested for growing a region with a defined neighborhood for an image with $N \times N$ pixels is just $2 \times N \times N$. Also, it does not require estimation of adaptive depths for every combining block as in the block merging scheme. Thus, region growing method considerably outperforms the block

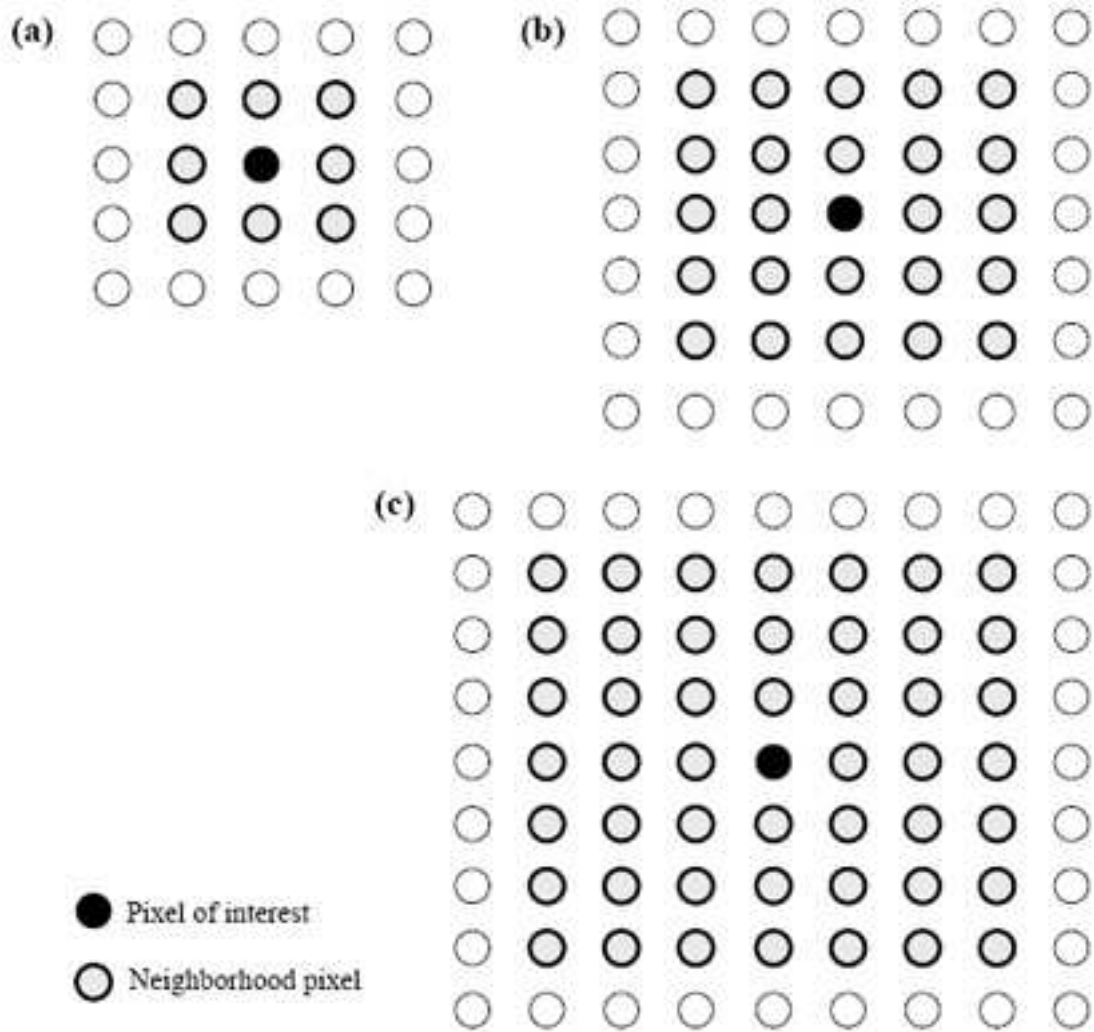


Fig. 9. (a) First order neighborhood, (b) Second order neighborhood, (c) Third order neighborhood.

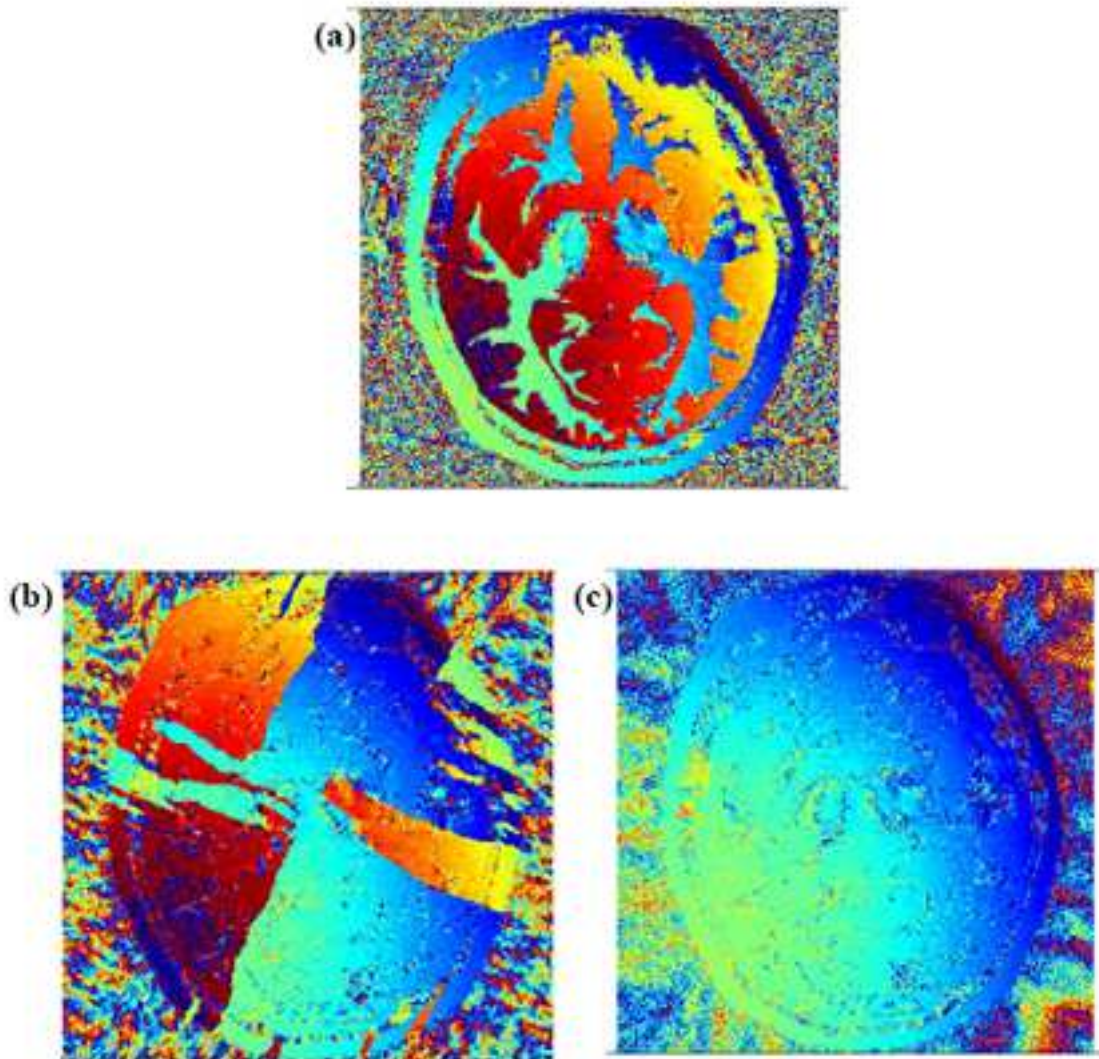


Fig. 10. Region growing (a) Original phase map, (b) Locally smooth regions extracted using region growing with first order neighborhood, (c) Consistent background phase extracted after repeating region growing with second and third order neighborhoods.

merging algorithm in terms of computational efficiency. However, block merging is more effective in neutralizing noise effects when high depths are allowable and hence, should be preferred in cases with high noise with slow phase phase variations.

C. Combatting Noise

Separating intrinsic phase from the background phase is the most important component of phase sensitive reconstruction. This process becomes difficult in presence of noise and the PSIR may fail in case of extremely noisy images. Different approaches have been considered to perform successful reconstruction in presence of noise. This section discusses these approaches and the obtained results.

1. Low Pass Filtering

Low pass filtering is the one of the most elementary approaches to reduce noise. We wish to reduce the noise on the phase image so as to facilitate the separation of intrinsic phase from the background phase. As mentioned earlier, the intrinsic phase is separable from the background phase due to its abrupt transitions between 0 and π which are not found in the smoothly varying background phase. A low pass filtering directly on the phase image can result in more harm than good. Consider the boundary between two regions of different polarity. For simplicity, assume that the background phase in both the cases is zero. So one of the regions will have the total phase = intrinsic phase = 0 whereas the other will have the total phase = intrinsic phase = π . A direct averaging on this phase map would result in generation of pixels with phase values approximately $\pi/2$. These $\pi/2$ values make it impossible to decide whether the pixel belongs to the 0 region or the π region. This often results in the failure of the PSIR algorithm. Moreover, the phase being cyclic the regions

with $-\pi$ follow the regions with phase π . An averaging in these regions also results in erroneous resultant phase values. Hence, low pass filtering cannot be directly done on the phase map.

Real and imaginary parts of a complex image, however, can be separately filtered and combined to form the low pass filtered complex image, the phase of which has less noise as compared to the unfiltered image. Since low pass filtering results in resolution reduction, the resultant PSIR image shows a decrease in resolution. The resolution reduction can be avoided if the phase is filtered using the above described method and is then combined with the original image magnitudes before further processing. If \hat{I} is the phase filtered image, it is obtained from original image I as follows

$$\hat{I}(x, y) = |I(x, y)|e^{i \times \arg\{\frac{1}{9} \sum_{m=-1}^1 \sum_{n=-1}^1 I(x+m, y+n)\}} \quad (2.9)$$

Figure 11 presents the result of low pass filtering the input image before performing the phase sensitive reconstruction. The figure demonstrates that while low pass filtering is able to remove a reconstruction error on one side of the image, it fails to do so on the other side. Low pass filtering is found to be useful in removing errors caused due to noise in a region with consistent polarity. For removing errors due to noise at boundaries of different polarity regions, a more sophisticated approach is required.

2. Wavelet Denoising

Wavelet domain denoising has been used by image processing community since quite some time. A recent denoising technique utilizing contextual hidden Markov models (CHMM) in wavelet domain [25] has been used here. The failure of a PSIR algorithm is a result of its inability to extract intrinsic phase due to either heavy noise or high variation rates of background phase information. It has been experimentally

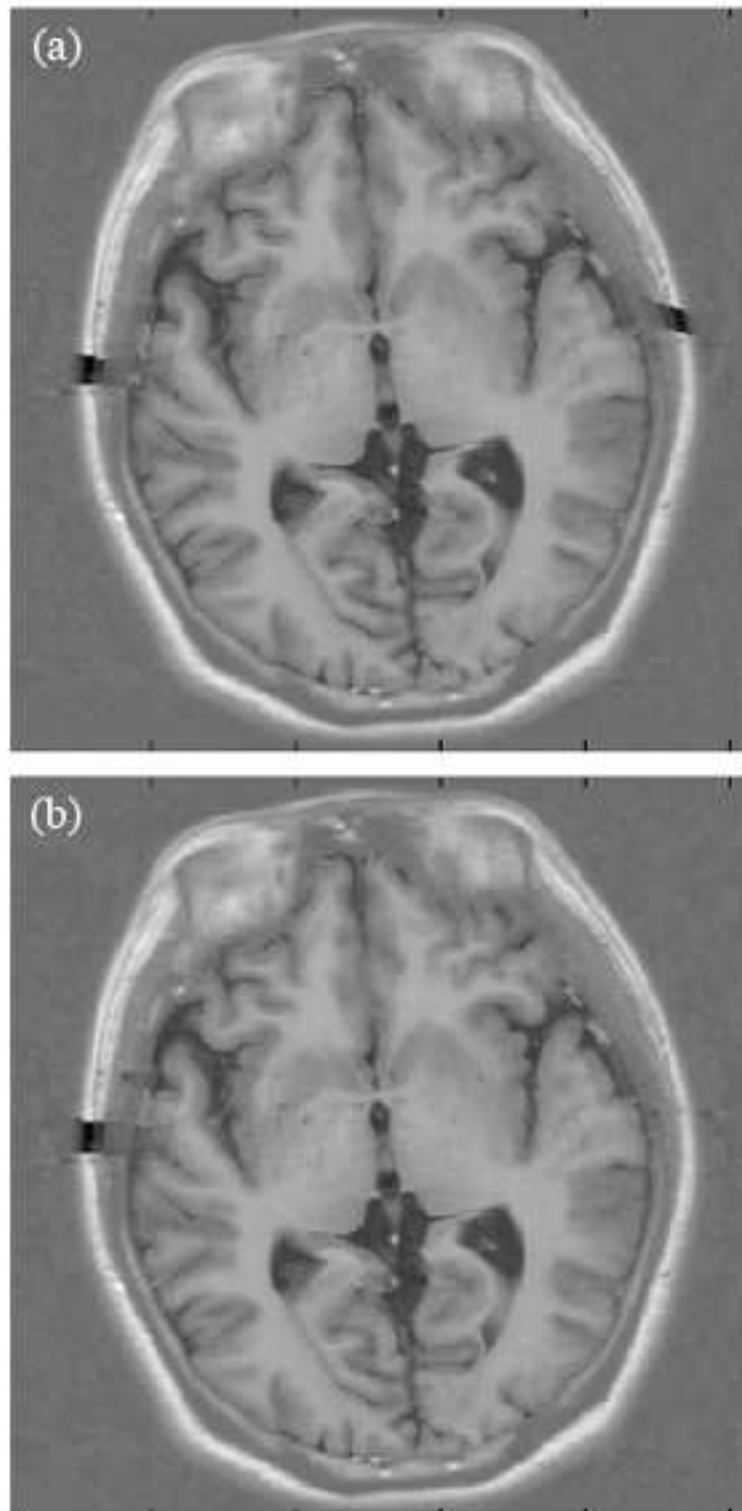


Fig. 11. Low pass filtering before phase sensitive reconstruction (a) PSIR image without low pass filtering, (b) PSIR image with low pass filtering. As seen, the low pass filtering is not successful in removing all the errors due to noise.

found using computer simulations that the wavelet denoising scheme [25] helps the proposed PSIR methods handle much noise and background phase variation rates. Thus, robustness of the proposed schemes is found to improve when this denoising technique is used. Also, the increase in errors when the image SNR is reduced is much lower when the denoising algorithm is used.

As explained in the previous section, due to cyclic nature of phase, denoising cannot be applied directly on the phase image. Hence, the real and imaginary parts are separately denoised. Doing so has a secondary benefit of providing a better reconstructed image due to the fact that denoised MR image displays better SNR and improved contrast-to-noise ratio (CNR) [26].

The denoising algorithm used here [25] captures the dependencies in wavelet coefficients through their hidden states using multidimensional mixture models in which hidden states exhibit Markov dependency structure. Using an iterative Expectation Minimization (EM) algorithm, the HMM model is first trained to adjust its parameters according to the observed wavelet coefficients. Context vectors are formed as functions of wavelet or scaling coefficients. Contexts help incorporate dependencies into HMMs efficiently. For denoising an image, the wavelet coefficients of the image are modeled using a two zero-mean component Gaussian mixture. The CHMM is trained on noisy wavelet data to estimate the hidden state probabilities of the signal and the mixture variances. Once the estimates of the denoised wavelet coefficients are calculated, an inverse wavelet transform gives the denoised image. The details of the algorithm can be found in [25].

The PSIR with denoising is done in the following steps:

1. Denoised phase is generated from the complex image by separately denoising the real and imaginary parts, generating a new denoised complex image and

finding its phase.

2. PSIR is performed to extract polarity phase $s(x,y)$ from the denoised phase
3. The polarity information is combined with the non-denoised magnitude image to generate the PSIR image

Using non-denoised magnitude in the final step avoids the unnecessary side-effect of resolution reduction when the denoising algorithm is used. In extremely noisy images where noise effects surpass losses due to resolution reduction, denoised magnitude can be used. This denoised magnitude should be obtained by taking absolute value of denoised complex image obtained in step 1. This is because the Gaussian noise assumption is valid only when denoising is done separately on real and imaginary parts [27]

Figure 12 shows a typical comparative result with and without using denoising. As shown, the failure of the PSIR algorithms in presence of heavy noise can be prevented by the use of the discussed wavelet denoising scheme. Moreover, the resultant PSIR image with denoising displays better SNR and contrast as compared to the non-denoised image. An detailed account of the improvement obtained by using denoising is presented in the results section.

3. Slope Filtering

Denoising phase using denoising performed on real and imaginary parts of an image is an indirect approach to phase denoising. A much efficient and direct approach is slope filtering. The idea is very similar to that of Borrello et al. [15]. However, it has been modified to retrieve the polarity information lost during slope calculation [15]. This makes it useful for phase denoising applications without loss of polarity.

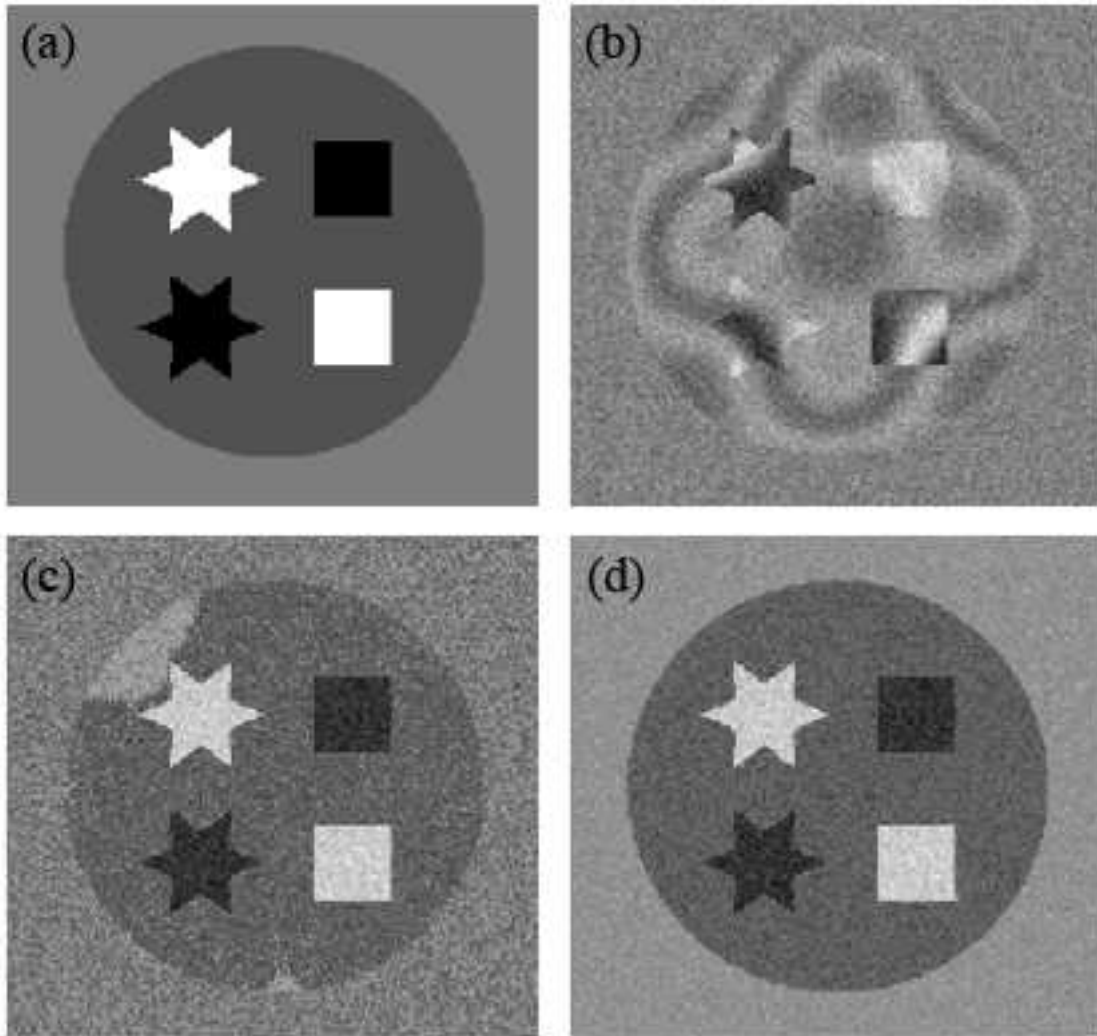


Fig. 12. PSIR result generated with and without using wavelet denoising. (a) Digitally generated phantom image without background phase modulation and noise added to it, (b) Real part of complex image shows the effect of phase modulation and noise, (c) PSIR using region growing algorithm without denoising shows two failure sites which appear in different shade due to wrongly assigned polarity, (d) Phase sensitive reconstruction after wavelet denoising.

The basic idea of slope filtering is based on the fact that in a small area of an IR image, the slope of the pixels remains approximately constant. This is because in a small area of an IR image, the slow varying background phase remains almost constant. The only ambiguity lies in the polarity or the intrinsic phase which is either 0 or π . In both these cases, the slope remains the same. This concept is illustrated in figure 13.

The algorithm starts from the center of the image and expands towards the edges following the trajectory defined in fig. 8. For every considered pixel, the phase-slope is calculated in an appropriately sized window surrounding the pixel. The window size is dependent on the the rate of background phase variation. Window sizes from 5×5 to 10×10 are found to give good results. For finding the phase-slope, a least-squares routine is used to fit a line passing through the complex pixel values in the considered window. As indicated in fig. 13, the line is constrained to pass through the origin. The least-squares line fitting formula is derived as follows:

A line passing through the origin can be expressed as

$$y = bx$$

where b is the slope of the line. We wish to fit a line $y = bx$ through the points (x_1, y_1) through (x_n, y_n) in the complex plane. For least-square line fitting, we minimize the vertical error between the line and the data points. The summation of square of the vertical errors is given by

$$E = \sum_{i=1}^n (y_i - bx_i)^2$$

where b is the slope of the line.

$$\frac{\partial E}{\partial b} = \frac{\partial}{\partial b} \sum_{i=1}^n (y_i - bx_i)^2 = 0$$

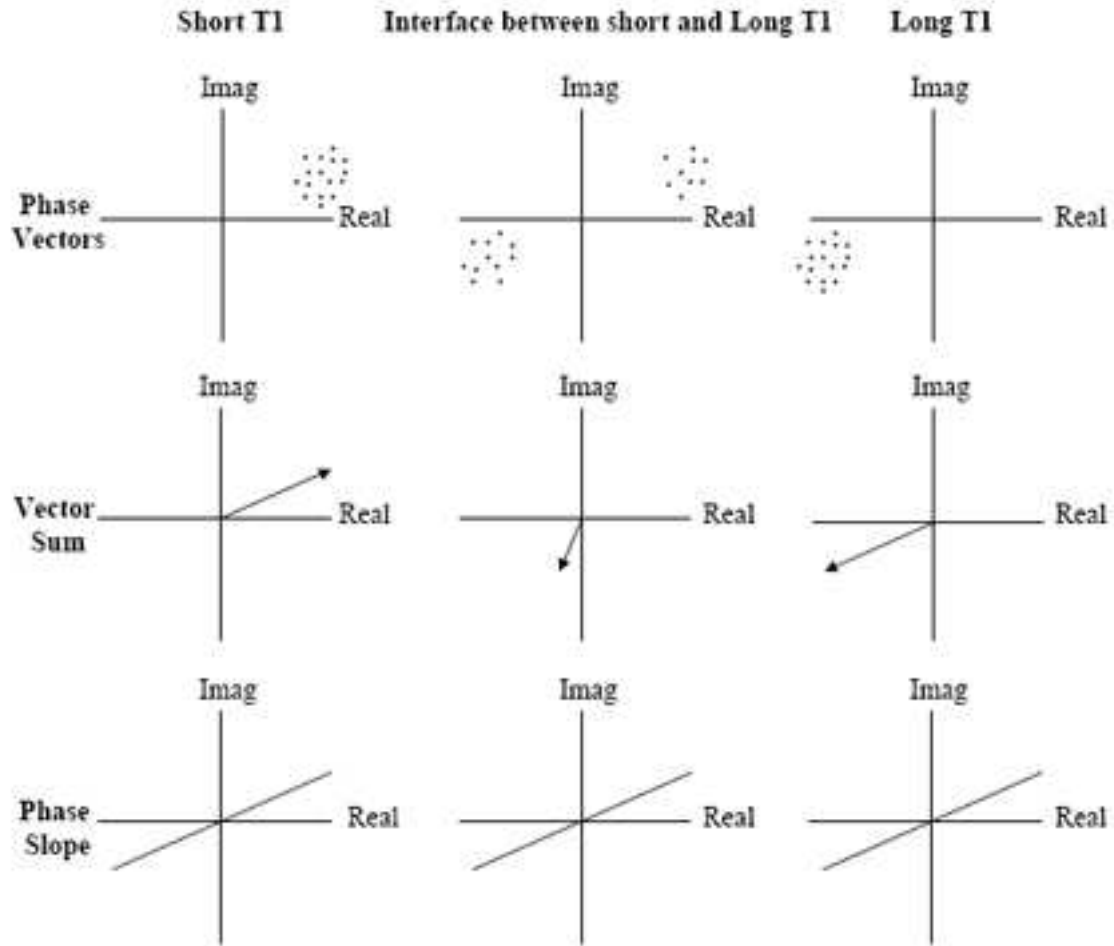


Fig. 13. Diagrammatic representation of phase-slope in a small area of a complex IR image. (a) Portion of tissue with short T1 and hence positive polarity, (b) Portion of area between tissues with short and long T1 values contains, (c) Tissue with long T1 and hence negative polarity. Unlike the vector sum is unpredictable at the interface due to cancelation of opposing phases, the phase-slope value is consistent in all the cases. Source: [15].

$$\begin{aligned} \Rightarrow 2 \sum_{i=1}^n (x_i y_i - b x_i^2) &= 0 \\ \Rightarrow b &= \frac{\sum_{i=1}^n x_i y_i}{\sum_{i=1}^n x_i^2} \end{aligned}$$

Once the slope is determined, the arctangent of the slope gives inclination angle of the line. Since the arctangent values lie between -90^0 to 90^0 , the 180^0 difference between pixels of opposite polarity is lost [15]. Hence, if the line representing the phase-slope is converted to a vector, there is an ambiguity regarding its direction. Here, choosing the direction closest to the vector under consideration retrieves the correct direction and hence the embedded polarity information. We shall refer the resulting vector as the *phase-slope vector*. By replacing the vector value at the pixel under consideration by its projection on the phase-slope vector, random noise variations in the image phase can be directly removed. Figure 14 demonstrates this process graphically.

Slope filtering has been found to be very effective in phase denoising. Improvement using slope filtering is demonstrated using simulation results in the results section.

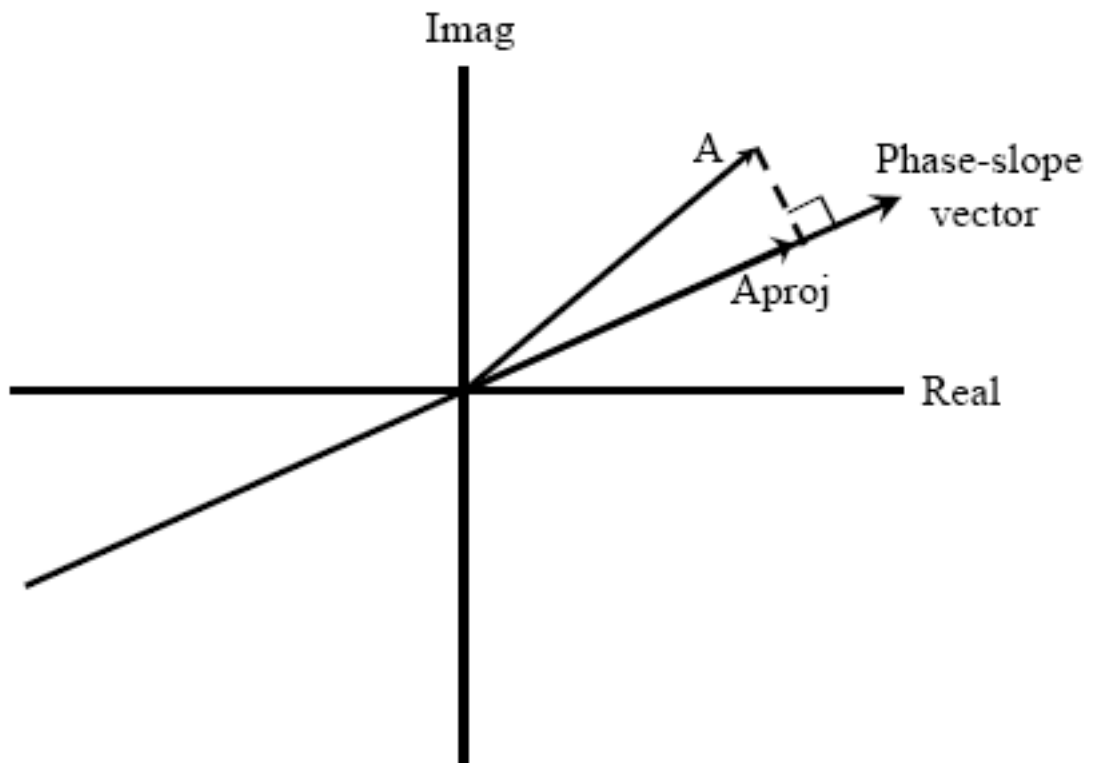


Fig. 14. Slope filtering. Here the vector A is replaced by its projection A_{proj} on the phase-slope vector. The result is a form of averaging on the phase to minimize the effect of noise without disturbing the polarity information.

CHAPTER III

EXPERIMENTAL RESULTS

A. Method of Performance Evaluation

The proposed methods have been tested using computer simulations as well as *in vivo* experiments. The performance of the PSIR methods presented here has been characterized with respect to

- SNR
- Background phase variation rates

For evaluating the performance with respect to SNR, the background phase variation is kept constant and the error in reconstruction is measured at different input image SNRs. The ratio of average power of pixels in the area of interest to that of pixels in the noise area is used for calculating SNR. Mathematically, the definition of image SNR used here can be expressed as

$$SNR = 10 \log \frac{\frac{1}{N_s} \sum_{(x,y) \in SignalRegion} |I(x,y)|^2}{\frac{1}{N_n} \sum_{(x,y) \in NoiseRegion} |I(x,y)|^2} \quad (3.1)$$

where N_s is the number of pixels in the area of interest or the signal region and N_n is the number of pixels in the noise region.

Since the goal of a successful reconstruction is to successfully retrieve the polarity information of the imaged object, the reconstruction error is defined as the percentage of pixels in the area of interest which are reconstructed with incorrect polarities. Mathematically, the reconstruction error e can be expressed as

$$e = \frac{1}{N_s} N_E \{ I_{PSIR}(x,y) \mid \text{sign}(I_{PSIR}(x,y)) \neq \text{sign}(I_{True}(x,y)) \} \times 100\% \quad (3.2)$$

where $N_E\{\cdot\}$ denotes the number of elements in a set and N_s is the total number of elements in the area of interest.

The error vs. SNR graphs for each method describe its performance with respect to noise. Similarly, the performance of the methods is evaluated with respect to the rate of background phase variations. Here, the spatial variation rate of background phase modulation is increased keeping the SNR constant.

B. Computer Simulations

1. IR Phantom

In order to characterize the performance of the proposed algorithm, a digital phantom image with characteristics similar to the human brain IR images was designed. The digital phantom was designed with the following goals in mind

1. Simple structures that can be well discerned in the presence of reconstruction abnormalities and noise thus allowing any abnormalities in reconstruction to be quickly identified
2. Structures with different T_1 values such that there are parts with positive as well as negative polarities in the image
3. Control over the amount of noise added to the image so as to control the image SNR
4. Control over the pattern, rate of variation and orientation of the background phase modulation

Figure 15 shows the flow-chart of IR phantom generation where the phantom template is taken and is converted to a complex IR image with background phase

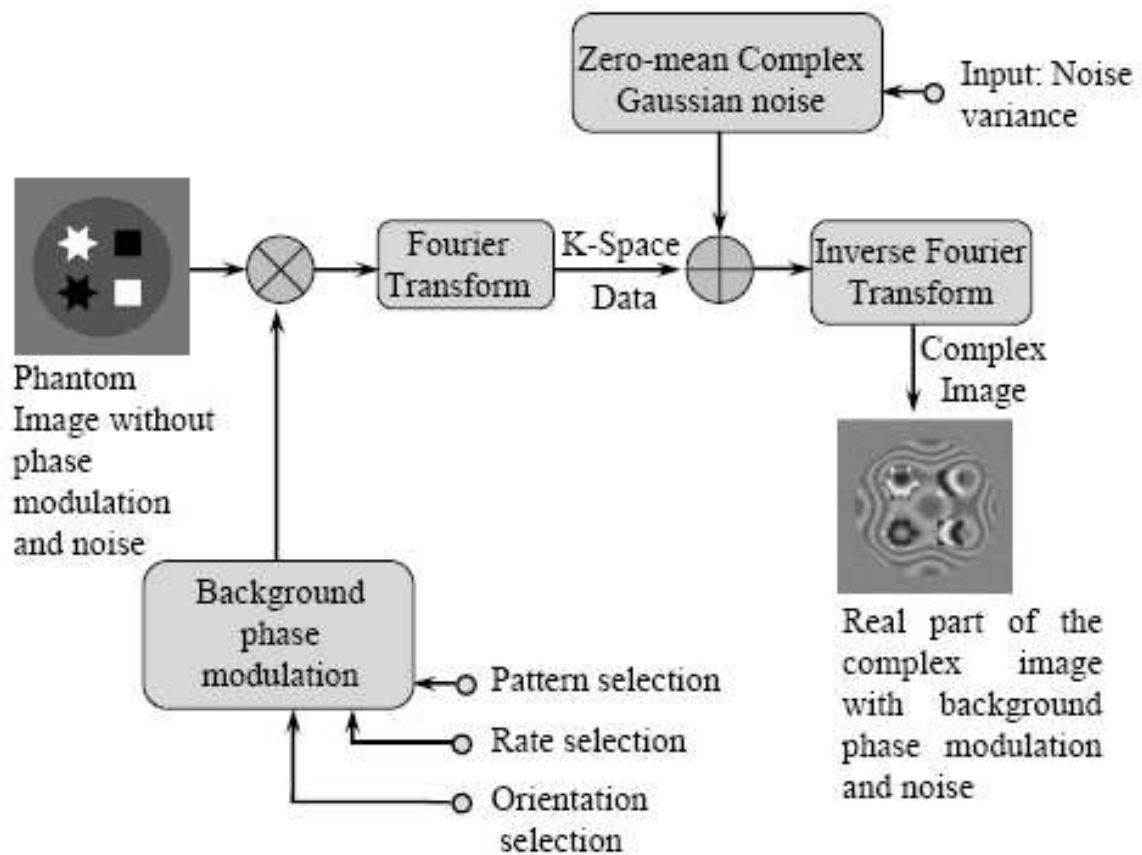


Fig. 15. Flow chart of complex IR phantom generation. The bubbled arrows indicate the user controllable inputs.

variation and noise. The phantom generation program allows generation of a variety of background phase modulation patterns. Independently controllable variations in horizontal and vertical directions are used for generating phase modulation patterns. Linear, sinusoidal or linear+sinusoidal variations with different rates can be selected for both horizontal as well as vertical directions. The combined effect can be as simple as single frequency diagonal phase variation to complex multi-spatial-frequency pattern with different rates of variations in different image areas. The orientation selection allows the background phase pattern to be rotated and the desired angle before superimposing it on the phantom image template. This allows user to determine if the algorithm under test has any directional preference.

MR data is acquired in frequency domain, called the *k-space* domain and is converted to the complex image using an inverse Fourier transform operation. Hence, the noise in an actual MR image is introduced in the k-space domain. In order to simulate realistic noise addition, we first convert the phantom image to k-space domain, add zero mean complex Gaussian noise and then convert it back to the complex domain. Figure 16 shows the phantom template, the background phase modulation pattern, the magnitude and the real images. The effect of background phase modulation can be seen in the real part of the complex image. Note that while the magnitude image does not suffer from the effects of background phase modulation, it fails to show contrast between objects of similar magnitude and opposite polarity.

2. Block Merging

The block merging algorithm is ideal for performing reconstruction of noisy images having large structures with same polarities and moderate background phase variation rates. Since the algorithm adaptively chooses optimum averaging depths depending on the phase variation rates, it is better able to combat noise in images with slow

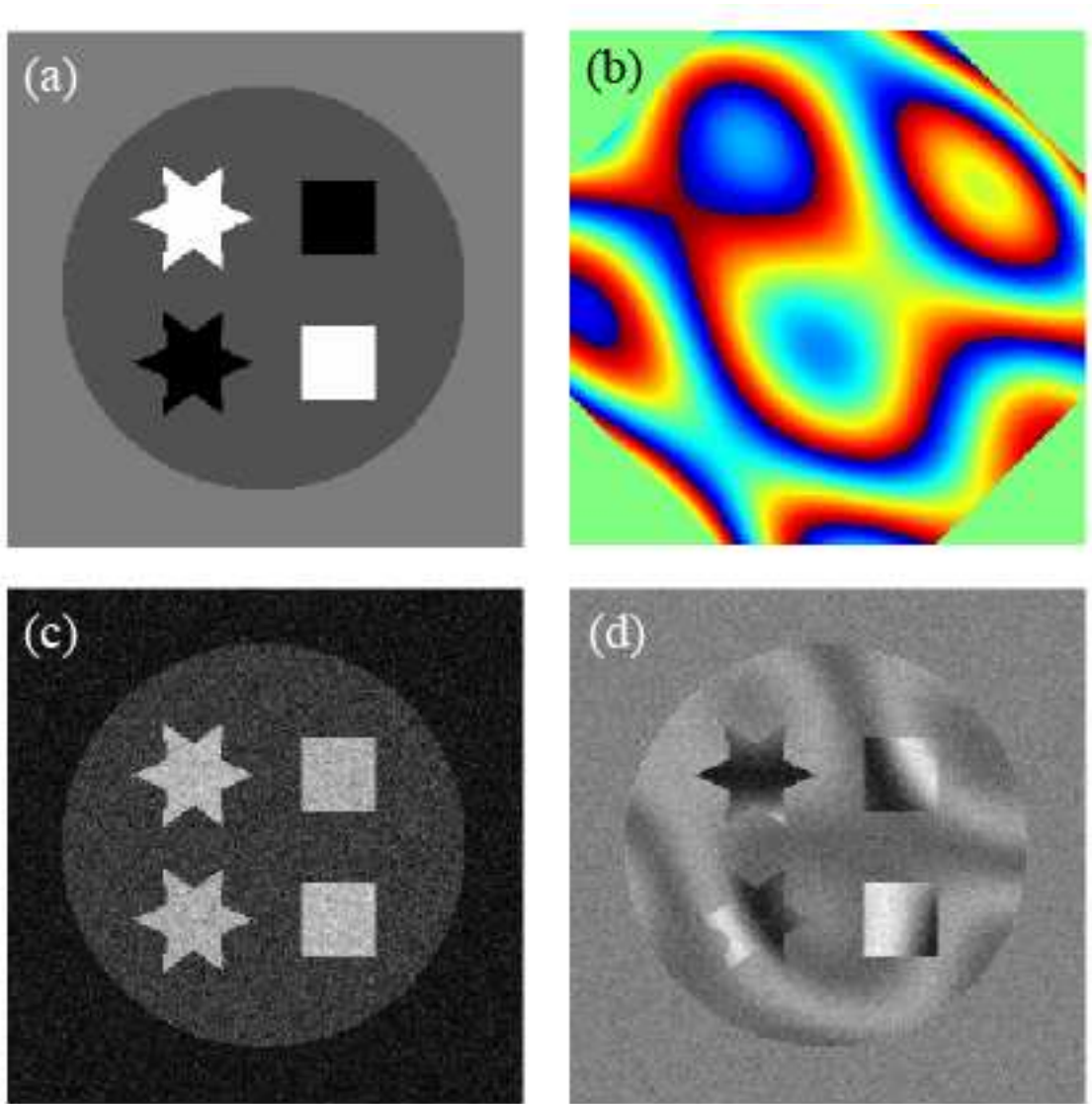


Fig. 16. Phantom image. (a) Phantom template without background phase modulation and noise, (b) Background phase modulation pattern. The pattern is cropped at the corners due to rotation by 45° , (c) Magnitude image. Notice that the star and the square with different polarity appear in the same shade in this image due to similar magnitude, (d) Real part of complex phantom image displays the effect of background phase modulation.

background phase variation rates. Figure 17 shows successful reconstruction in an image with moderate background phase variation rate and low SNR. Here the image SNR is 27 dB and the reconstruction error is 0.26%

Figure 18 shows the plot to error vs. SNR plot for the block merging algorithm. As seen from the plot, the amount of error increases gradually with the decrease in SNR which indicates that the PSIR algorithm does not suffer from an avalanche breakdown. Also the error rate becomes negligible above 27 dB SNR. The actual IR images in our database have an average SNR above 40 dB. Hence, the error vs. SNR performance of the algorithm is satisfactory.

Block merging algorithm can also reconstruct high SNR images with rapid background phase variations. Figure 19 shows successful reconstruction of a phantom image with very high background phase variation rate. IR images obtained in practice typically have about one to three cycles of background phase variation covering the field-of-view. The phantom image showing in the fig. 19 has a little more than eleven complete cycles of background phase variation covering the field-of-view. Thus the proposed algorithm quite over-performs in the area of handling rapid phase modulations on IR images. In fig. 19, the a regular background phase pattern is shown. In more complicated patterns, the phase variation rate may be different in different areas of the image. In such cases, the maximum variation rate is used as the parameter for evaluation.

3. Region Growing

The region growing algorithm is efficient in handling noise under high background phase variation rates. In these images, the block merging algorithm chooses lower averaging depths due to high phase variations and hence is not able to minimize noise effects. Figure 20 shows successful reconstruction in an image with high background

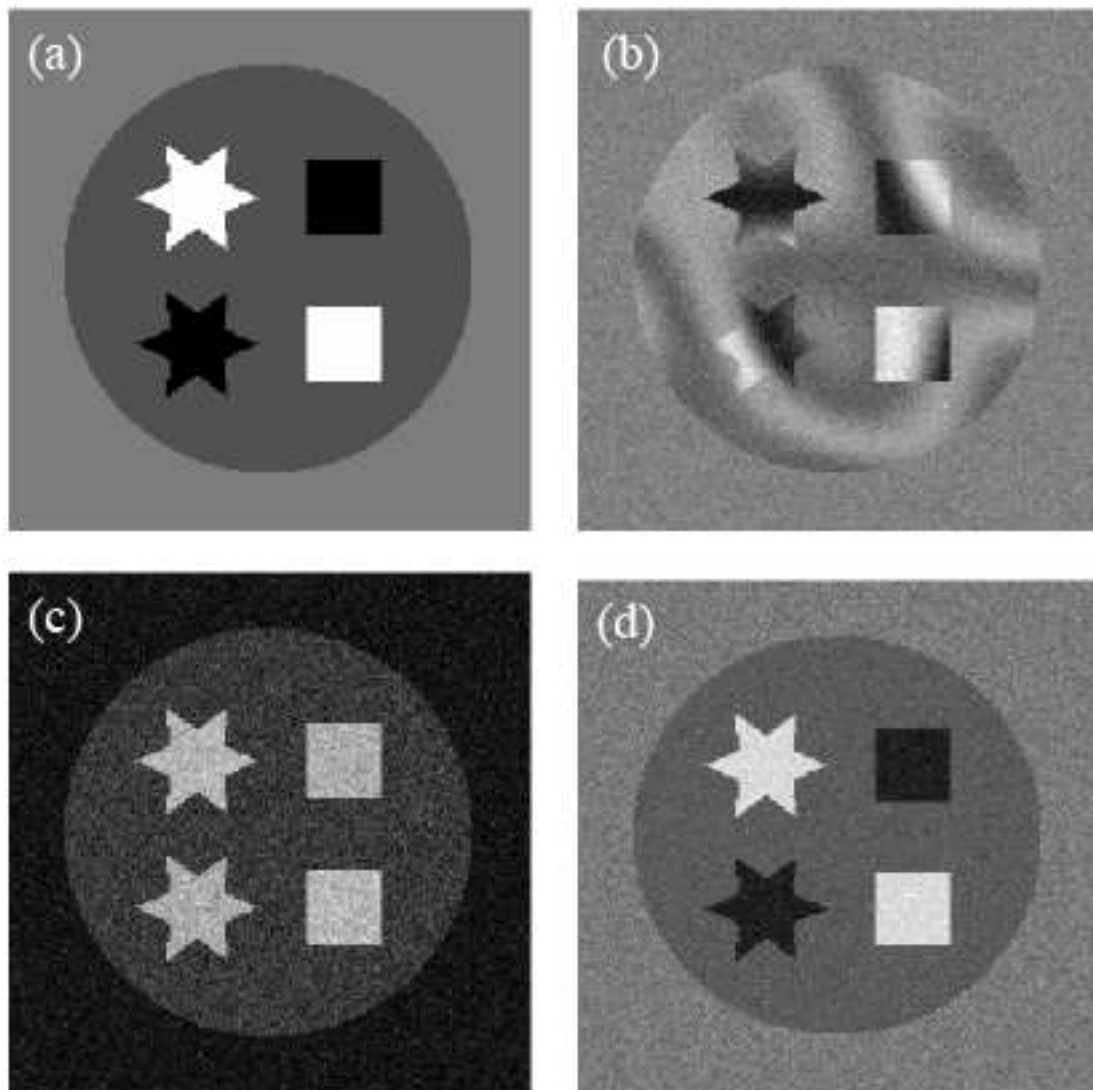


Fig. 17. Image reconstruction using block merging algorithm. (a) True image, (b) Real image displaying background phase modulation, (c) Magnitude reconstruction, (d) PSIR image obtained using block merging algorithm.

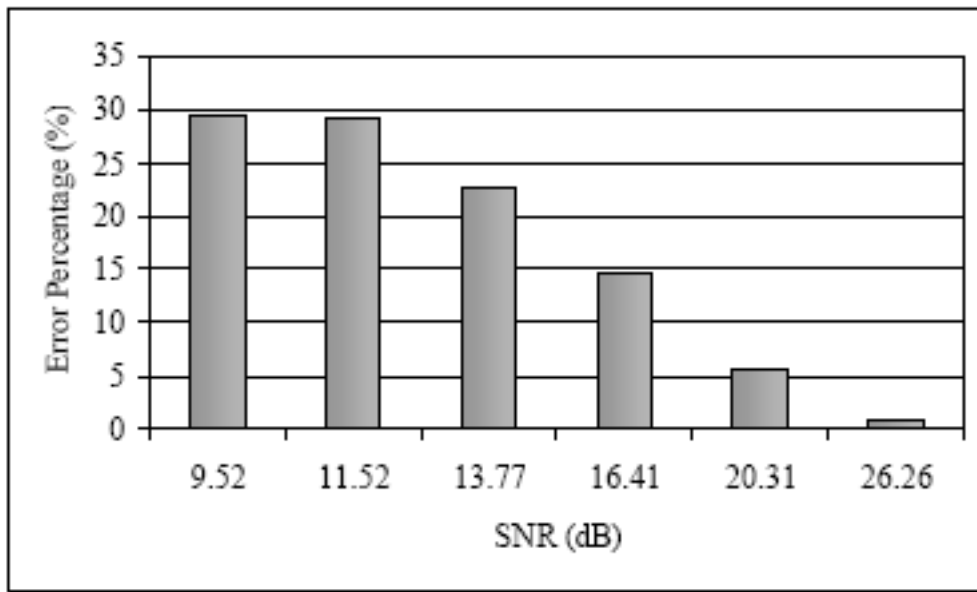


Fig. 18. Error vs. SNR plot for the block merging algorithm. The background phase variation in all the cases was maintained constant with maximum variation rate of 0.026 cycles per pixel.

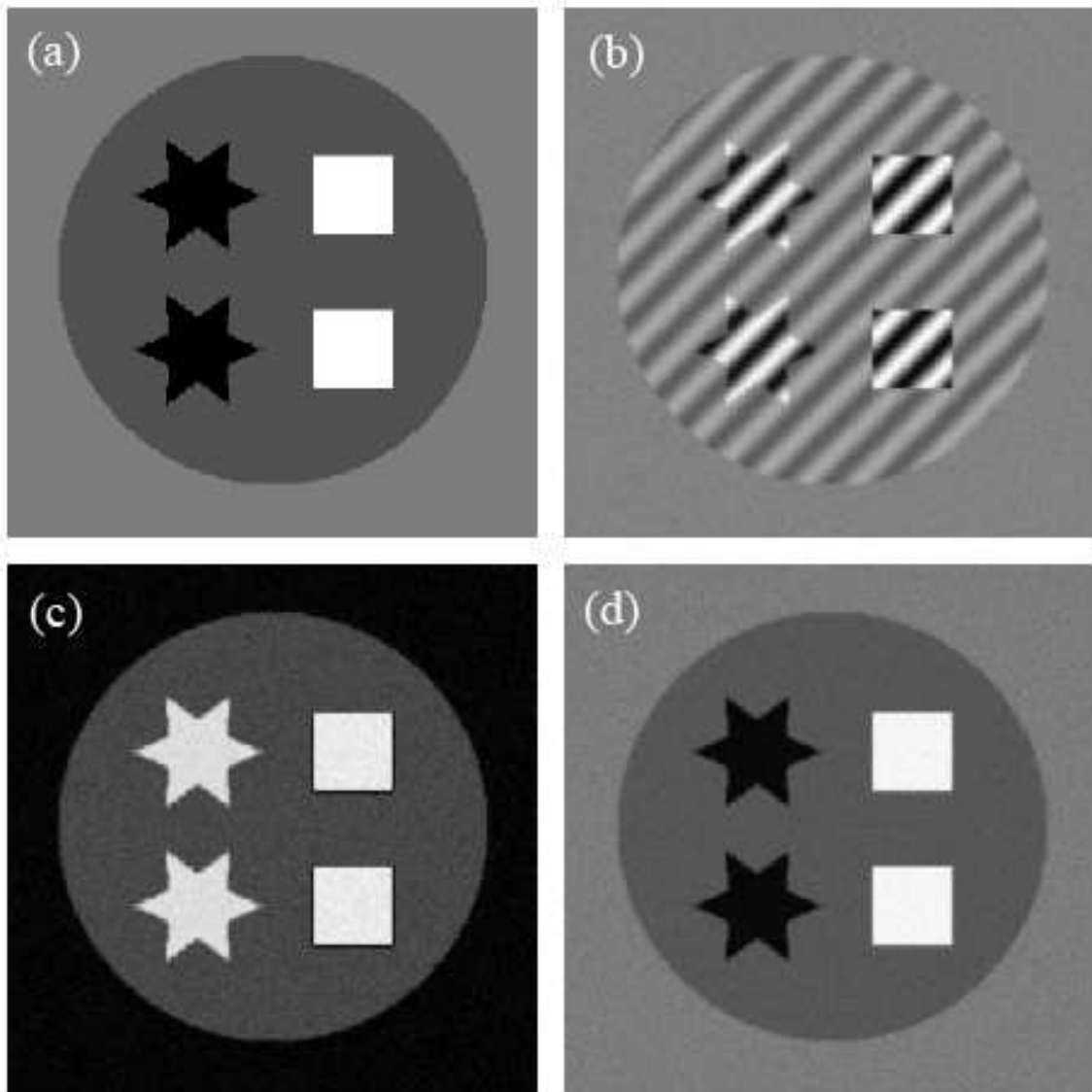


Fig. 19. Phase sensitive reconstruction of image with very high background phase variation rate using block merging algorithm. (a) True image, (b) Real image displaying rapid background phase variations, (c) Magnitude reconstruction, (d) PSIR Image obtained using block merging algorithm.

phase variations and low moderately low SNR of 33.4 dB. The white box marks the maximum phase variation regions where background phase goes through two complete phase cycles in just 28 pixels ie. variation rate of 0.07 cycles per pixel.

Figure 21 shows the plot to error vs. SNR plot for the block merging algorithm. The plot indicates that the reconstruction errors increase gradually with SNR and hence, the region growing algorithm does not have an avalanche breakdown problem.

Figure 22 shows the plot of error vs. variation rate of background phase modulation.

4. Wavelet Denoising

For the PSIR algorithms proposed in this research, the ability of withstanding rapid background phase variations is found to more in case of high SNR images. Moreover, by increasing the image SNR of the image input to the PSIR algorithm, the overall capability of handling noise increases. This motivates the use of wavelet denoising proposed in [25]. The idea is validated by the error vs. input image SNR plot shown in fig. 23. As indicated by the plots, the percentage error is significantly reduced when PSIR with denoising is carried out. Note that the percentage error with denoising at about 12 dB image SNR is less than error without denoising at 20 dB SNR. This highlights the primary advantage of using the wavelet denoising scheme. Also note that the increase in error with the decrease in image SNR is much lower when denoised phase is used. This pushes the algorithm's breakdown SNR threshold to a much lower value. We define this breakdown SNR as the SNR of the input image at which the PSIR image has 25% reconstruction errors. It can also be observed from Fig.23 that the improvement in error performance using proposed scheme increases with decrease in SNR. Hence the computational power spent on denoising best pays off when the image SNR is low. PSIR algorithms generally fail at two vulnerable

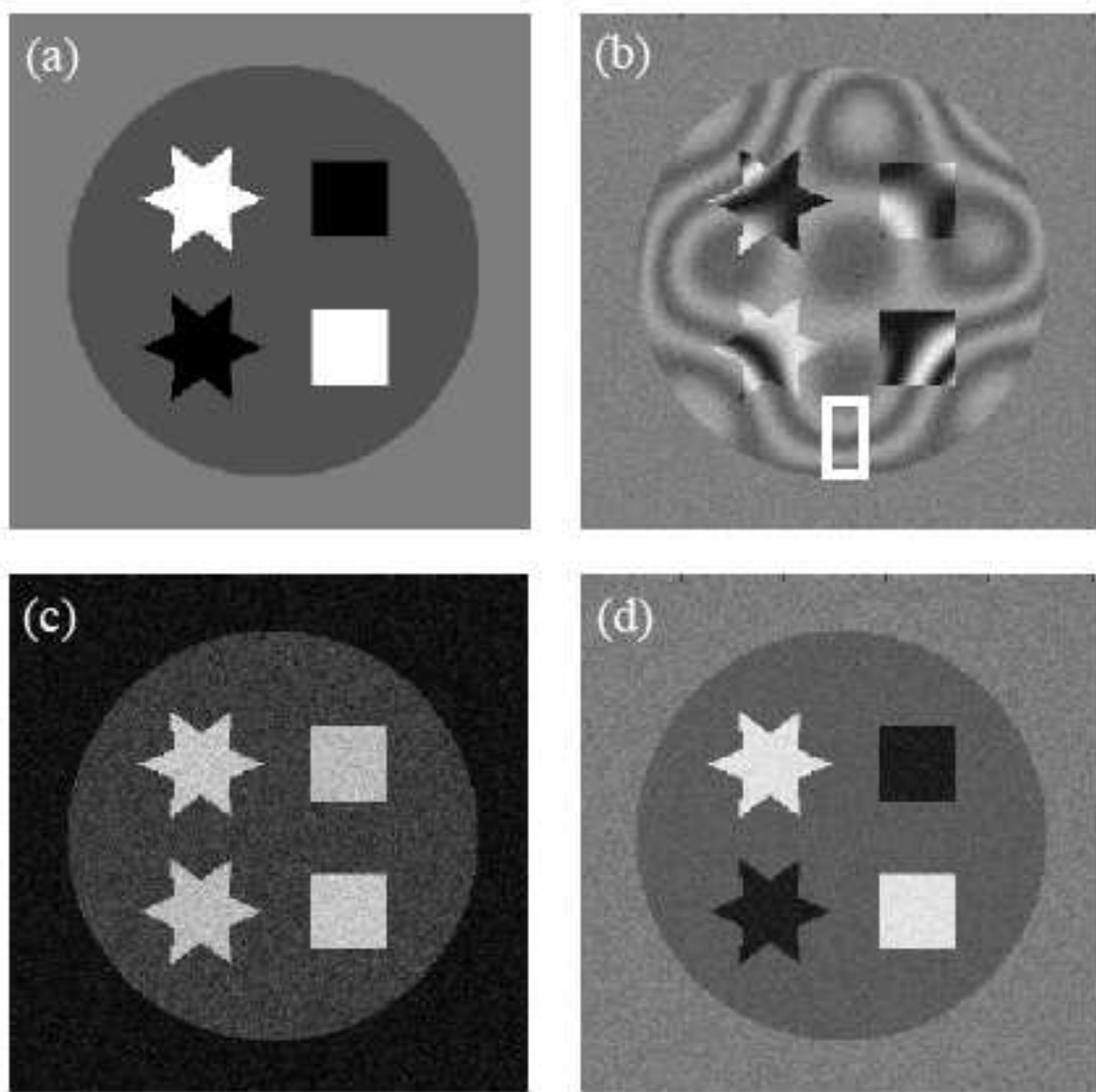


Fig. 20. Image reconstruction of image with high background phase variation rate and moderately low SNR using region growing algorithm. (a) True image, (b) Real image displaying background phase modulation. The white box indicates the maximum phase variation region with 2 phase cycles covered in 28 pixels, (c) Magnitude reconstruction, (d) PSIR image obtained using block merging algorithm.

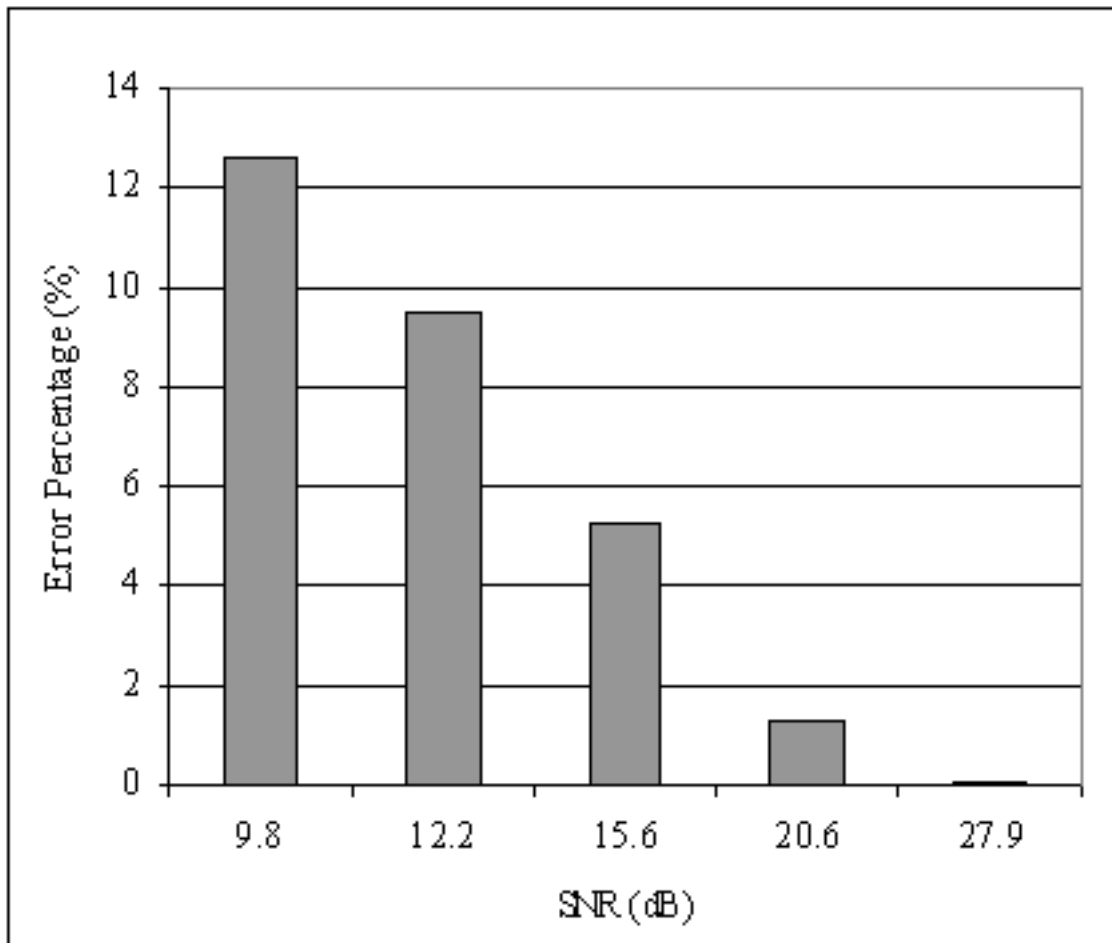


Fig. 21. Error vs. SNR plot for the region growing algorithm. The background phase variation in all the cases was maintained constant with maximum variation rate of 0.026 cycles per pixel.

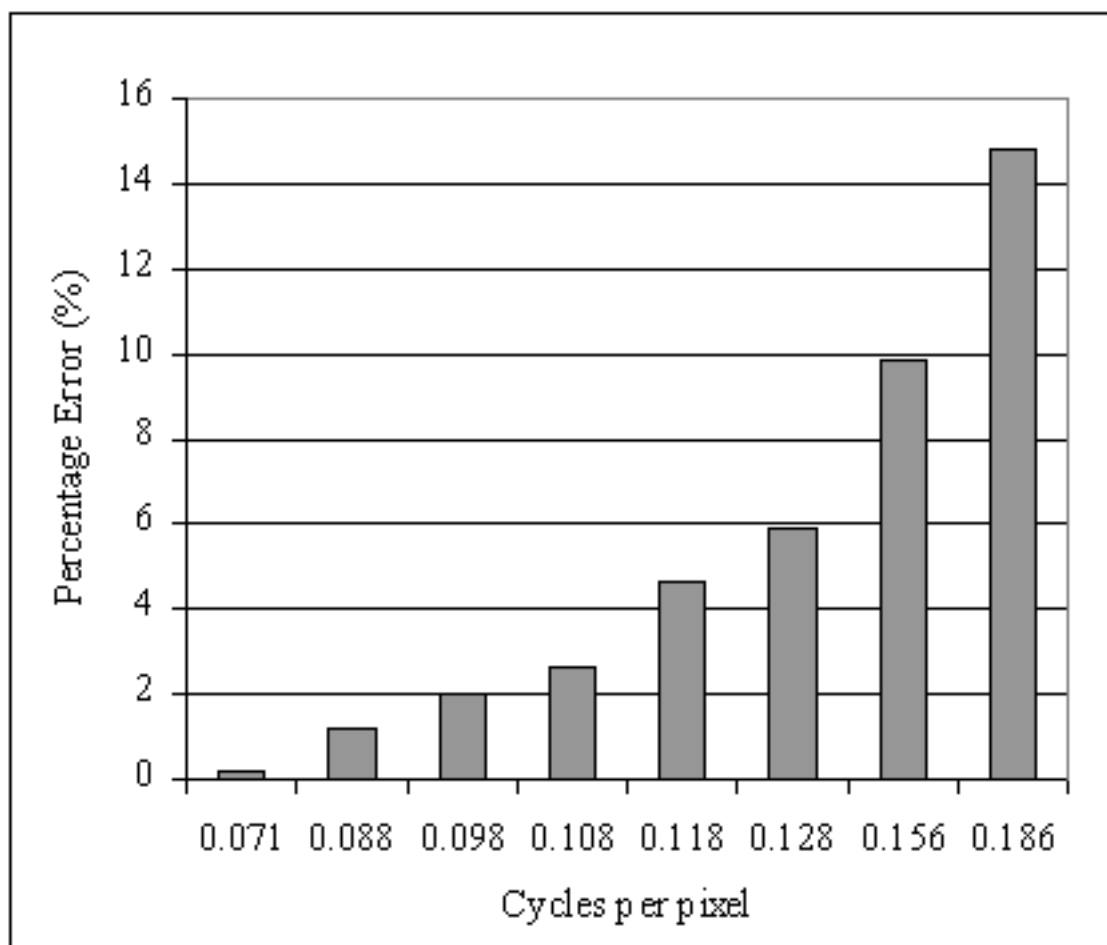


Fig. 22. Error vs. background phase variation rate plot for the region growing algorithm. The image SNR in all the cases was maintained at a constant level of 40 dB.

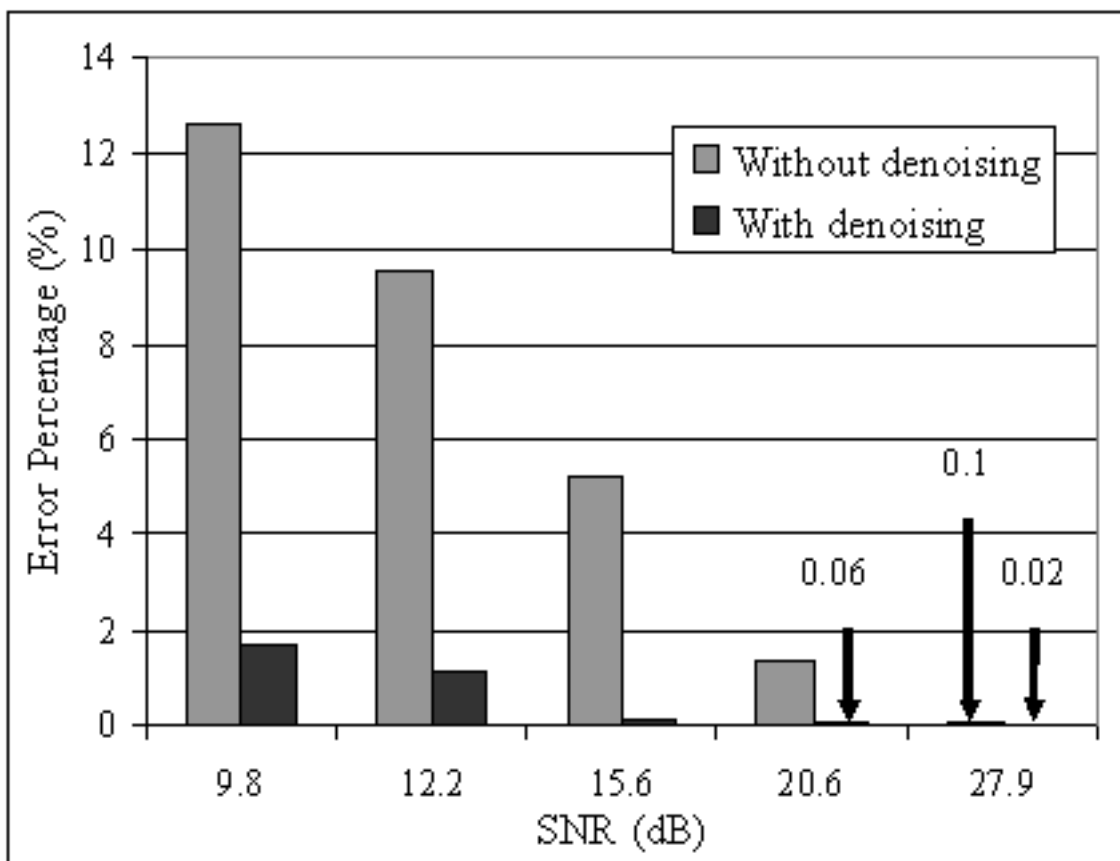


Fig. 23. Comparative error vs. SNR plots for region growing algorithm with and without wavelet denoising. Here the background phase variation rate for each case was set at 0.035 cycles per pixel.

spots: The boundaries between object and space and at small portions of MR image where phase image has low SNR. Thus, the denoising can be applied to only those areas to save the computational power while taking the best advantage of denoising. These areas being marked by high gradient in the magnitude image, can be isolated using an automated algorithm. The approach, however, has not been tested yet.

Figure 24 shows a result set in which region growing algorithm fails without denoising due to high background phase variation rate and moderately low SNR. The failure shown is a characteristic failure found in cases where PSIR fails due to high frequency background phase variations. The failure is non-sporadic and occurs at multiple locations with high frequency variations. The image SNR in this case was 27.8 dB. Here successful reconstruction was performed when input data was wavelet denoised prior to PSIR algorithm. Figure 25 shows the plot of percentage error vs. maximum variation rate of background phase variation.

5. Slope Filtering

Slope filtering is an efficient and direct way of removing random errors in phase. By choosing an appropriate window size according to rate of background phase variations, a remarkable improvement in the performance of the proposed PSIR algorithms can be obtained. Figure 26 shows the improvement in region growing algorithm using slope filtering. Here the IR data has high background phase variation with more than 8 complete phase cycles in the field of view and poor SNR of just 17.9 dB. Successful reconstruction was possible in this case because of slope filtering.

Slope filtering is not computationally intensive and gives an improved reconstruction when it is used with the proposed PSIR algorithms. Hence, in most results showing the *in vivo* experiments, slope filtering has been included as a preceding stage of the PSIR reconstruction.

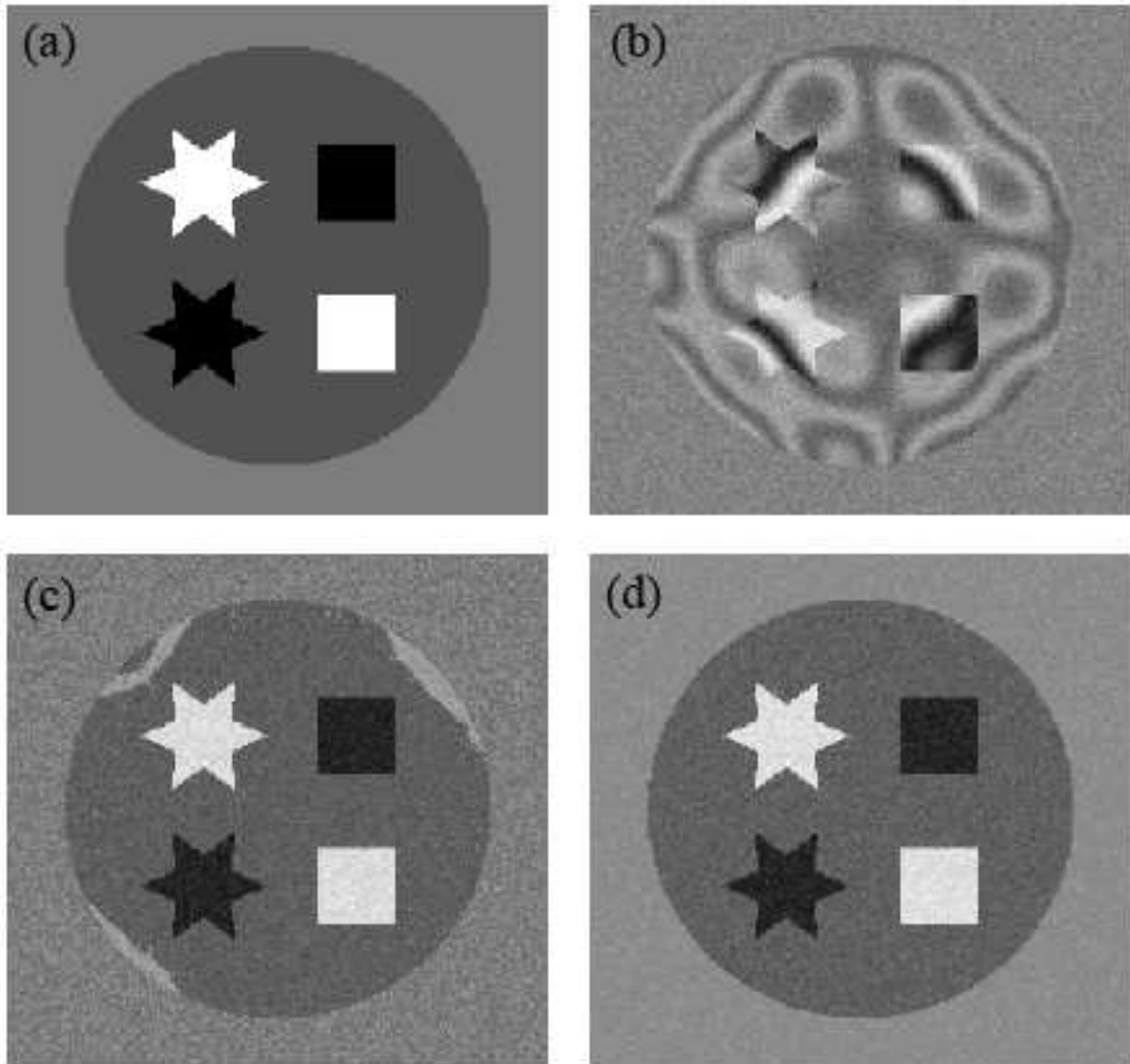


Fig. 24. Comparative PSIR result sets generated with and without using denoising for high rate of background phase variations. (a) Phantom image without phase modulation and noise; (b) Real part of complex image shows different phase variation rates at different locations; (c) PSIR using region growing without denoising shows failure due to high frequency background phase; (d) PSIR after denoising the phase image.

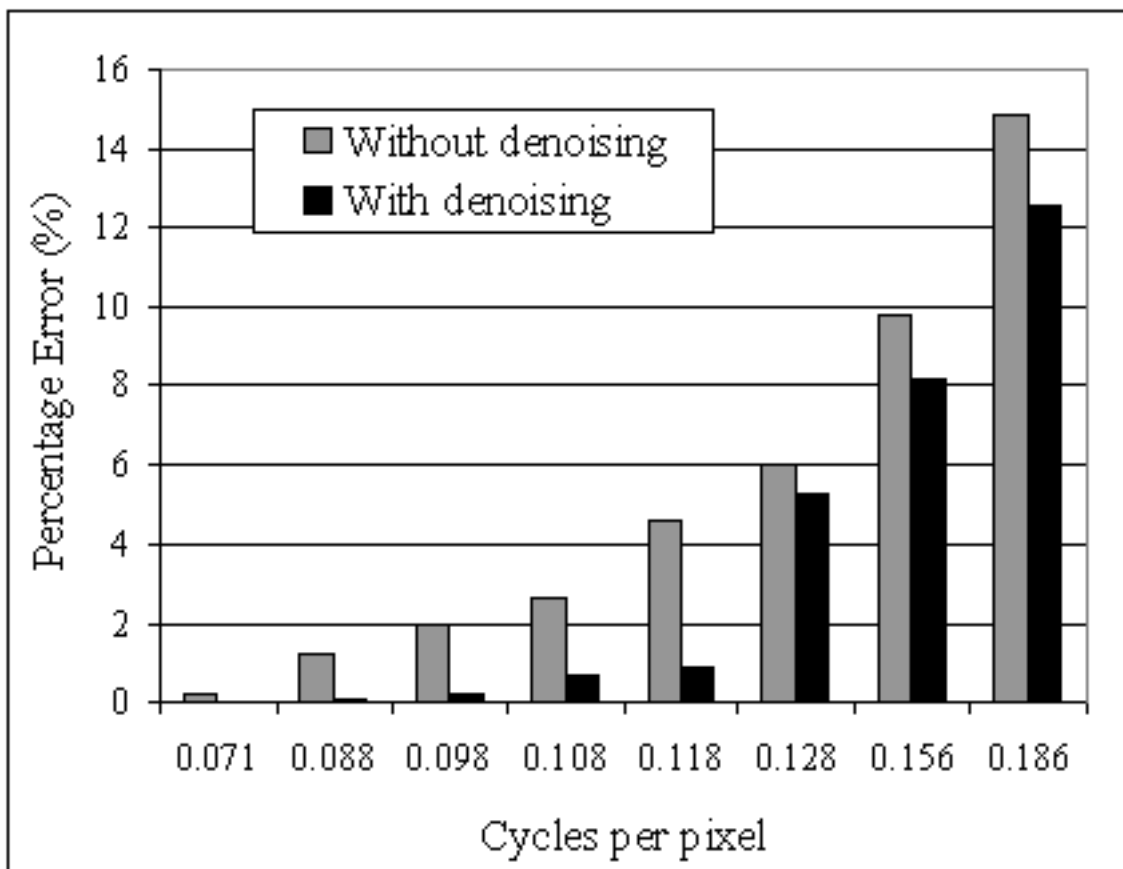


Fig. 25. Plot of percentage error vs. maximum spatial variation measured in cycles per pixel. Errors increase with frequency of background phase variations. Image SNR of 27.5 dB was used for simulations.

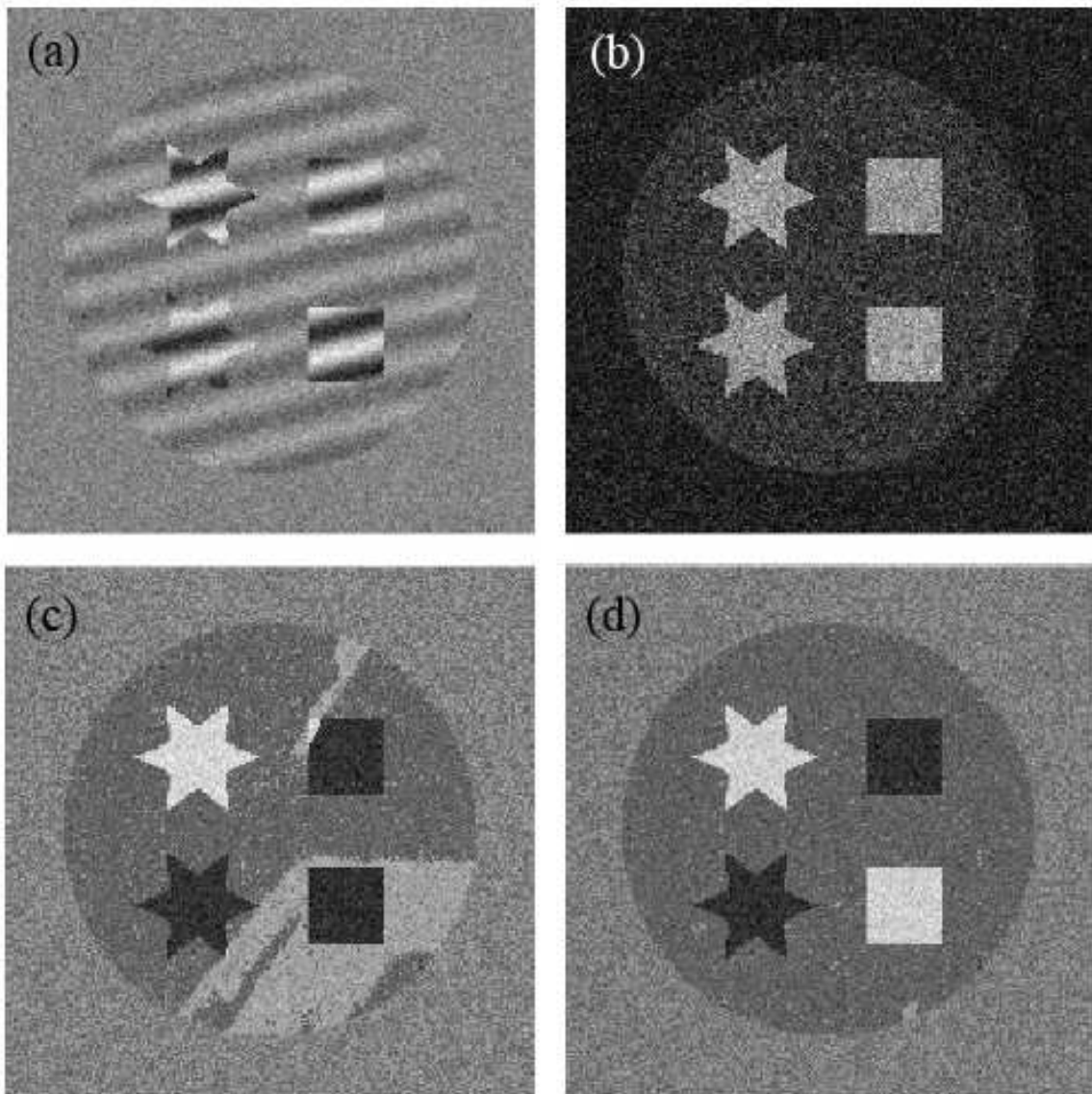


Fig. 26. Improvement in region growing algorithm using slope filtering. Here background phase variation rate is 0.065 cycles per pixel and the image SNR is 17.9 dB. (a) Phantom image without phase modulation and noise; (b) Real part of complex image; (c) PSIR using region growing without slope filtering; (d) PSIR with slope filtering.

C. *In vivo* Results

The proposed algorithms have been tested on a variety of MR images acquired using *in vivo* experiments. The tests were done on a number of data sets acquired using different MR scanners with different magnet strengths. This section presents the results of some of these tests.

Figures 27 to 30 show the phase sensitive reconstruction of inversion recovery brain images. Figures 27 and 28 were reconstructed using block merging method whereas figures 29 and 30 were reconstructed using the region growing algorithm. The images are slices of a single brain taken at various depths. The inversion recovery data set was collected using a fast spin-echo pulse sequence. The imaging parameters used in collecting the data sets were TR/TE/TI/ETL= 4000/17/450/16ms.

Figure 31 demonstrates the utility of slope filtering algorithm. At the boundary of the object of interest, the PSIR algorithm fails due to random noise in the phase image. Here successful reconstruction could be carried out when the input image was treated with slope filter before the PSIR reconstruction.

Figures 32 to 34 show results of tests done data sets acquired using a 15 Tesla MR scanner. Here the data was acquired using a fast spin-echo imaging sequence.

The algorithms were also tested on data acquired using multiple coils. Figures 35 to 37 show results of tests done on 8 coil data. This is an example of successful reconstruction of low SNR *in vivo* data.

Figure 38 demonstrates reconstruction of data with high rate of phase variation.

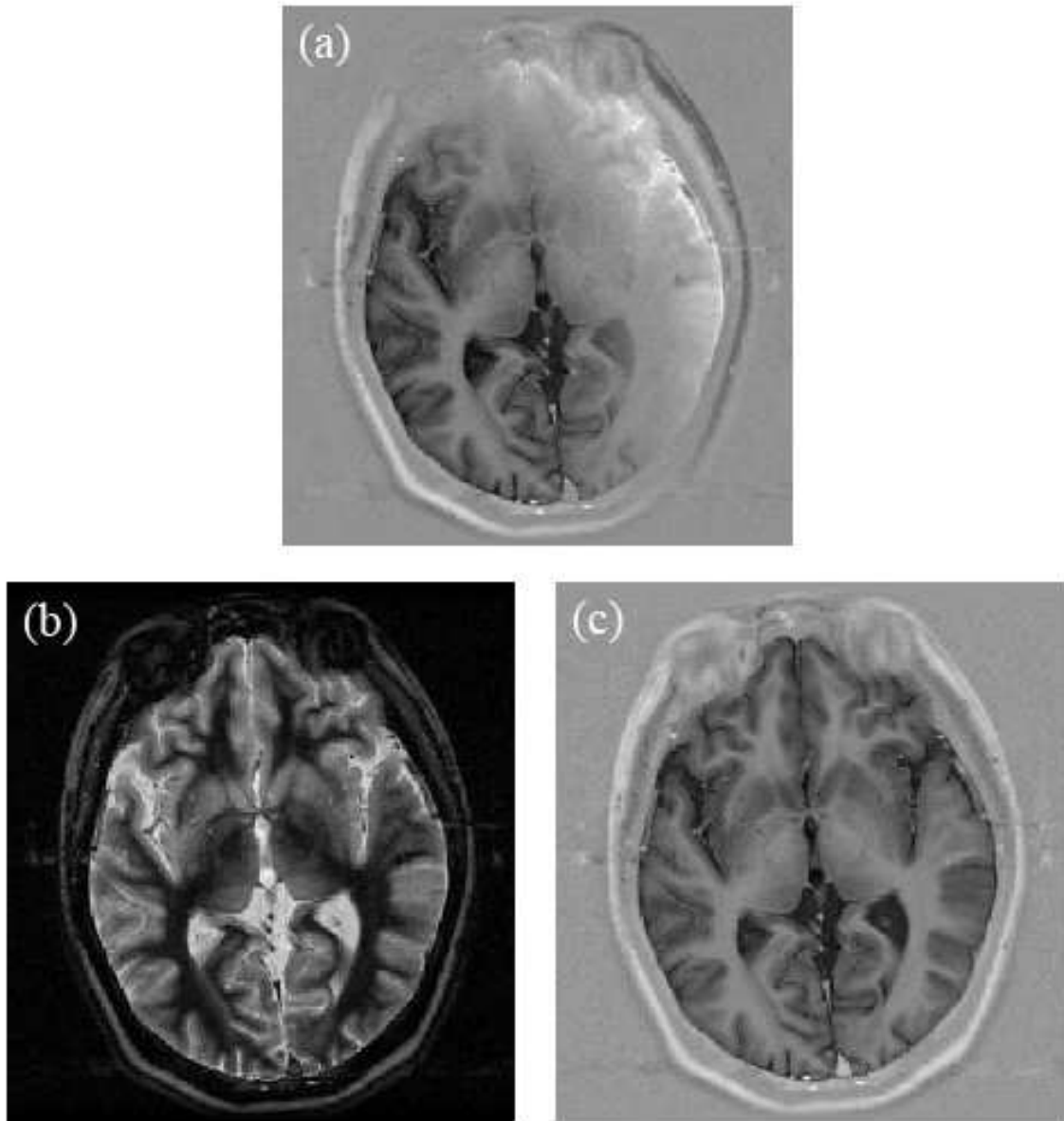


Fig. 27. Phase sensitive reconstruction of IR brain image using block merging algorithm (a) Real part of complex IR image; (b) Magnitude reconstruction; (c) PSIR image.

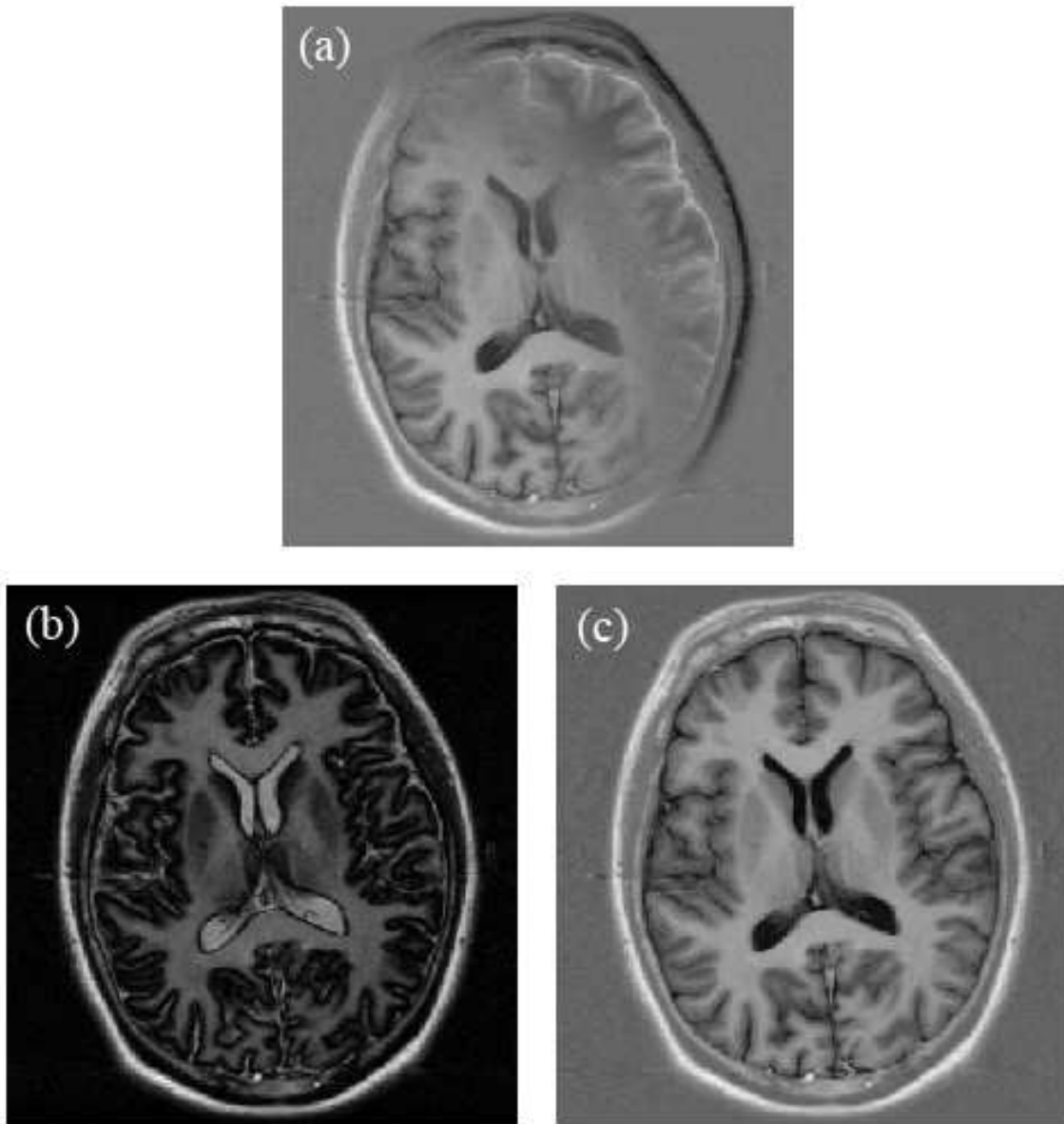


Fig. 28. Phase sensitive reconstruction of IR brain image using block merging algorithm (a) Real part of complex IR image; (b) Magnitude reconstruction; (c) PSIR image.

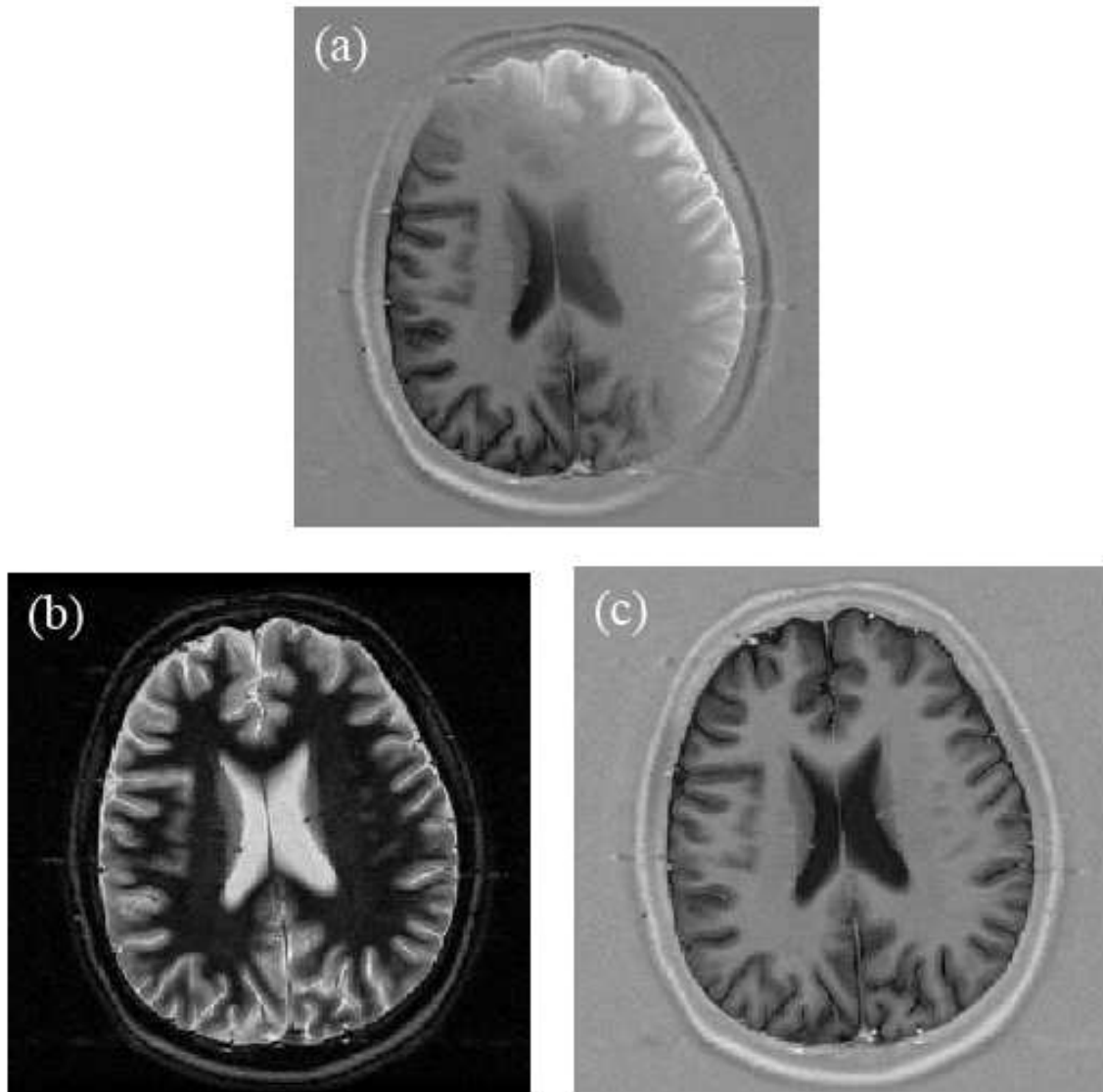


Fig. 29. Phase sensitive reconstruction of IR brain image using region growing algorithm (a) Real part of complex IR image; (b) Magnitude reconstruction; (c) PSIR image.

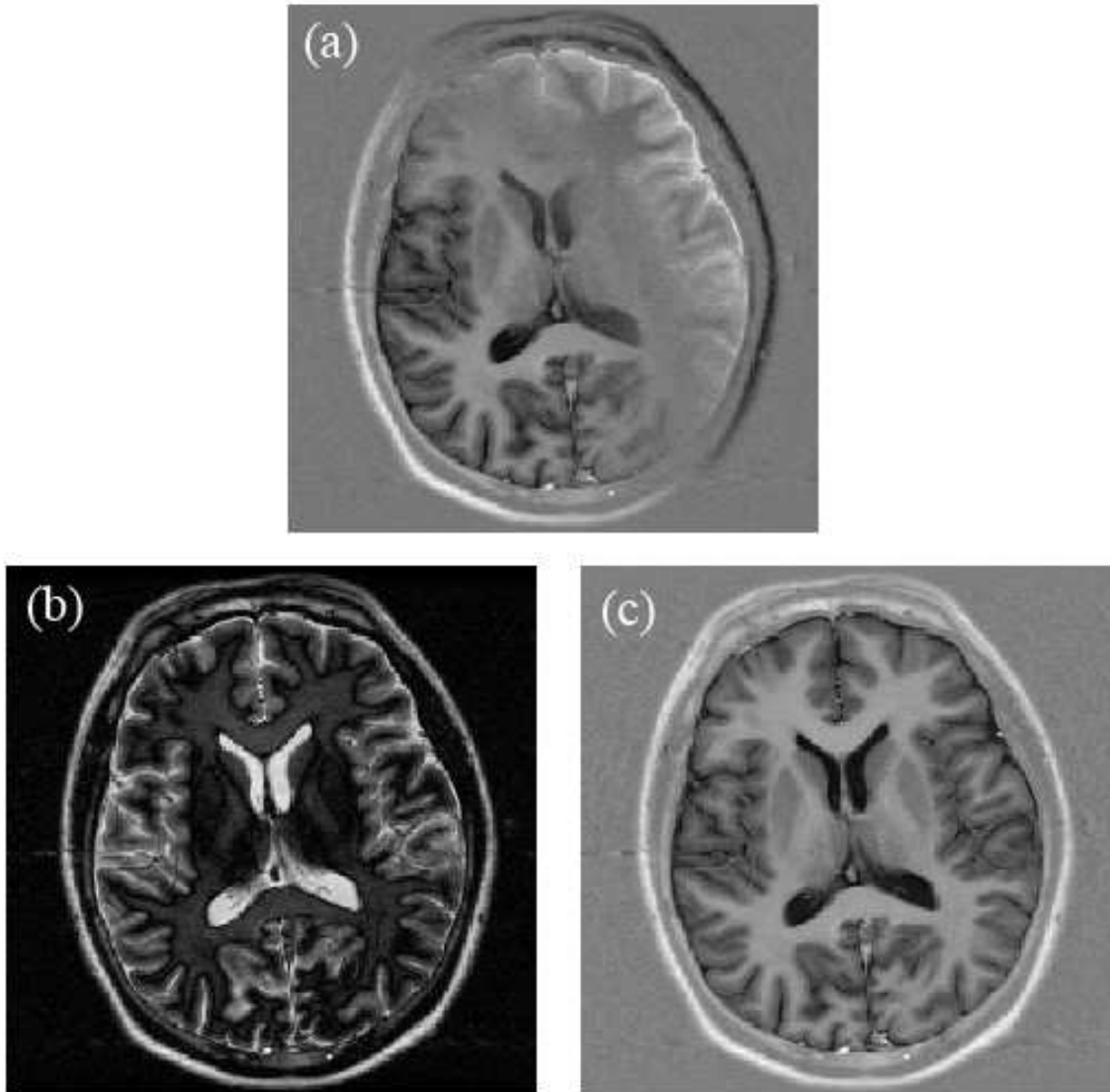


Fig. 30. Phase sensitive reconstruction of IR brain image using region growing algorithm (a) Real part of complex IR image; (b) Magnitude reconstruction; (c) PSIR image.

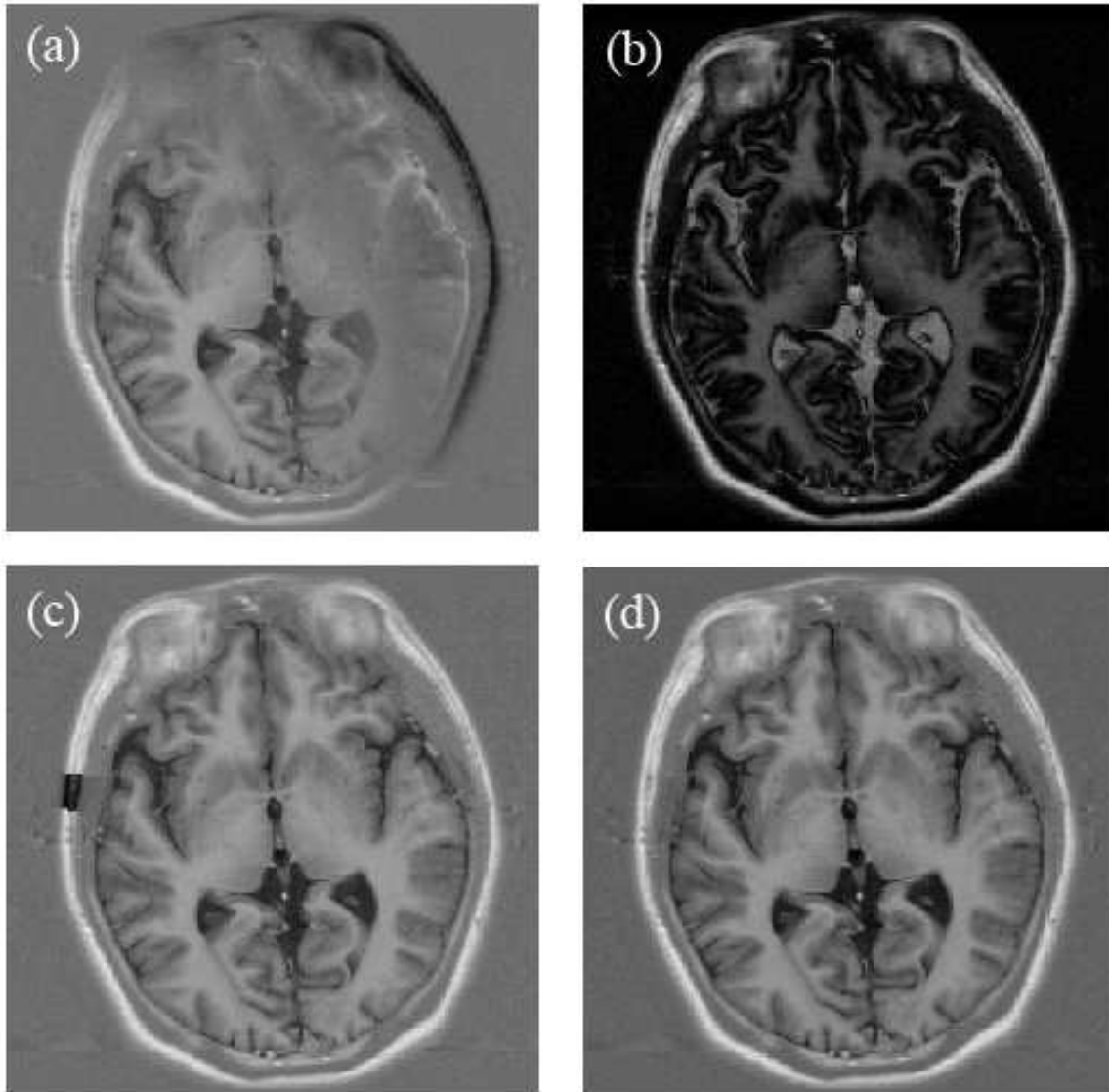


Fig. 31. Use of slope filter to achieve successful reconstruction. (a) Real part of complex IR image; (b) Magnitude reconstruction; (c) Phase sensitive reconstruction fails in a part of image due to noise; (d) Successful phase sensitive reconstruction by treating the image data with slope filter before reconstruction.

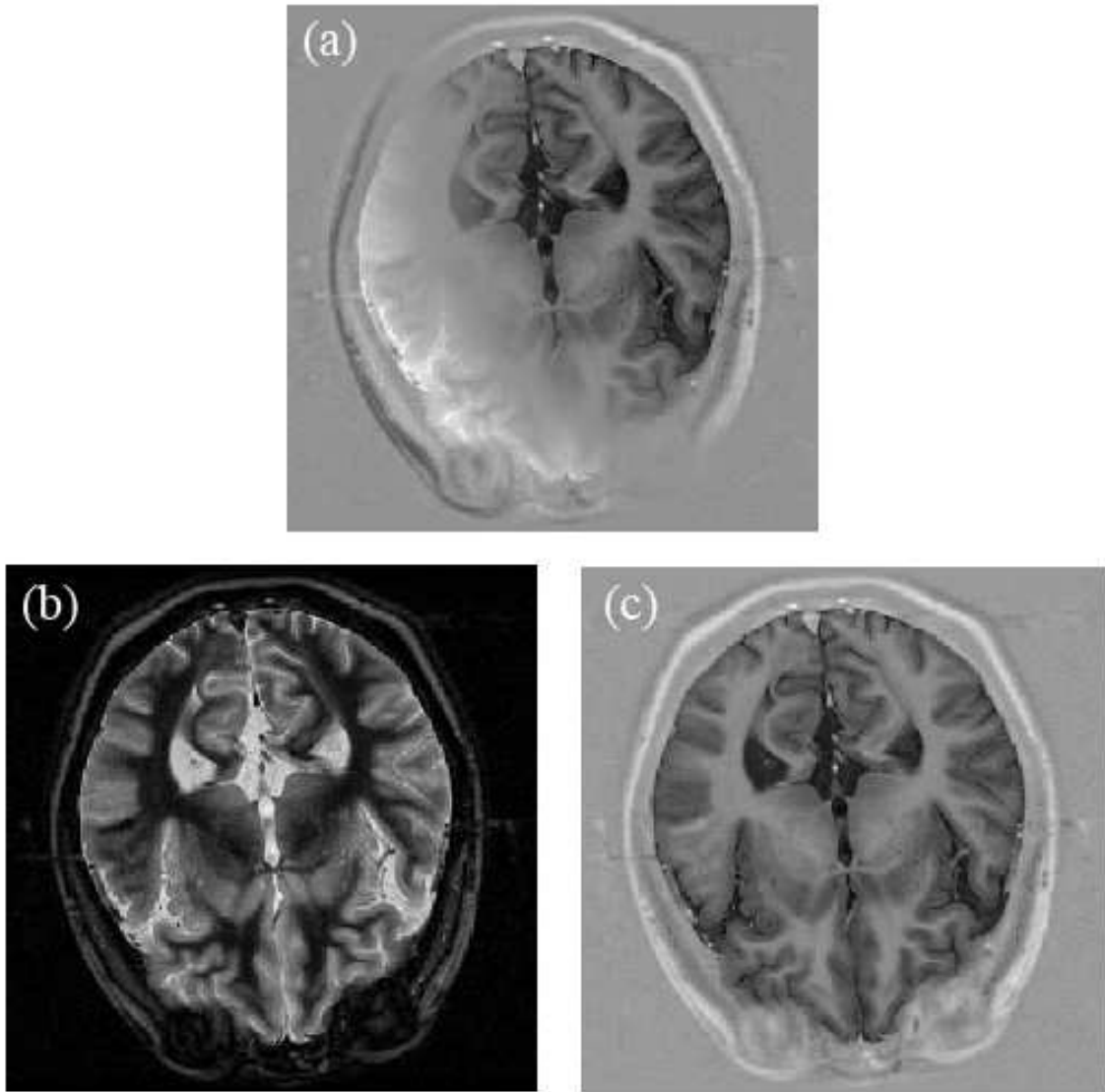


Fig. 32. Phase sensitive reconstruction of data acquired using a fast spin-echo sequence on a 15 Tesla MR scanner (a) Real image; (b) Magnitude reconstruction; (c) PSIR image.

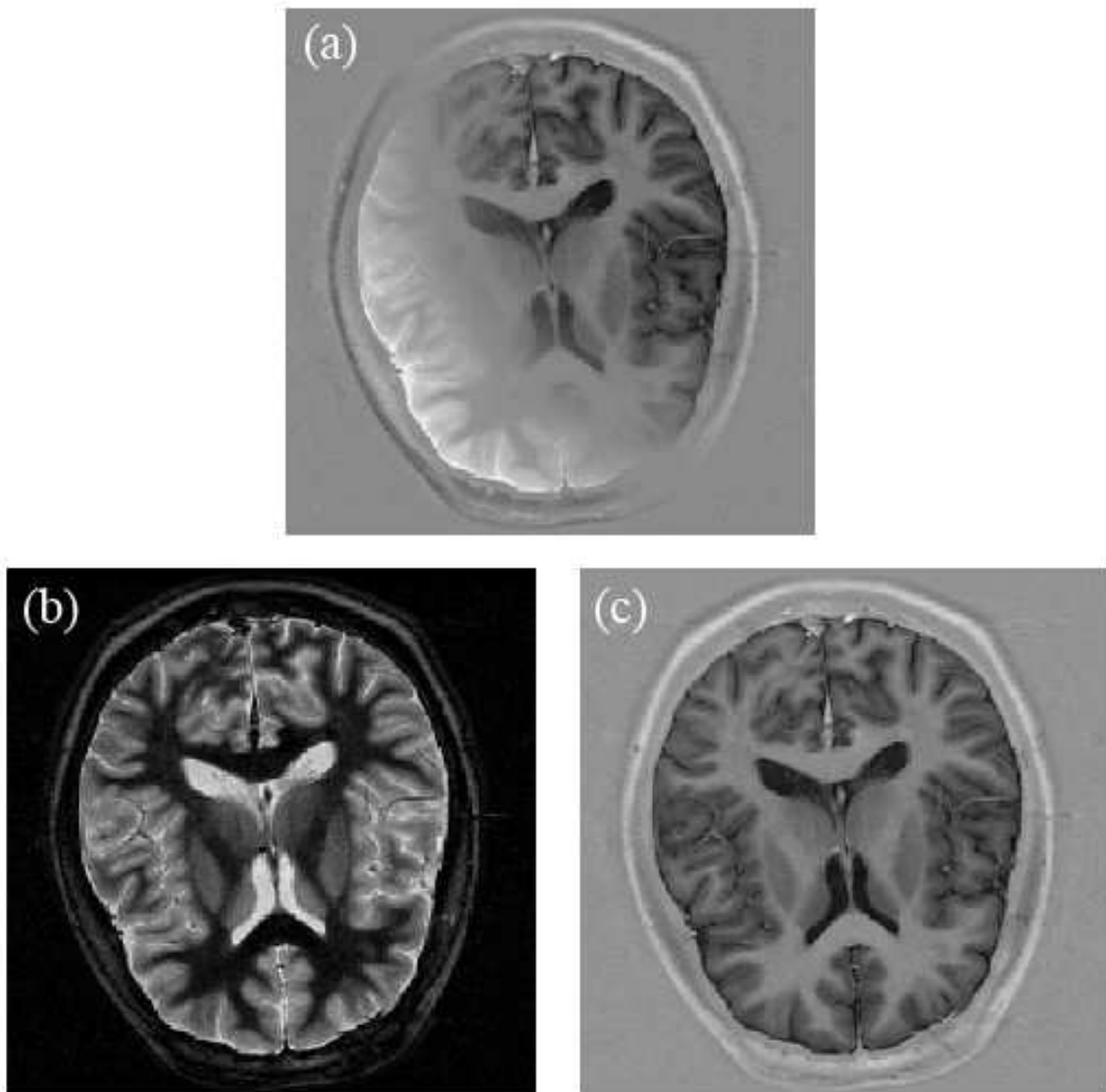


Fig. 33. Phase sensitive reconstruction of data acquired using a fast spin-echo sequence on a 15 Tesla MR scanner (a) Real image; (b) Magnitude reconstruction; (c) PSIR image. Note that the magnitude reconstruction in this case results in a contrast inversion between ventricles and the surrounding structure.

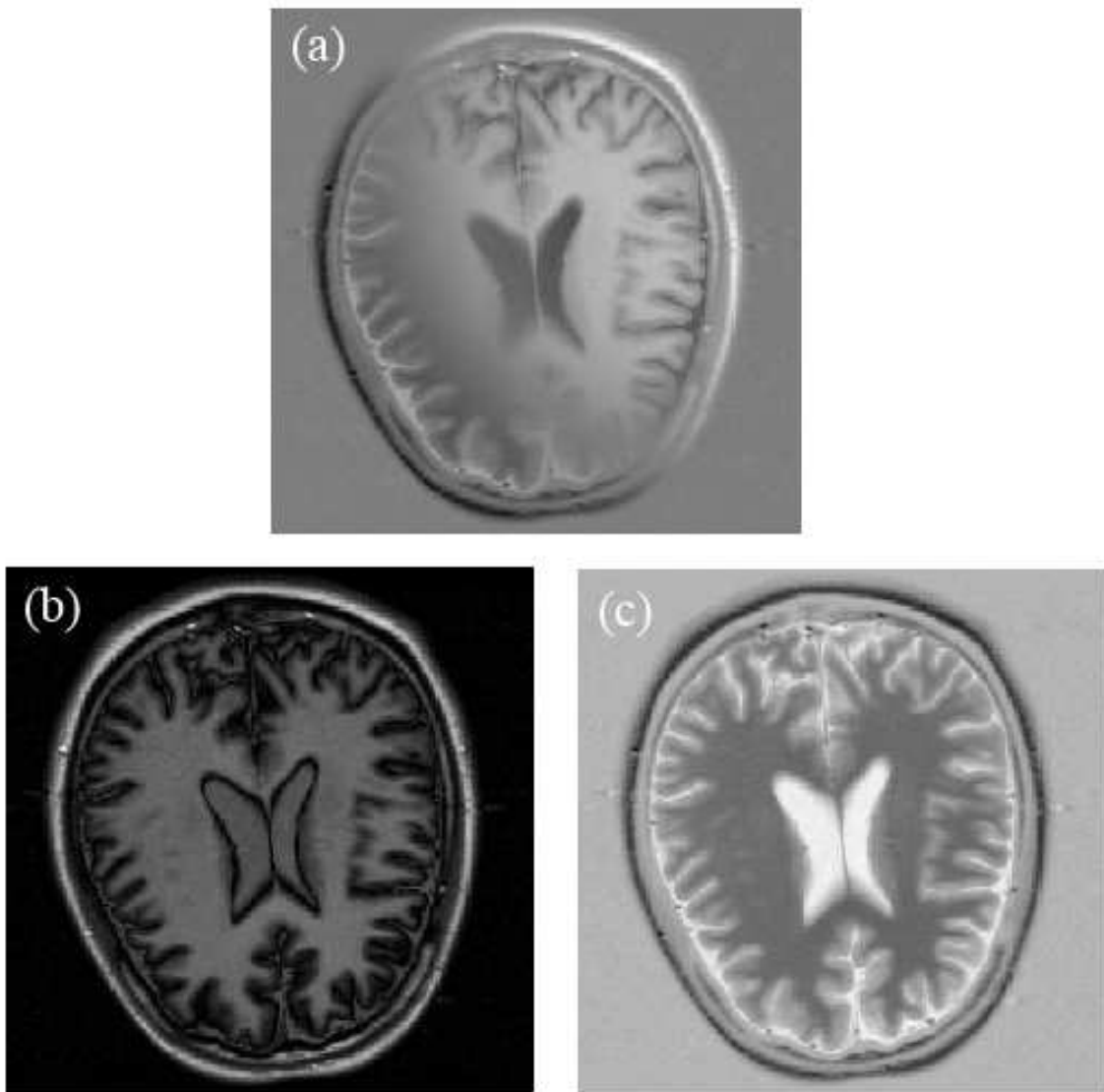


Fig. 34. Phase sensitive reconstruction of data acquired using a fast spin-echo sequence on a 15 Tesla MR scanner (a) Real image; (b) Magnitude reconstruction; (c) PSIR image reconstructed with inverted polarity. This example demonstrates the problem of global polarity determination in the PSIR reconstruction.

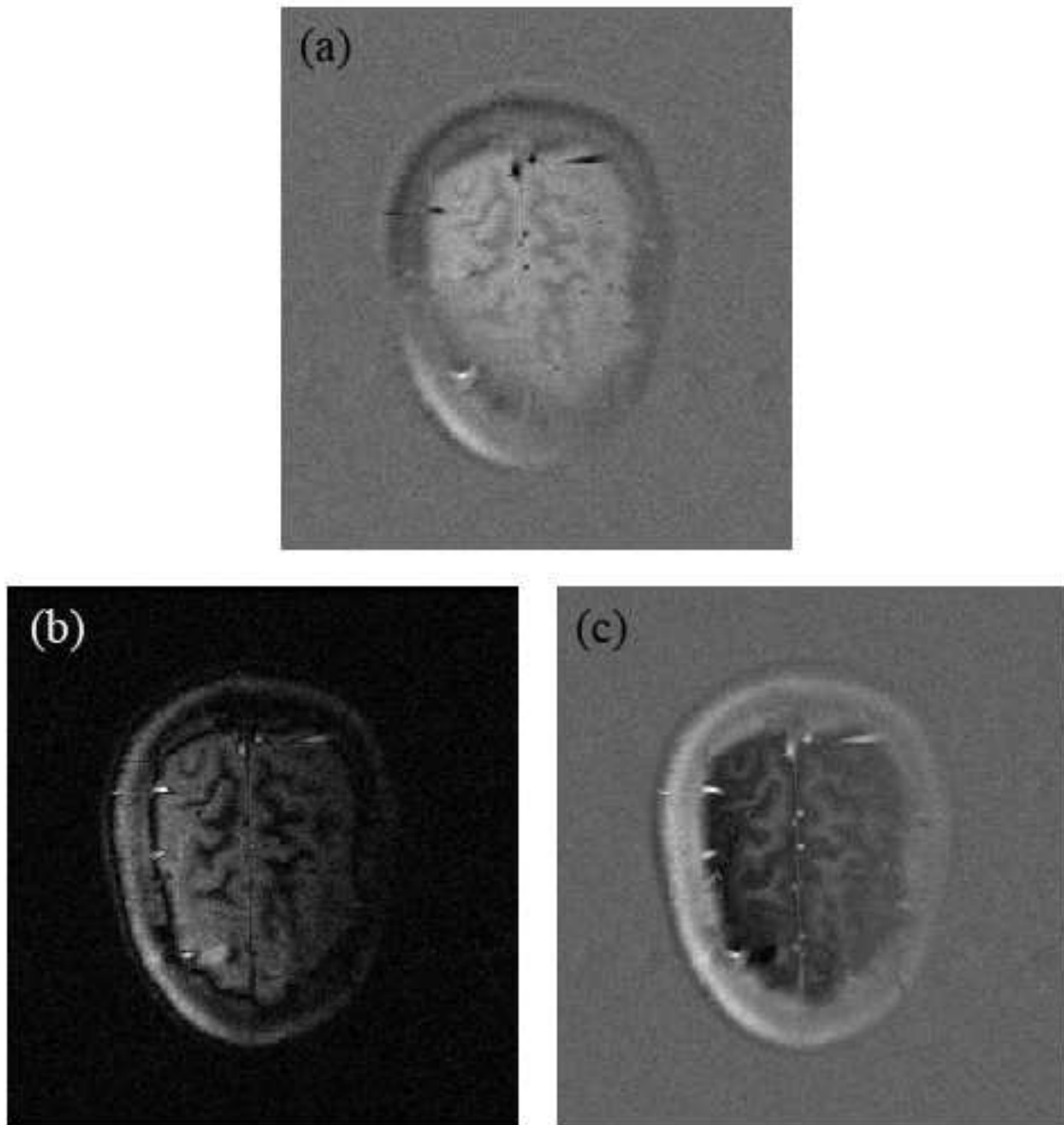


Fig. 35. Phase sensitive reconstruction of a low SNR MR data acquired using 8 coils using a fast spin-echo sequence. (a) Real image; (b) Magnitude reconstruction; (c) PSIR image.

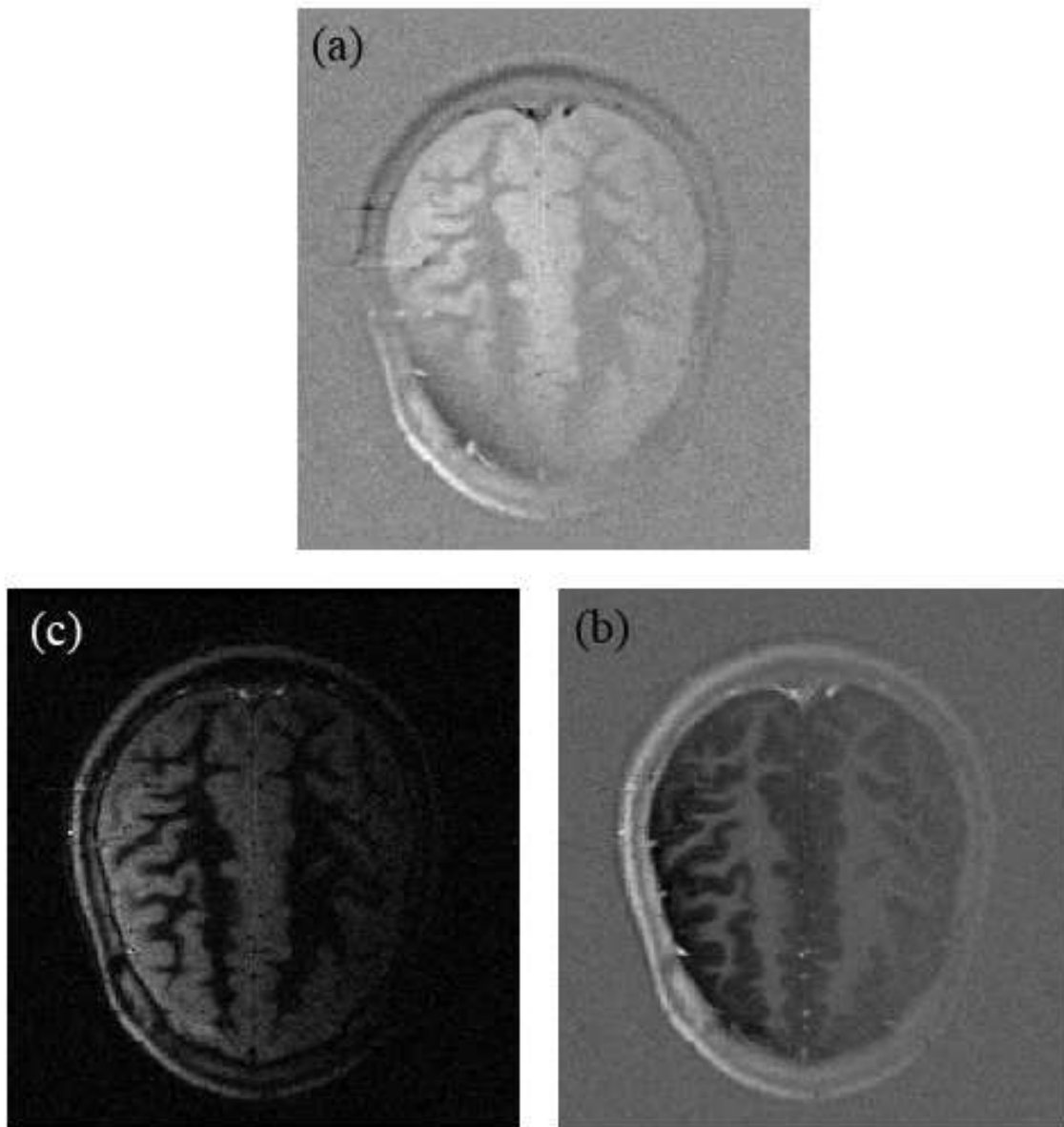


Fig. 36. Phase sensitive reconstruction of 8 coil data acquired using fast spin-echo sequence. The imaging time was 300ms. (a) Real image; (b) Magnitude reconstruction; (c) PSIR image.

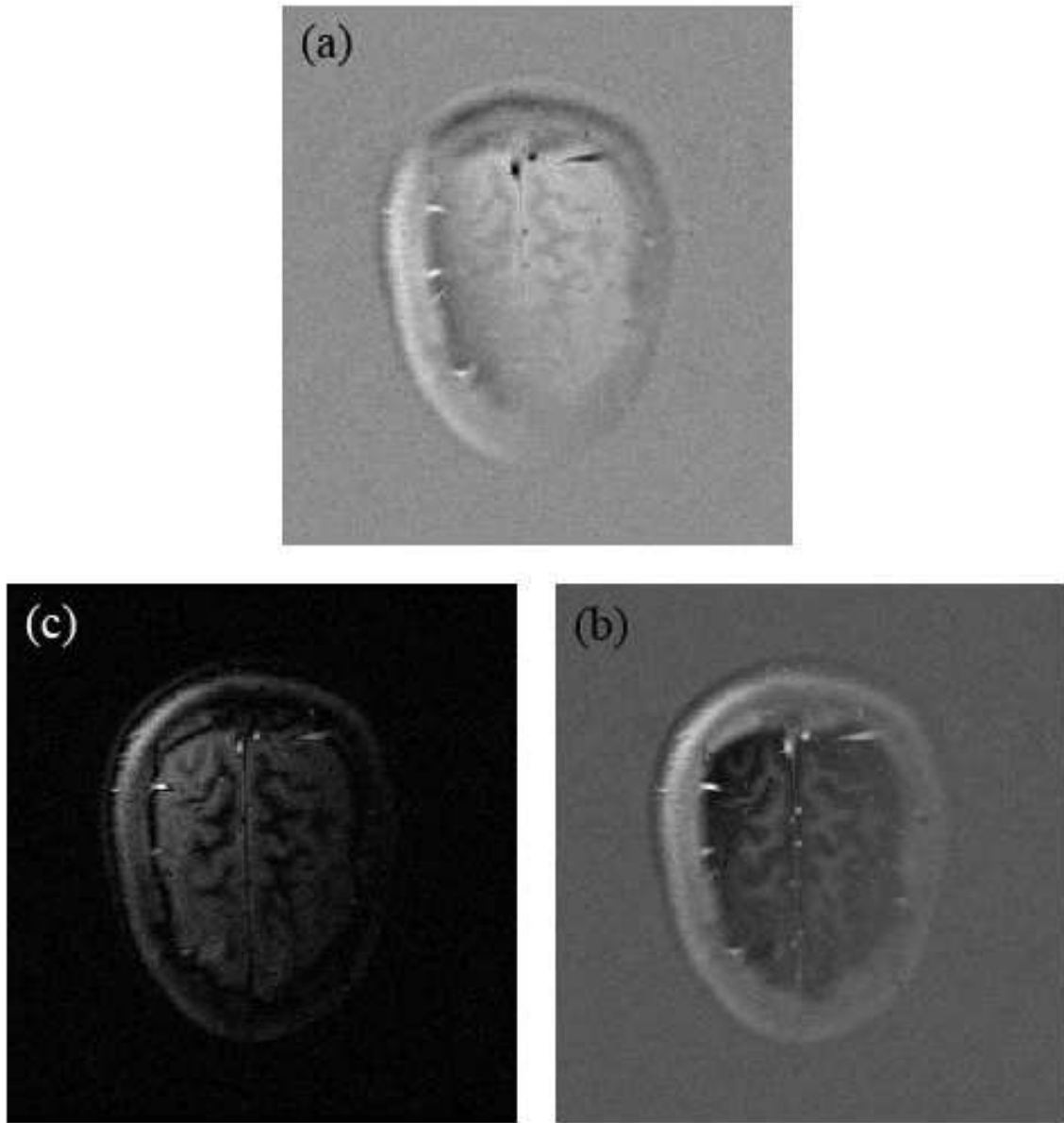


Fig. 37. Phase sensitive reconstruction of 8 coil data acquired using fast spin-echo sequence. The imaging time was 300ms. The input image SNR was 32dB. (a) Real image; (b) Magnitude reconstruction; (c) PSIR image.

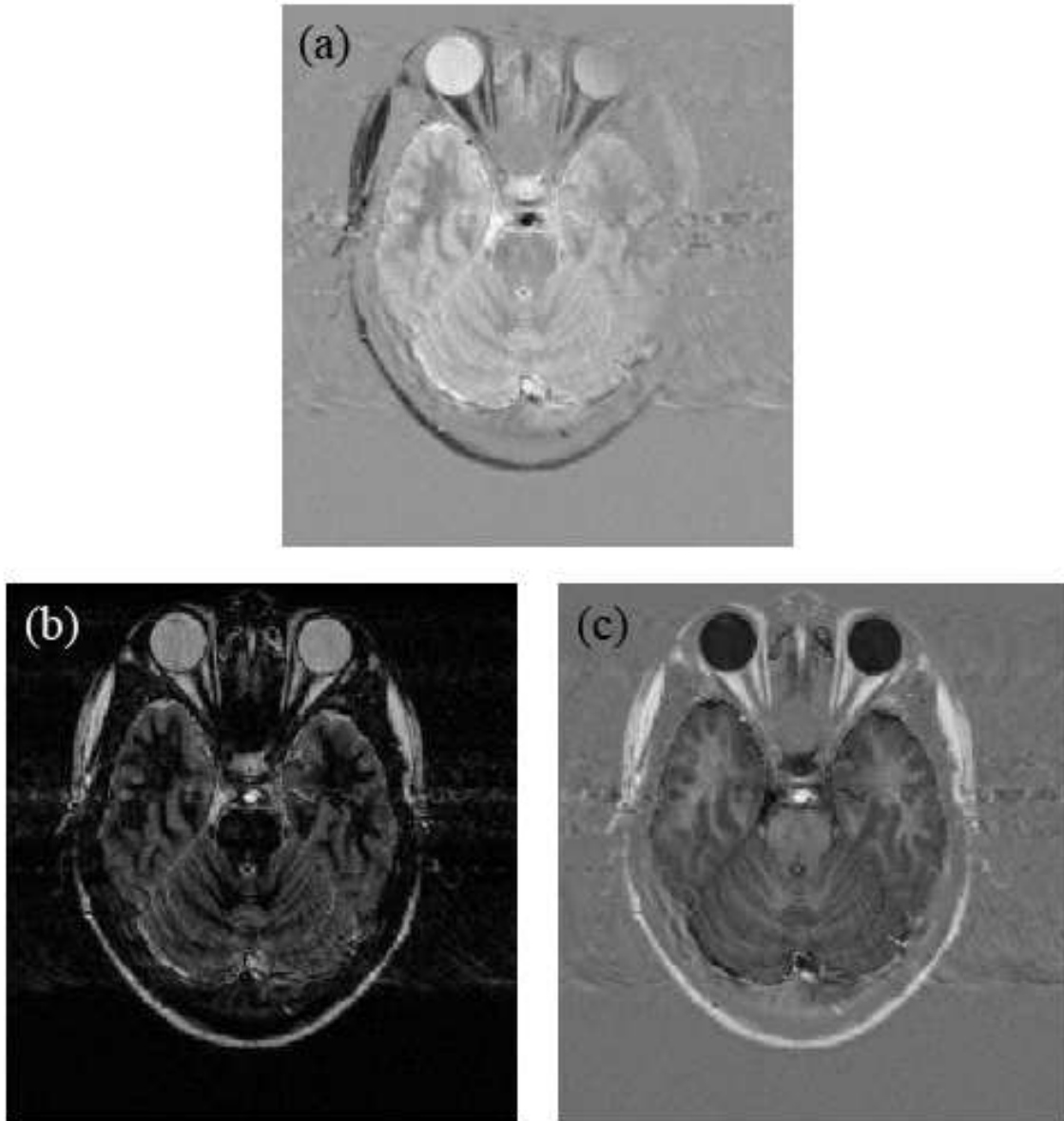


Fig. 38. Phase sensitive reconstruction of IR brain image. (a) Real part of complex image; (b) Magnitude reconstruction; (c) Phase sensitive reconstruction.

D. Discussion

The global optimum solution to the background phase estimation problem requires consideration of 2^{N^2-1} possibilities. The optimization algorithms try to obtain a sub-optimal background phase estimate approximating the global optimum in a computationally efficient way. The block merging method requires a testing of about $2.7 \times N^2$ possibilities to extract the background phase. However, the adaptive depth estimates for each block make it less computationally efficient as compared to the region growing method. Block merging method should be preferred only in low SNR images where higher averaging depths are allowable.

Both the reconstruction algorithms have an unsolved ambiguity of global polarity determination. The block merging algorithm used the fact that if the phase of a complete block is flipped by 180° , the optimum of the block remains unchanged. Thus, an obtained optimum estimate of the background phase can be 180° flipped version of the actual background phase. As a result, the PSIR image produced may be polarity reversed. A manual intervention is required at this stage to choose the correct global polarity. A suggested approach to automate this process is to choose the solution with net image intensity greater than zero [11]. For the images in our database, this approach is not found to give consistently correct polarity. For brain images with cerebrospinal fluid, the solution yielding positive moment of inertia evaluated at the center of the image can be chosen [20].

An analysis of algorithm failures was carried out to help find ways to minimize the failures. Reconstruction failures refer to cases where large portions of image reconstructed with inconsistent polarities. When the randomly distributed gaussian noise is gradually increased, the errors in reconstruction increase linearly with the decrease in SNR. These errors are sporadic and as analyzed from the presented graphs,

do not result in avalanche breakdown. Hence, decrease in SNR alone was not found to cause algorithm failure. PSIR reconstruction failed when high rate of phase variations were accompanied by low SNR. Typically, failures occurred when phase variations as fast as one complete phase cycle per 17 or less pixels were accompanied by SNR of about 25 dB or lower. PSIR algorithms assume that the background phase is almost constant in a small neighborhood and hence in the defined neighborhood, either the pixels are in phase with the neighbors or are 180° out-of-phase with them. Considering the region growing algorithm,

- If the summation of dot product of a pixel with its neighbors is greater than zero, the pixel is considered in-phase with its neighbors. Hence, its phase is stored as the extracted background phase.
- If the summation of the dot product is less than zero, 180° is added to the pixel phase and the result is stored as the extracted background phase.

Only the visited neighbors are considered in the above calculations. When the algorithm starts from the top left corner of any loop (fig. 8), only one pixel in the first order neighborhood (fig. 9) is visited previously. If this pixel is affected heavily by noise, it may lead to error in the considered pixel. In some cases, these errors may propagate leading to a large portion of image reconstructed with inconsistent polarity. Figure 39 shows one such example.

Figure 40 shows the detailed analysis of the failure start and spread. For the pixel (116, 116) under consideration, only one of its neighbors (117, 117) is an already visited pixel. The phase of this pixel being about 101° different from the considered pixel, they are interpreted as anti-phase. As a result, the phase at (116, 116) is wrongly toggled. Similarly, when decision of pixel at (115, 115) is made from pixel at (116, 116), the error spreads.

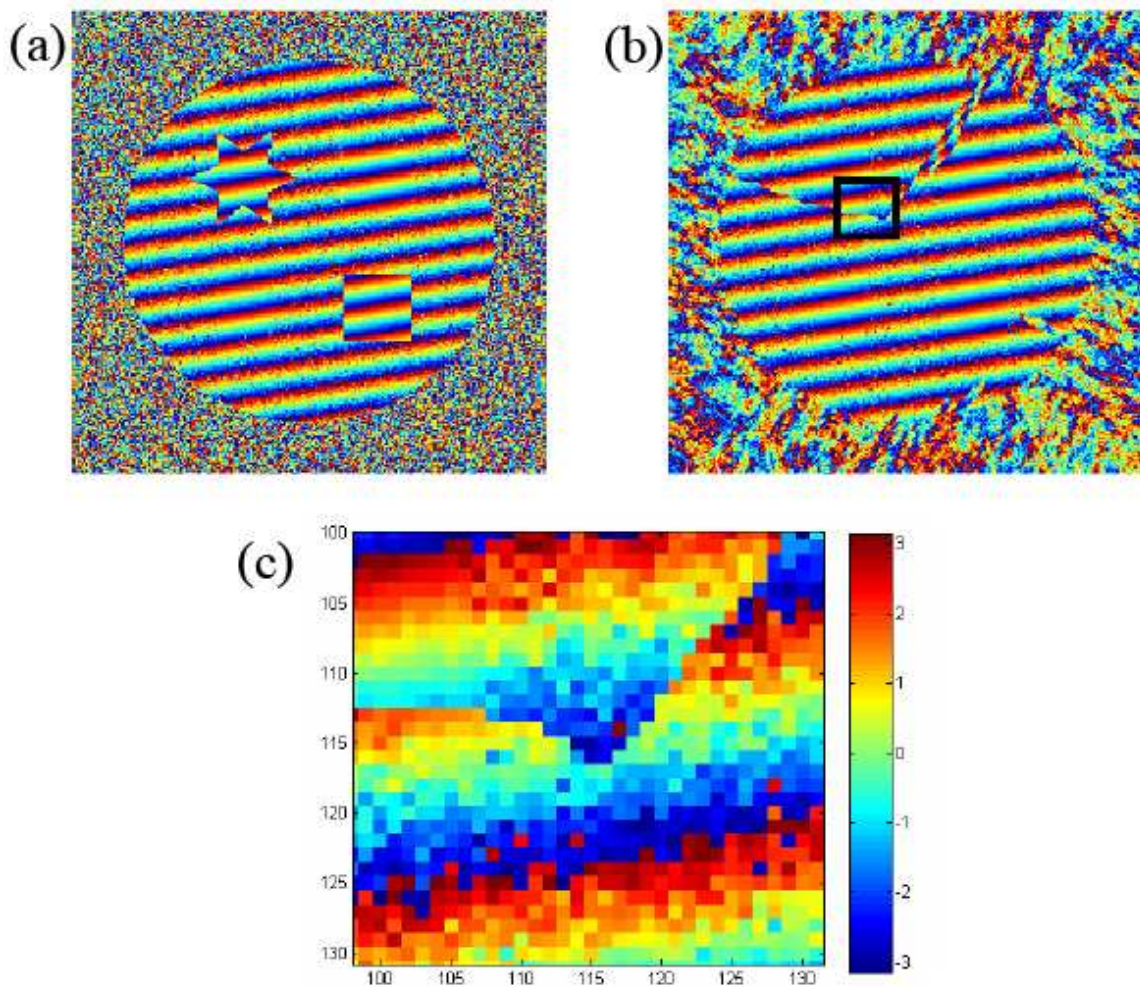


Fig. 39. Analysis of PSIR failure - 1. (a) Phase map of input image; (b) Extracted background phase by PSIR algorithm. Though the polarity information has been eliminated in the phase map as required for successful background phase extraction, a large portion extracted background phase is inconsistent with the rest of the phase map; (c) Zoomed-in failure location boxed using a black square in (b). Note that here the failure starts at a single pixel (116, 116) and spreads in a considerable portion of the phase map.

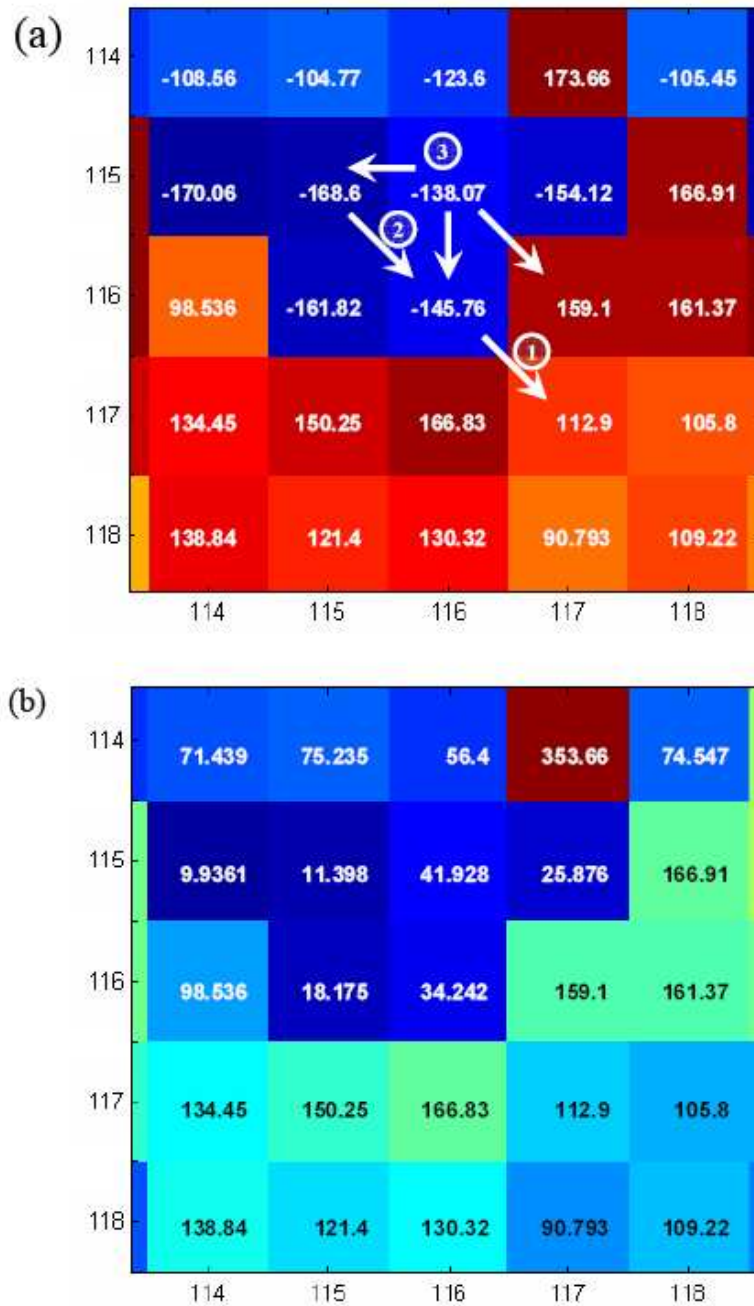


Fig. 40. Analysis of PSIR failure - 2. (a) Phase of pixels in input image surrounding pixel at location (116, 116). Pixel (116, 116) being the corner starting point in the growth trajectory, its decision is made only from pixel (117, 117). The arrows indicate the pixels used for making decision and the numbers indicate the sequence in which the shown pixels phases are determined. Pixels with similar angles are shown in similar shades; (b) Result of region growing.

Ideally, adjacent pixels should either have a very small phase difference or should be about 180° out of phase. Errors occur when adjacent pixels have a phase difference of about 90° . In cases with fast background phase variations, adjacent pixels already have significant difference in phases. If noise increases this phase difference in some critical pixels like (117, 117) in the example, the PSIR algorithm fails. Wavelet filtering and slope filtering are steps in direction of eliminating these 90° pixels. Using these methods, isolated trouble-maker pixels can be removed to a large extent. But in images with a large number of pixels with 90° phase difference packed in a small area, reconstruction is not possible with the current implementations of the algorithm. Figure 41 is one such image. Here the boundary regions have low intensity and the phase in these regions is overwhelmed by noise.

The proposed algorithms do not work properly with most gradient echo data. Due to extremely high phase variations in gradient echo images, the smooth phase criterion requiring nearly constant background phase in a local neighborhood is not satisfied. Figure 42 shows the PSIR algorithm performance on a gradient echo spine image. A failure location of the PSIR algorithm is marked by a black arrow and the neighboring region of the failure site is indicated by a white box in the phase image. To investigate the cause of failure, angular difference between neighboring pixels of the phase image was taken. This phase difference image was thresholded to indicate the regions in which neighboring pixel phases differed by about 90° (interval used: $(75^\circ, 105^\circ)$). This thresholded image is shown in 42(c). As seen, there is an almost continuous line of 90° pixels separating two opposite polarity regions. As a result, the polarity change is not detected in these regions resulting in a PSIR failure.

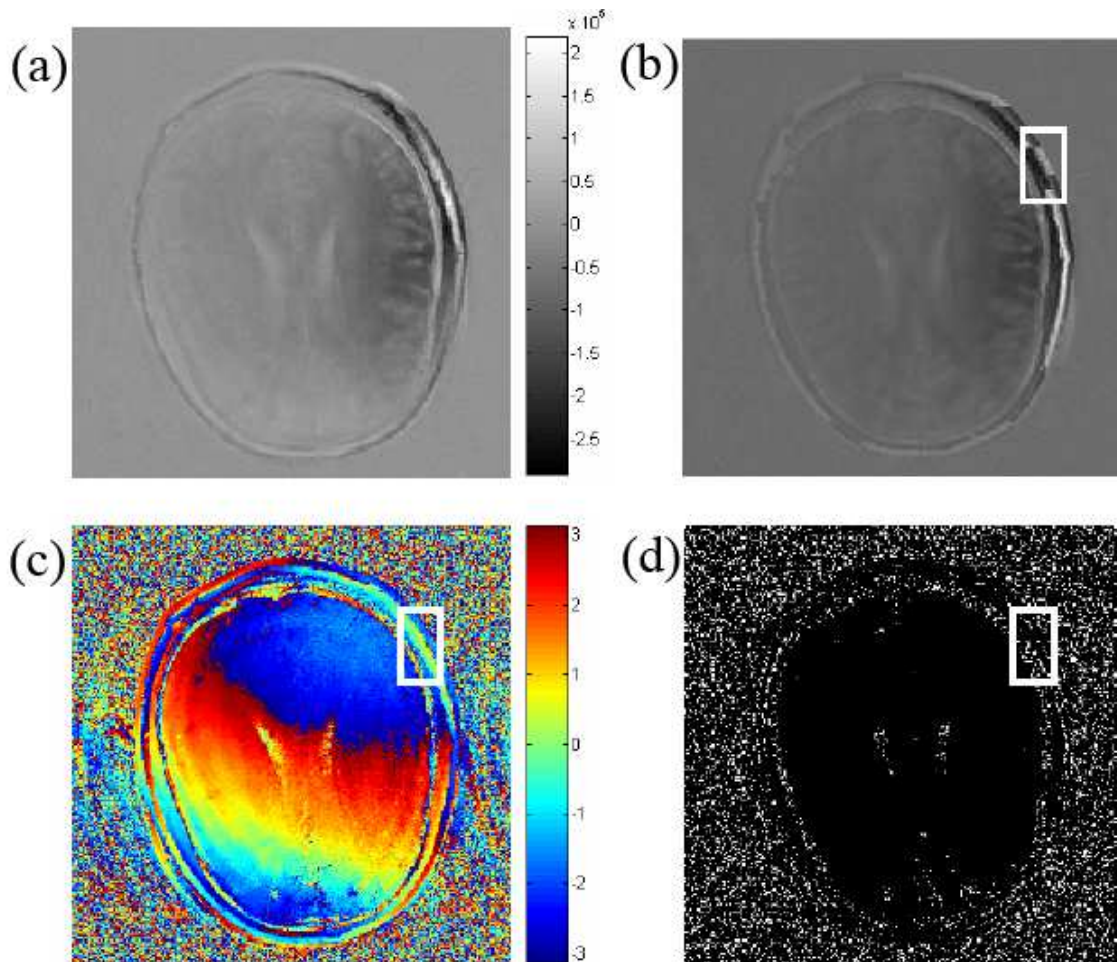


Fig. 41. Unsuccessful reconstruction of a gradient echo brain image acquired using a 3 Tesla MR scanner. (a) Real image; (b) Failed phase sensitive reconstruction. White box in the boundary region shows the failure location; (c) Phase-map. The white box indicated the region surrounding the failure site; (d) Thresholded phase difference between phases of neighboring pixels. The regions with a difference between 75° and 105° between neighboring pixels are indicated. The white box indicates the failure location crowded with pixels having almost 90° phase difference between each other.

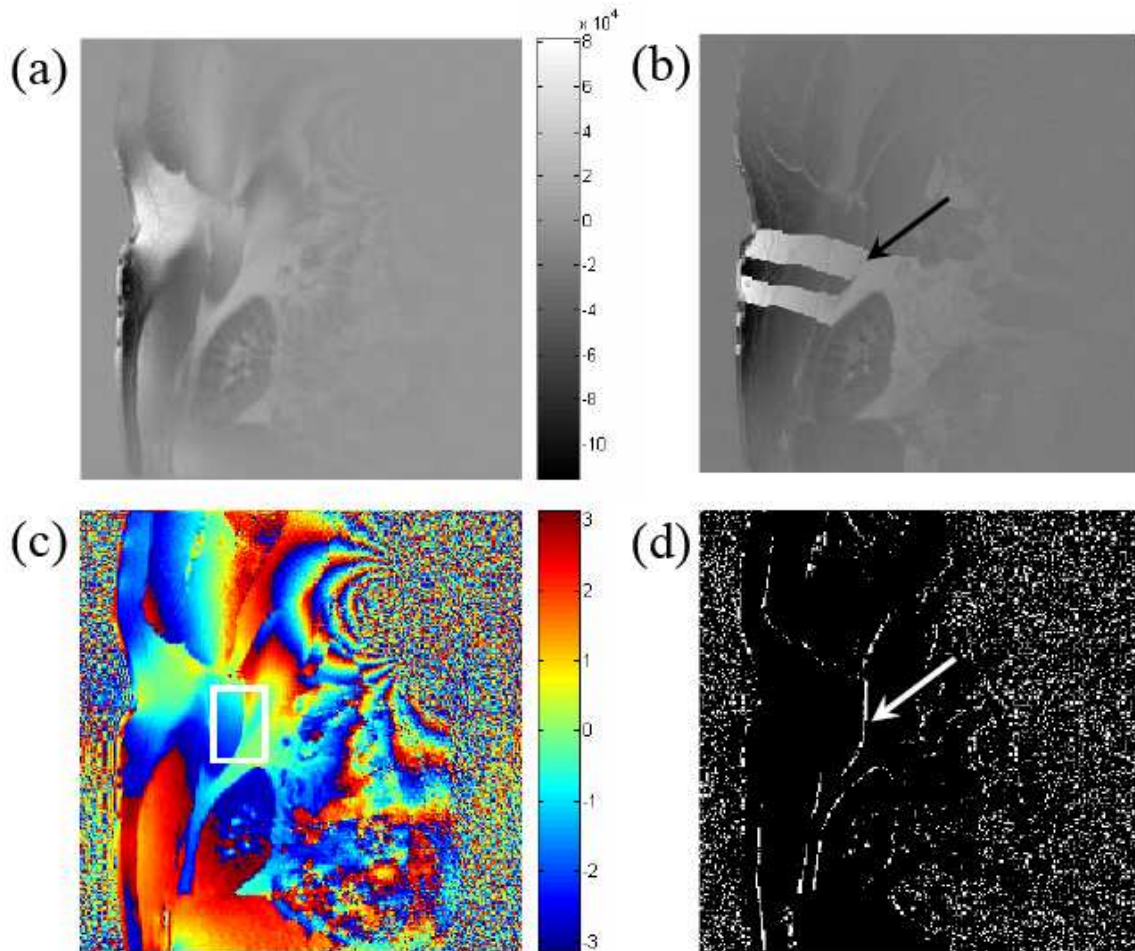


Fig. 42. Phase sensitive reconstruction of gradient echo data. (a) Real part of complex gradient echo image; (b) Unsuccessful phase sensitive reconstruction. The black arrow shows the beginning of reconstruction failure at a failure site; (c) Phase-map of the image. The white box indicated the region surrounding the failure site; (d) Thresholded phase difference between phases of neighboring pixels. The regions with a difference between 75° and 105° between neighboring pixels are indicated. The white arrow indicates the failure site.

CHAPTER IV

CONCLUSION AND FUTURE WORK

In this thesis, a new approach to phase sensitive inversion recovery (PSIR) image reconstruction has been presented. The background phase of an inversion recovery (IR) image is modeled as a Markov random field (MRF). Two different optimization algorithms have been developed to obtain a sub-optimal estimate the background phase from an IR image using the MRF model. The first algorithm, block merging, takes advantage of slow varying nature of background phase and uses a multiple resolution procedure. This imparts it robustness against noise in images with slow varying background phase. The second algorithm, region growing, starts from a single point and extracts an optimum solution along a spiral path. It is designed to handle lower SNR images with high background phase variations. To enhance the performance of these algorithms, a wavelet denoising algorithm and a modified slope-filtering approach have been investigated. The proposed methods do not require any modification in the MR hardware setup and are compatible with the existing MR systems. The performance of these algorithms was demonstrated using results of various computer simulations and *in vivo* experiments. The results show that (a) The proposed methods can perform reconstruction under rapid background phase variations with moderate SNR levels; (b) It works better for spin-echo images than gradient-echo images (where very rapid phase variations exist). The presented work is expected to be useful for a number of applications where enhanced T_1 contrast is desirable. High-field T_1 -weighted imaging and pediatric brain imaging are some of these applications.

The algorithms are currently limited to two dimensional data. This work can be extended to operate on three dimensional MR data.

REFERENCES

- [1] Bydder G.M. and Young I.R., “MR imaging: clinical use of the inversion recovery sequence,” *J Comput Assist Tomogr*, vol. 9, no. 4, pp. 841–844, August 1985.
- [2] Hajnal J.V., Bryant D.J., Kasuboski L., Pattany P.M., De Coene B., Lewis P.D., Pennock J.M., Oatridge A., Young I.R. and Bydder G.M., “Use of fluid attenuated inversion recovery (FLAIR) pulse sequences in MRI of the brain,” *J Comput Assist Tomogr*, vol. 16, no. 6, pp. 841–844, November 1992.
- [3] Zee C.S., Segall H.D., Terk M.R., Destian S., Ahmadi J., Gober J.R. and Colletti P.M., “SPIR MRI in spinal diseases,” *J Comput Assist Tomogr*, vol. 16, no. 3, pp. 356–360, June 1992.
- [4] Halligan S., Healy J.C. and Bartram C.I., “Magnetic resonance imaging of fistula-in-ano: STIR or SPIR,” *Br J Radiol*, vol. 71, no. 842, pp. 141–145, Feb 1998.
- [5] Tokunda O., Hayashi N., and Matsunga N., “MRI of bone tumors: Fast STIR imaging as a substitute for T1-weighted contrast-enhanced fat-suppressed spin-echo imaging,” *J Mag Reson Imag*, vol. 19, no. 4, pp. 475–481, April 2004.
- [6] Mai V.M., Chen Q., Bankier A.A., Zhang M., Hagspiel K.D., Berr S.S., and Edelman R.R., “Imaging pulmonary blood flow and perfusion using phase-sensitive selective inversion recovery,” *Magn Reson Med*, vol. 43, no. 6, pp. 793–795, June 2000.
- [7] Kellman P., Arai A.E., McVeigh E.R., and Aletras A.H., “Phase sensitive inversion recovery for detecting myocardial infarction using gadolinium delayed hyperenhancement,” *Magn Reson Med*, vol. 47, no. 2, pp. 372–383, February 2002.

- [8] Nitta N., Takahashi M., Furukawa A., Murata K., and Mori M., “MR imaging of the normal appendix and acute appendicitis,” *J Mag Reson Imag*, vol. 21, no. 2, pp. 156–163, February 2005.
- [9] Cappendijk V.C., Cleutjens K.B., Heeneman S., Schurink G.W., Welten R.J., Kessels A.G., van Suylen R.J., Daemen M.J., van Engelshoven J.M., and Kooi M.E., “In Vivo detection of hemorrhage in human atherosclerotic plaques with magnetic resonance imaging,” *J Mag Reson Imag*, vol. 20, no. 1, pp. 105–110, July 2004.
- [10] McVeigh E.R., Bronskill M.J., and Henkelman R.M., “Phase and sensitivity of receiver coils in magnetic resonance imaging,” *Med Phys*, vol. 13, no. 6, pp. 806–814, 1986.
- [11] Xiang Q.S., “Inversion recovery image reconstruction with multiseed region-growing spin reversal,” *J Mag Reson Imag*, vol. 6, no. 5, pp. 775–782, September 1996.
- [12] Bakker C.J.G., De Graaf C.N., and Van Dijk P., “Restoration of signal polarity in a set of inversion recovery NMR images,” *IEEE Trans Med Imaging*, vol. 3, no. 4, pp. 197–202, 1987.
- [13] Gowland P.A. and Leach M.O., “A simple method for the restoration of signal polarity in multi-image inversion recovery sequences for measuring T1,” *Mag Reson Med*, vol. 18, no. 1, pp. 224–231, 1991.
- [14] Park H.W., Cho M.H., and Cho Z.H., “Real value representation in inversion recovery NMR imaging by use of a phase correction method,” *Mag Reson Med*, vol. 3, no. 1, pp. 15–23, 1986.

- [15] Borrello J.A., Chenevert T.L., and Aisen A.M., "Regional phase correction of inversion-recovery MR images," *Mag Reson Med*, vol. 14, no. 1, pp. 56–67, 1990.
- [16] Ahn C.B., and Cho Z.H. "A new phase correction method in NMR imaging based on autocorrelation and histogram analysis," *IEEE Trans Med Imag*, vol. 6, no. 1, pp. 32–36, 1987.
- [17] Ji J.X., Ying L., Ma J., Munson D.C. and Liang Z.P. Jr, "Phase-sensitive inversion recovery imaging using a Markov random field model," in *Proc 11th Ann Meeting Intl Soc Mag Reson Med*, pp. 1068–1068, July 2003.
- [18] Garach R.M., Ji J.X., Ying L., and Ma J., "Robust phase sensitive inversion recovery imaging using a Markov random field model," in *Proc. 26th IEEE EMBS Engg. in Med. and Biology Soc.*, pp. 478–481, September 2004.
- [19] Garach R.M. and Ji J.X., "An improved region-growing method for phase sensitive reconstruction of inversion recovery magnetic resonance images," in *22nd Annual Houston Conference on Biomed. Engg. Research*, pp. 89–89, February 2005.
- [20] Ma J., "Multislice and multicoil phase-sensitive inversion-recovery imaging," *Magn Reson Med*, vol. 53, no. 4, pp. 904–910, April 2005.
- [21] Noll D.C., Nishimura D.G. and Macovski A., "Homodyne detection in magnetic resonance imaging," *IEEE Trans. on Medical Imaging*, vol. 10, no. 2, pp. 154–163, 1991.
- [22] Geman S. and Geman D., "Stochastic relaxation, Gibbs distribution and the Bayesian restoration of images," *IEEE Trans. on Pattern Analysis and Machine Intelligence*, vol. 6, no. 6, pp. 721–741, 1984.

- [23] Besag J., “On the statistical analysis of dirty pictures,” *J. Royal Statist Soc B*, vol. 48, no. 3, pp. 259–302, 1986.
- [24] Li S.Z., *Markov Random Field Modeling and Computer Vision*, New York: Springer-Verlag, 1995.
- [25] Crouse M.S. and Baraniuk R.G., “Contextual hidden Markov models for wavelet-domain signal processing,” in *Proceedings of 31st Asilomar Conference on Signal, Systems, and Computers*, pp. 95–100, November 1997.
- [26] Pizurica A., Wink A.M., Vansteenkiste E., Philips W. and Jos B.T.M. Roerdink., “A review of wavelet denoising in MRI and ultrasound brain imaging,” *Current Medical Imaging Reviews*, in press, 2005.
- [27] Zaroubi S. and Goelman G., “Complex denoising of MR data via wavelet analysis: application for functional MRI,” *Mag Reson Imaging*, vol. 18, no. 1, pp. 59-68, Jan 2000.

VITA

Ravindra Garach was born on November 24, 1981 in Rajkot, India. He attended M.K. High School, Gujarat from 1997 to 1999. In June of 2003, he received his B.E. degree in Electronics and Communications Engineering from L.D. College of Engineering, Gujarat University, India. Since then he has been pursuing his M.S. in Electrical Engineering at Texas A&M University. After completing his M.S., he intends to work in the exciting field of MRI and make further contributions to MRI research.

The author can be contacted at his permanent address or email given below:

House Name: 'Param Anand'

1/9A Ganesh Park,

Nr. Chandan Park,

Raiya Road,

Rajkot-360005

ravi.garach@gmail.com